University of Southampton

PASSIVELY AND ACTIVELY MODE-LOCKED FIBRE LASER DEVICES

by Victor Jacob Matsas

Thesis submitted for the qualification of
DOCTOR OF PHILOSOPHY

Conducted in the
DEPARTMENT OF ELECTRONICS AND COMPUTER SCIENCE

submitted
September 1993

UNIVERSITY OF SOUTHAMPTON

ABSTRACT

FACULTY OF SCIENCE

DEPARTMENT OF ELECTRONICS AND COMPUTER SCIENCE

Doctor of Philosophy

PASSIVELY AND ACTIVELY MODE-LOCKED FIBRE LASER DEVICES

by Victor Jacob Matsas

This thesis examines a number of passively and actively mode-locked fibre laser devices. The passive systems that are described incorporate the fast, saturable absorber-like action of a Kerr-type nonlinear optical switch to provide the passive mode-locking mechanism. Two such all-fibre nonlinear switches are described and analysed, namely the nonlinear optical loop mirror and the nonlinear optical gate. The mode-locked fibre laser systems based on the performance of these devices, informally known as the "Figure-of-eight" laser and the "nonlinear polarisation evolution" laser are described and characterised with respect to their modes of operation, self-starting thresholds and resonator parameters. These lasers provide a unique and convenient method for generating fundamental solitons 0.1-5 ps long. A theoretical analysis shows that the resonant loss mechanism, which is responsible for the formation of sidebands in the optical spectrum of the solitons produced by these systems, imposes a limit on the soliton pulsewidth that can be derived from a given cavity. This limit has a square-root dependence on the product of the intracavity dispersion and resonator length.

The actively mode-locked fibre laser configurations that are described are 100-1000m long and form part of an investigation into their use for distributed temperature sensing. The sensing method is based on the production of spontaneous Raman backscattered radiation from the mode-locked pulse circulating within the cavity. An extended version of the Kuizenga-Siegman (K-S) analysis of active mode-locking has shown that in systems with large dispersion-length-(bandwidth)^2 products there is a significant increase in the pulse durations that can be achieved. However, the accuracy of the K-S theory is also shown to be questionable when used for cavity lengths >50m. Optical time-domain reflectometry measurements on a 4km mode-locked ring laser provided strong supporting evidence for the successful use of long fibre lasers for distributed temperature sensing.

ACKNOWLEDGEMENTS

I wish to thank all members of the Optical Fiber Group (now part of the Opto-electronics Research Centre) for their valuable assistance and encouragement. In particular I would like to thank my supervisor, Dr. T. P. Newson, for his continuous guidance and technical (as well as moral) support. I am also grateful to Prof. D. N. Payne and Prof. W. A. Gambling for allowing me the privilege to be part of this group. Special thanks are due to Dr. D. J. Richardson for his assistance and collaboration on many of the experiments presented in this thesis, Dr. P. R. Morkel and Dr. R. I. Laming for useful discussions and to Dr. J. E. Townsend, Dr. W. L. Barnes and Mr. L. Reekie for giving generously their time and expertise, especially at the beginning of my stay here. Many thanks are also due to Chris Nash for producing diagrams of unsurpassed quality. Last, but not least, I wish to thank my family for their continuous encouragement and financial assistance.

CONTENTS

CHAPTER 1 : INTRODUCTION TO THE THESIS

CHAPTER 2 : GENERAL CHARACTERISTICS OF END-PUMPED SINGLE-MODE FIBRE LASERS AND AMPLIFIERS

CHAPTER 3 : PASSIVE MODE-LOCKING OF FIBRE-LASERS I: SQUARE PULSES, SOLITONS AND SAGNAC LOOP MIRRORS

CHAPTER 4: PASSIVE MODE-LOCKING OF FIBRE LASERS II: SYSTEMS BASED ON NON-LINEAR POLARISATION EVOLUTION

CHAPTER 5 : LONG MODE-LOCKED FIBRE LASERS FOR SENSING APPLICATIONS

CHAPTER 6: THESIS SUMMARY AND GENERAL CONCLUSIONS

If a man will begin with certainties, he shall end in doubts;
but if he will be content to begin with doubts, he shall end in certainties.

Francis Bacon, *Advancement of Learning,* I.v.8

CHAPTER 1

INTRODUCTION TO THE THESIS

1.1 INTRODUCTION

Low-loss rare-earth doped single-mode optical fibers have made a significant impact in the fields of opto-electronics and telecommunications. Since the first demonstration of the incorporation of rare-earth ions into the core of a monomode optical fibre by an extended Modified Chemical Vapour Deposition (MCVD) process [1], a wide range of rare-earth doped-based fiber devices have been developed, including fibre lasers and amplifiers as well as novel fibre sensors and fibre optic switches.

The most exciting of these developments has been in the area of optical communications with the erbium-doped fibre amplifier outperforming its rival, the semiconductor optical amplifier, within just a few years of it first being reported [2]. The field of fibre lasers has also been the focus of a high level of research activity; fibre lasers now span a range of operating wavelengths of about 3μm, from 0.651μm (Sm^{3+}) to 3.5μm (Er^{3+}), with some of the transitions reported lasing at extremely low threshold pump powers: the high field intensities that are created as a result of the ability to confine both the pump and lasing lights with the lasing species into the very small area of the fibre core, combined with good cross-section-fluorescence lifetime products has enabled efficient fibre amplifiers to be designed. For example, the Er^{3+} system can provide single-pass gains in excess of 50dB at only modest pump power levels ($\sim$50mW). The fibre laser systems that are presently being developed include the high-output power cladding-pumped fibre lasers [3], single longitudinal mode fibre lasers [4] and fibre lasers which operate at wavelengths suitable for gas sensing or medical applications [5,6]. All of these systems have the advantages of relatively wide tunability and compatibility with existing optical fibre technology.

The use of optical fibres as sensing elements for physical quantities such as pressure and temperature has been demonstrated over the last two decades. As well as point-monitoring, optical fibres also provide the capability of true distributed sensing of these quantities. Rare-earth doped single-mode optical fibres have made their presence felt in this field too, and there have been several reports on their novel incorporation into systems for current [7], temperature [8], polarimetric [9], and rotation [10] sensing.

The high gains achieved with rare-earth doped fibre amplifiers have enabled the construction of fibre lasers with cavity lengths ranging from less than a cm to more than 10km long. Whilst the symmetry of the SiO_2 molecule, unfortunately, prevents the generation of second-order nonlinear effects in optical fibres, the combination of long cavity lengths with high mode field densities has provided researchers the opportunity to observe and exploit third-order nonlinear effects. Even though the third-order non-linear coefficients involved are extremely small, these effects have been observed at power levels of a few milliwatts. For example, optical switching has been successfully demonstrated at optical power levels below one milliwatt [11].

The large (>30nm) gain bandwidths of rare-earth doped fibre amplifiers such as the Er^{3+} or the Nd^{3+} system have made fibre lasers highly attractive for ultrashort pulse generation. This has been achieved by incorporating a nonlinear optical fibre switch into a fibre laser system: the action of the optical switch, which is similar to the behaviour of a saturable absorber, causes passively mode-locked operation; in the negative group-velocity regime this leads to the generation of optical solitons [12,13]. Until the mid-eighties ultrashort pulse production could only be achieved by using dye or colour-centre lasers, often in combination with external pulse compression techniques. These recent developments in the field of ultrashort pulse generation by fibre laser technology are thought to set new standards for the reliability, simplicity and cost of future ultrafast communication systems.

The principal aim of this thesis is to investigate two types of mode-locked fibre laser systems. The systems belonging to the first type are those which utilise the characteristics of a nonlinear optical switch, based on a nonresonant Kerr-type (third-order) fibre nonlinearity, to produce passively mode-locked soliton laser operation. Two prime examples of such switches are the Sagnac loop switch and the non-linear polarisation switch. The significance of these systems lies in their capability to produce fundamental solitons of time durations ranging from ~50ps to ~100fs. Moreover, the simplicity of these systems and their compatibility with existing fibre technology makes them attractive candidates as soliton sources in a soliton-based communications system. The second type of mode-locked fibre laser systems that is investigated are long, actively mode-locked fibre lasers for use as distributed temperature sensors.

This thesis is divided as follows:

Chapter two serves as an introduction to the continuous-wave operation characteristics of fibre lasers with particular emphasis given to the Er^{3+}-doped system (a 3-level system) that was used for the majority of the experimental work. For the sake of completeness, the Pr^{3+}-doped system was chosen to represent the class of ideal 4-level fibre laser systems. Semi-analytical expressions for the gain of 3 and 4-level amplifiers are derived and concepts such as the power-dependent effective area and the optimum cut-off wavelength are discussed in detail. Guidelines for lasing threshold and output power optimisation are given and the factors that determine the operating wavelength of the Er^{3+} system are investigated.

Chapter three investigates the mode-locked operation of fibre laser systems which use the nonlinear characteristics of the Sagnac loop mirror. Following an analysis of its linear characteristics in which the effects due to the birefringence in the loop are discussed, the analysis then focuses on its nonlinear behaviour. Owing to the particular relevance of these nonlinear characteristics to optical soliton propagation, a summary of the theory of the propagation of solitons in optical fibres is presented, providing also the neccessary theoretical background for later discussions of experimental work. The ideas that have been developed are then verified experimentally using two fibre laser systems, namely the birefringence-bias and the Figure-of-8 configuration. The chapter closes with a discussion on the mechanisms that limit the pulsewidth in mode-locked fibre soliton laser systems and suggests ways that could minimise this problem.

Chapter four investigates the mode-locked operation of fibre laser systems based on another type of nonlinear fibre-optic switch which operates by using the effect of non-linear polarisation evolution (NLPE). A brief introduction to the principles of NLPE is followed by extensive experimental studies on the utilisation of this effect to provide self-starting, passively mode-locked soliton operation in both ring and Fabry-Perot fibre laser cavities. As with the Figure-of-8 laser, the systems are characterised with respect to their operating regimes and other parameters such as the cavity length and the type of fibre used. A brief account of the soliton behaviour in the presence of birefringence is also given.

Chapter five reports on an investigation into the possible use of long mode-locked fiber lasers for distributed temperature sensing (DTS). The chapter starts by discussing the merits of a fibre laser-based DTS system in comparison with those using the conventional Q-switched laser source approach. Various experimental configurations are then presented and their relative merits discussed. Optical Time Domain Reflectometry measurements on a 4km long mode-locked fibre laser were performed for the first time. An extension of the Kuizenga-Siegman model for actively mode-locked lasers to include the effects of significant intracavity dispersion present in ultra-long fibre laser cavities, helps to interpret the experimental results.

The final chapter of this thesis provides a summary of the results of each chapter and states the overall conclusions of the thesis.

REFERENCES

1. S. B. Poole, D. N. Payne and M. E. Fermann: "Fabrication of low-loss optical fibres containing rare-earth ions" *Electron. Lett.* **21** p.737 (1985).

2. R. J. Mears, L. Reekie, S. B. Poole and D. N. Payne: "Low threshold, tunable cw and Q-switched fibre laser operating at 1.5μm" *Electron. Lett.* **22** p.159 (1986).

3. J. D. Minelly, E. R. Taylor, K. P. Jedrzejewski, J. Wang and D. N. Payne: "Laser-diode pumped Nd^{3+}-doped fibre laser with output power in excess of 1 Watt" *Proc. CLEO* paper CWE6, Anaheim May 1992.

4. T. Kringlebotn, and D. N. Payne: "Efficient diode-pumped single frequency Erbium-Ytterbium fibre laser" *IEEE Phot. Techn. Lett.* Oct. (1993).

5. H. Tobben: "Temperature-tunable 3.5μm fibre laser" *Electron. Lett.* p.667 (1993).

6. W. L. Barnes and J. E. Townsend: "Highly tunable and efficient diode-pumped operation of Tm^{3+}-doped fibre lasers" *Electron. Lett.* **26** p.747 (1990).

7. R. I. Laming, D. N. Payne and L. Li: "Compact optical fibre current monitor with passive temperature stabilisation" in *Optical Fiber Sensors* vol.2 p.123, N.Orleans USA (1988).

8. M. Farries, M. E. Fermann, R. I. Laming, S. B. Poole and D. N. Payne: "Distributed temperature sensor using Nd^{3+}-doped optical fibre", *Electr.Lett.* **22** p.418 (1986).

9. H. K. Kim, S. K. Kim, H. G. Park and B. Y. Kim: "Polarimetric fibre laser sensors" *Opt. Lett.* **18** p.317 (1993).

10. M. Y. Jeon, H. J. Jeong and B. Y. Kim: "Mode-locked fibre laser gyroscope" *Opt. Lett.* **18** p.320 (1993).

11. D. J. Richarsdon, R. I. Laming and D. N. Payne: "Very low threshold Sagnac switch incorporating an Erbium-doped fibre amplifier" *Electon. Lett.* **26** p.1779 (1990).

12. D. J. Richardson, R. I. Laming, D. N. Payne, V. J. Matsas and M. W. Phillips: "Self-starting passively mode-locked fibre laser based on the amplifying Sagac switch" *Electron. Lett.* **27** p.542 (1991).

13. V. J. Matsas, T. P. Newson, D. J. Richardson and D. N. Payne: "Self-starting passively mode-locked fibre ring soliton laser exploiting non-linear polarisation rotation"

Electron. Lett. **28** p.1391 (1992).

CHAPTER 2

GENERAL CHARACTERISTICS OF END-PUMPED SINGLE-MODE FIBRE LASERS AND AMPLIFIERS

2.1 INTRODUCTION

The objective of this chapter is to review the continuous-wave operation (CW) characteristics of longitudinally pumped single-mode fibre lasers prior to a discussion of the mode-locked regime of operation. Particular emphasis is therefore given to topics which are relevant to mode-locking, such as the lasing wavelength in Er^{3+}-doped systems and the overlap of the signal with the inverted population. Wherever possible, an analytical approach is pursued. The fibre laser systems are assumed to be *ideal* 3 or 4-level systems and distinctions are made between the two. An ideal 3 or 4-level system is defined as one in which the lasing species (atoms, molecules etc) can be found to exist in either one of two energy levels only; the "ground" state or the "excited" (or "lasing") state. In this respect both systems are effectively "2-level" systems and the only lifetime of significance is the *total* lifetime of the excited state. This assumption is valid for the laser transitions in three different types of rare-earth doped fibres, namely the $^4F_{3/2}\rightarrow{}^4F_{9/2}$ transition in Nd^{3+} pumped at 810nm, the $^4I_{13/2}\rightarrow{}^4I_{15/2}$ transition in Er^{3+}, pumped at the excited-state-absorption-free wavelength of 980nm and the $^1G_4\rightarrow{}^3H_5$ transition in Pr^{3+} pumped at 1017nm. The systems are assumed to be homogeneously broadened; in the case of the Er^{3+} system, the Stark-splitting effect can be accounted for by ascribing a wavelength-dependent emission and absorption cross section.

The fibre modes for the signal and pump wavelengths are assumed to be Gaussian and their spotsizes with respect to the fibre V-value are determined not by Marcuse's formula [1] but by using a more appropriate formula derived by Whitley [2]. Whitley's formula provides the respective Gaussian mode spotsize of an LP_{01} mode by maximising the *overlap* between the two as opposed to maximising the corresponding *launch efficiency* (Marcuse). This approach is shown to give more precise results when used for fibre amplifier gain calculations.

The semi-analytical expressions which are derived for the small-signal gain of ideal 3 and 4-level fibre amplifiers can be used to determine the lasing threshold of fibre laser cavities using such amplifiers. The effect of Amplified Spontaneous Emission (ASE) on the amplifier gain is neglected, as it is not relevant for laser threshold calculations. Gain optimisation curves are drawn with respect to the fibre cut-off wavelength and the concept of a pump power-dependent effective area is introduced in connection with the overlap between the signal mode and the inverted ion population. This is followed by the determination of the lasing wavelength in systems with wavelength-dependent signal emission and absorption cross-sections, such as the Er^{3+} system. Finally, this chapter ends by deriving a formula for the fibre laser slope efficiency and suggests methods that can lead to output power optimisation.

2.2 SMALL-SIGNAL GAIN OF 3 AND 4-LEVEL SINGLE-MODE FIBRE AMPLIFIERS

To obtain an expression for the small-signal gain of a single-mode fibre amplifier, the relationship between the pump power and the population densities for 3 and 4-level systems first needs to be calculated. The pump absorption along the doped fibre can then be determined and hence the small-signal gain can be evaluated. The dependence of the small-signal gain on various parameters such as the fibre cut-off wavelength and the wavelength-dependent signal absorption and emission cross-sections is then investigated.

2.2.1 Population Densities for 3 and 4-level Systems

First consider an ideal 4-level laser system. A standard rate equation analysis [3] yields the following formulae for the energy level population densities of a 4-level system at steady-state conditions:

$$\frac{N_2(r,z)}{N_{total}(r,z)}=\frac{W_p(r,z)\tau_f}{W_p(r,z)\tau_f+W_s(r,z)\tau_f+1} \tag{2.1}$$

$$\frac{N_1(r,z)}{N_{total}(r,z)}=\frac{W_s(r,z)\tau_f+1}{W_p(r,z)\tau_f+W_s(r,z)\tau_f+1} \tag{2.2}$$

with

$$W_p(r,z)\equiv\frac{\sigma_{p_a}I_p(r,z)}{h\nu_p} \quad ; \quad W_s(r,z)\equiv\frac{\sigma_{s_e}I_s(r,z)}{h\nu_s} \tag{2.3}$$

where h is Planck's constant, $N_1(r,z)$ and $N_2(r,z)$ are the lasing species population densities (eg number of ions per unit volume) in the ground and the upper lasing level states respectively with $N_{total}(r,z)=N_1(r,z)+N_2(r,z)$, σ_{pa} and σ_{se} denote the pump absorption and signal emission cross-sections respectively, τ_f is the total (fluorescence) lifetime of the lasing level, ν_p and ν_s are the frequencies of the pump and laser light respectively and $I_p(r,z)$, $I_s(r,z)$ refer to the pump and laser intensities at a radial distance r from the fibre core and axial distance z. τ_f is a mixture of two components, the radiative part τ_{rad} and the non-radiative part τ_{nrad} of the laser transition, which satisfy the following relationship:

$$\frac{1}{\tau_f}=\frac{1}{\tau_{rad}}+\frac{1}{\tau_{nrad}} \tag{2.4}$$

A similar rate equation analysis for the ideal 3-level system [3] provides us with the following equations for the relevant energy level population densities at equilibrium:

$$\frac{N_2(r,z)}{N_{total}(r,z)}=\frac{W_p(r,z)\tau_f+\gamma W_s(r,z)\tau_f}{W_p(r,z)\tau_f+(1+\gamma)W_s(r,z)\tau_f+1} \tag{2.5}$$

$$\frac{N_1(r,z)}{N_{total}(r,z)}=\frac{W_s(r,z)\tau_f+1}{W_p(r,z)\tau_f+(1+\gamma)W_s(r,z)\tau_f+1} \tag{2.6}$$

where

$$\gamma \equiv \frac{\sigma_{s_a}}{\sigma_{s_e}} \tag{2.7}$$

σ_{sa}, σ_{se} being the signal absorption and emission cross-sections respectively. The pump emission cross-section is assumed to be zero in both the 3 and 4-level systems.

Assuming a Gaussian approximation for the pump and laser mode profiles inside the fiber:

$$W_p(r,z)=W_p(0,z)e^{-\frac{r^2}{\omega_p^2}} \qquad W_s(r,z)=W_s(0,z)e^{-\frac{r^2}{\omega_s^2}} \tag{2.8}$$

where r is the radial coordinate across the (circular) fibre waveguide and ω_p,ω_s are the radii where the intensity has dropped to 1/e of its value at r=0. The distribution of the dopant ions is assumed to be "top hat" (ie having a square profile extending to $r=r_0$) and being uniform along the fibre. $P_k(z)$ (k=p,s) is the total power carried by the fibre mode and is given by

$$P_k(z)=\int_0^\infty I_k(r,z)2\pi r dr=I_k(0,z)\pi\omega_k^2=\frac{W_k(0,z)h\nu_k}{\sigma_k}\pi\omega_k^2=W_k(0,z)\tau_f P_k^{sat} \tag{2.9}$$

where

$$P_k^{sat}\equiv\frac{h\nu_k}{\sigma_k\tau_f}\pi\omega_k^2 \tag{2.10}$$

is the signal or pump saturation power and σ_k is either σ_{pa} or σ_{se}.

2.2.2 Pump Absorption

The amount of inverted ions at any point along the doped optical fibre is determined (through eqns.(2.1) and (2.2)) by the amount of the pump light that is present. In the case of an end-pumped fibre, the absorption of the pump light due to the dopant ions and the attenuation due to the background losses is given by

$$\int_0^\infty \frac{\partial I_p(r,z)}{\partial z} 2\pi r dr = -\int_0^\infty \left(\sigma_{p_a} N_1(r,z) + \alpha_p\right) I_p(r,z) 2\pi r dr \tag{2.11}$$

or, in terms of the total power carried by the pump mode $P_p(z)$,

$$\frac{dP_p(z)}{dz} = -\sigma_{p_a} P_p(z) \int_0^{r_0} F_p(r) N_1(r,z) 2\pi r dr - \alpha_p P_p(z) \int_0^\infty F_p(r) 2\pi r dr \tag{2.12}$$

where $F_p(r)$ is defined as

$$F_p(r) \equiv \frac{e^{-\frac{r^2}{\omega_p^2}}}{\pi \omega_p^2} \tag{2.13}$$

and α_p is the pump backround loss coefficient. The pump absorption length in the absence of background losses ($\alpha_p=0$), L_0, is defined as

$$L_0 \equiv \frac{1}{\sigma_{p_a} N_{total}} \tag{2.14}$$

Case (a): No pump background losses

At threshold ($W_s(r,z)=0$) and in the absence of any pump background losses ($\alpha_p=0$), eqn.(2.12) becomes

$$\frac{dP_p(z)}{dz} = -\left[\sigma_{p_a} N_{total} \int_0^{r_0} \frac{F_p(r)}{p(z) e^{-r^2/\omega_p^2} + 1} 2\pi r dr\right] P_p(z) \tag{2.15}$$

where

$$p(z) \equiv \frac{P_p(z)}{P_p^{sat}} \tag{2.16}$$

is a normalised pump parameter. When the radial integral is determined this reduces to

$$\frac{dp(z)}{dz} = \frac{1}{L_0} \ln \left[\frac{p(z)\ e^{-r_0^2/\omega_p^2} + 1}{p(z) + 1} \right] \tag{2.17}$$

Eqn.(2.17) can only be solved numerically [4], but by approximating the logarithmic function on the RHS with the rational function (see Appendix to Ch.2)

$$\ln \left[\frac{p(z) e^{-r_0^2/\omega_p^2} + 1}{p(z) + 1} \right] \approx \frac{-p(z)\left(1 - e^{-r_0^2/\omega_p^2}\right)}{p(z) + 1} \left[1 + \frac{C_1 p(z)}{C_2 p(z) + 1} \right] \tag{2.18}$$

an approximate solution can be given in closed form:

$$\begin{aligned} \ln\alpha = & \left(1 - e^{-r_0^2/\omega_p^2}\right) \left[p(0)\,(1-\alpha) \frac{\omega_p^2}{r_0^2} - \frac{L}{L_0} \right] \\ & - \frac{C_1(1 - C_1 - C_2)}{(C_1 + C_2)^2} \ln \left[\frac{\alpha p(0)\,(C_1 + C_2) + 1}{p(0)\,(C_1 + C_2) + 1} \right] \end{aligned} \tag{2.19}$$

where L is the fiber length and

$$\alpha \equiv \frac{P_p(L)}{P_p(0)} \tag{2.20}$$

is the residual pump fraction at the fiber end. C_1 and C_2 are constants which depend only on the normalised pump spot size ω_p/r_0 (see Appendix to Ch.2).

Case (b): Inclusion of pump background losses

Eqn.(2.12) is now equivalent to

$$\frac{dP_p(z)}{dz}=\left\{\frac{P_p^{sat}}{P_p(z)L_0}\ln\left[\frac{p(z)\,e^{-r_0^2/\omega_p^2}+1}{p(z)+1}\right]-\alpha_p\right\}P_p(z) \tag{2.21}$$

By using the same approximation for the logarithmic function as in case (a), the approximate closed-form solution of this equation is

$$\begin{aligned}&\ln\alpha+\frac{L}{L_0}\left[1-e^{r_0^2/\omega_p^2}+\frac{L_0}{L_p}\right]+C_3\ln\left[\frac{C_4(\alpha p(0))^2+C_5\alpha p(0)+C_6}{C_4(p(0))^2+C_5p(0)+C_6}\right]\\&=C_7\left(\tanh^{-1}(C_8\alpha p(0)+C_9)-\tanh^{-1}(C_8p(0)+C_9)\right)\end{aligned} \tag{2.22}$$

where

$$L_p\equiv\frac{1}{\alpha_p} \tag{2.23}$$

and C_i ($i=3..9$) are constants that depend on ω_p/r_0, L_0 and L_p (see Appendix to Ch.2) and are determined in a similar fashion as for C_1 and C_2.

Fig.2.1 plots the numerical solution of eqn.(2.12) for an Er^{3+} amplifier 200m long in the two cases of (a) zero background loss ($L_p=\infty$) and (b) L_p=2000m. The derived approximate analytic solutions given by eqns.(2.19) and (2.22) were so close to the numerical solution of eqn.(2.12) that the two could not be distinguished. With reference to p(0), ie the ratio of the input pump power $P_p(0)$ to P_p^{sat}, the absorption of the fibre is divided into two main regions: for $p(0) > 10$ the absorption is linear whereas for $p(0) < 1$ the fibre absorption is exponential.

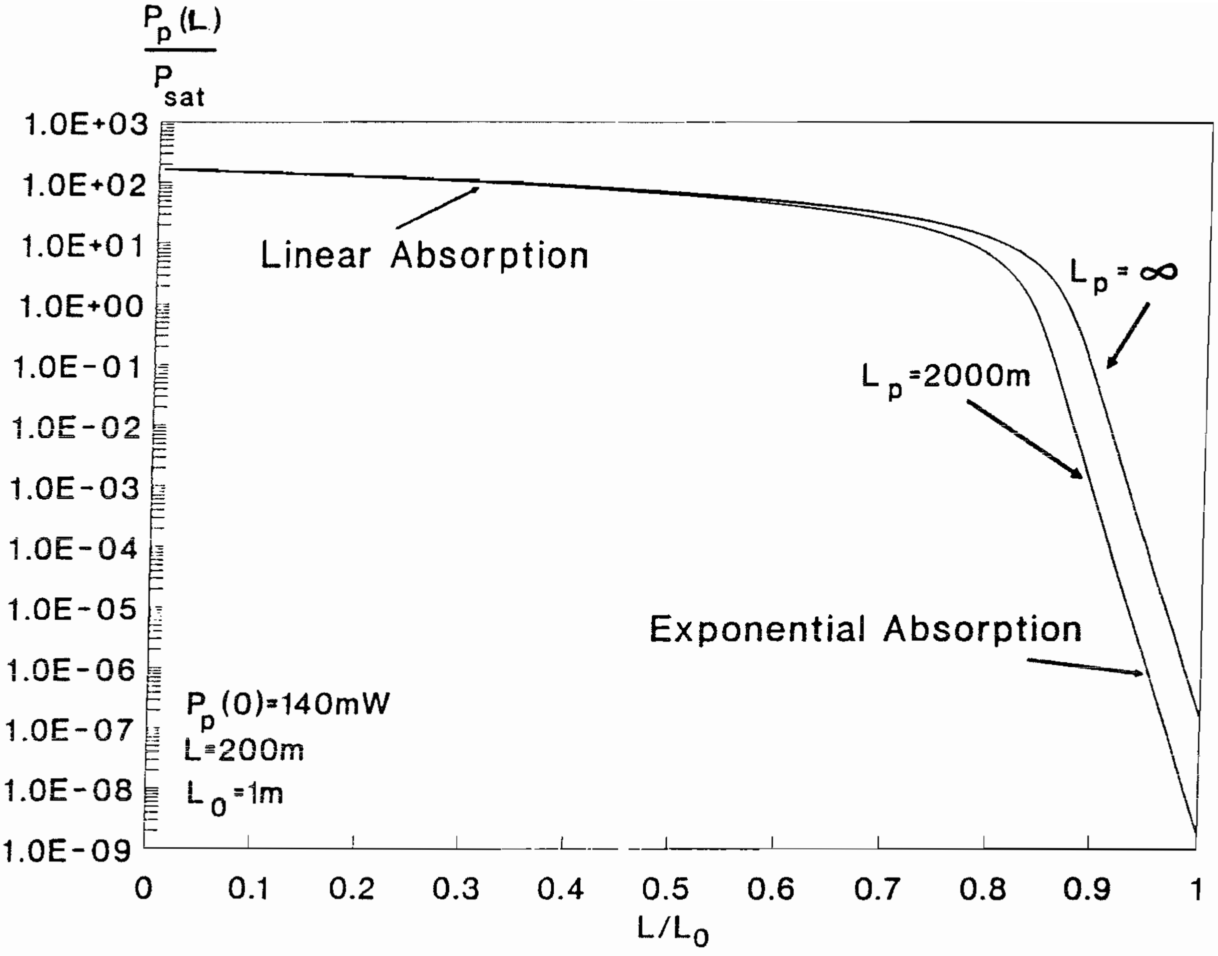

Fig.2.1 Er^{3+} amplifier pump absorption: $r_0=2\mu m$, $\omega_p/r_0=1$, $\sigma_{pa}=2.52\times10^{-25}$, $\lambda_p=980nm$, $\tau_f=12ms$.

2.2.3 Small-Signal Gain

With a knowledge of the number of excited ions at each point along the fibre, the small-signal gain can be calculated. The propagation equation for a signal at the lasing wavelength is described by

$$\int_0^\infty \frac{\partial I_s(r,z)}{\partial z} 2\pi r dr = \int_0^\infty \left(\sigma_{s_e} N_2(r,z) - \alpha_s\right) I_s(r,z) 2\pi r dr \qquad (2.24)$$

for the 4-level system and

$$\int_0^\infty \frac{\partial I_s(r,z)}{\partial z} 2\pi r dr = \int_0^\infty \left(\sigma_{s_e} N_2(r,z) - \sigma_{s_a} N_1(r,z) - \alpha_s\right) I_s(r,z) 2\pi r dr \qquad (2.25)$$

for the 3-level system. In terms of the power carried by the mode $P_s(z)$,

$$\frac{dP_s(z)}{dz} = \left[\sigma_{s_e} N_{total} \int_0^{r_0} F_s(r) 2\pi r dr - \int_0^{r_0} \sigma_{s_e} N_1(r,z) F_s(r) 2\pi r dr - \alpha_s \right] P_s(z) \qquad (2.26)$$

$$\frac{dP_s(z)}{dz} = \left[\sigma_{s_e} N_{total} \int_0^{r_0} F_s(r) 2\pi r dr - \int_0^{r_0} \left(\sigma_{s_e} + \sigma_{s_a}\right) N_1(r,z) F_s(r) 2\pi r dr - \alpha_s \right] P_s(z) \qquad (2.27)$$

for the 4 and 3-level laser amplifiers respectively. $F_s(r)$ is defined as

$$F_s(r) \equiv \frac{e^{-\frac{r^2}{\omega_s^2}}}{\pi \omega_s^2} \qquad (2.28)$$

and α_s is the signal intensity background loss coefficient. We have also used the fact that $N_2(r,z) = N_{total} - N_1(r,z)$ for ideal 3 and 4-level systems. Using eqn.(2.12) to eliminate dz from eqns. (2.26) and (2.27) we obtain the following expressions

$$\int_{P_s(0)}^{P_s(L)} \frac{dP_s}{P_s} = \frac{\sigma_{s_e}}{\sigma_{p_a}}\left(1 - e^{-r_0^2/\omega_s^2}\right)\frac{L}{L_0} + \frac{\sigma_{s_e}}{\sigma_{p_a}}\frac{\omega_p^2}{\omega_s^2}\int_{p(0)}^{p(L)} S(p)\frac{dp}{p} - \alpha_s L \tag{2.29}$$

$$\int_{P_s(0)}^{P_s(L)} \frac{dP_s}{P_s} = \frac{\sigma_{s_e}}{\sigma_{p_a}}\left(1 - e^{-r_0^2/\omega_s^2}\right)\frac{L}{L_0} + \frac{\left(\sigma_{s_e}+\sigma_{s_a}\right)}{\sigma_{p_a}}\frac{\omega_p^2}{\omega_s^2}\int_{p(0)}^{p(L)} S(p)\frac{dp}{p} - \alpha_s L \tag{2.30}$$

where S(p) is a function that represents the effect of the power-dependent overlap between the signal and the population inversion and is given by

$$S(p) \equiv \frac{\int_0^{r_0} N_1(r,z)\, e^{-r^2/\omega_s^2}\, 2\pi r dr}{\int_0^{r_0} N_1(r,z)\, e^{-r^2/\omega_p^2}\, 2\pi r dr + \frac{\alpha_p}{\sigma_{p_a}}\pi\omega_p^2} \tag{2.31}$$

Again, we consider two cases with respect to pump background losses:

Case (a): No pump background loss

In the case of zero pump background loss ($\alpha_p = 0$) and under the assumption of negligible signal power ($W_s(r,z) = 0$) it can be shown that S(p) always lies between two values, ie $S_0(p=0) < S_0(p) < S_0(p=\infty)$ where the subscript 0 indicates that there is zero pump background loss and

$$S_{\min} \equiv S_0(p=0) = \frac{\omega_s^2\left(1 - e^{-r_0^2/\omega_s^2}\right)}{\omega_p^2\left(1 - e^{-r_0^2/\omega_p^2}\right)} \tag{2.32}$$

$$S_{\max} \equiv S_0(p \rightarrow \infty) = \frac{1 - e^{-r_0^2(1/\omega_s^2 - 1/\omega_p^2)}}{r_0^2(1/\omega_s^2 - 1/\omega_p^2)} \tag{2.33}$$

If the pump and signal spotsizes that correspond to a certain fibre V-value for each wavelength are calculated using Whitley's formula [2]

$$\frac{\omega}{a} = 0.436 + 1.174V^{-1.5} + 0.698V^{-6} \tag{2.34}$$

(where a is the core radius) with

$$\frac{V_p}{V_s} = \frac{\lambda_s}{\lambda_p} \tag{2.35}$$

the following function was found to be a reasonable approximation for $S_0(p)$:

$$S_0(p) \approx \frac{C_{10}p + C_{11}}{C_{12}p + 1} \tag{2.36}$$

where C_i ($i=10$-12) are constants that depend on the pump and signal normalised spotsizes (see Appendix to Ch.2).

Fig.2.2 plots $S_0(p)/S_{\min}$ against the normalised intensity parameter p for two different values of the signal V-value. The signal wavelength is 1.56μm and the pump wavelength is 0.98μm. The solid curves were obtained by numerical integration of eqn.(2.31) and the dashed curves by direct evaluation of formula (2.36). It can be seen that the approximation holds very well over a wide range of signal V-values. Note, however, that Whitley's formula can be used only when the dopant radius r_0 is equal to the core radius a and that eqn.(2.36) is an approximate formula which holds only for the range of signal and pump spotsizes that are calculated using eqns.(2.34) and (2.35).

By use of the above approximation (eqn.(2.36)), the integrals of (2.29) and (2.30) may be determined yielding the following expressions for the integrated small-signal gain of

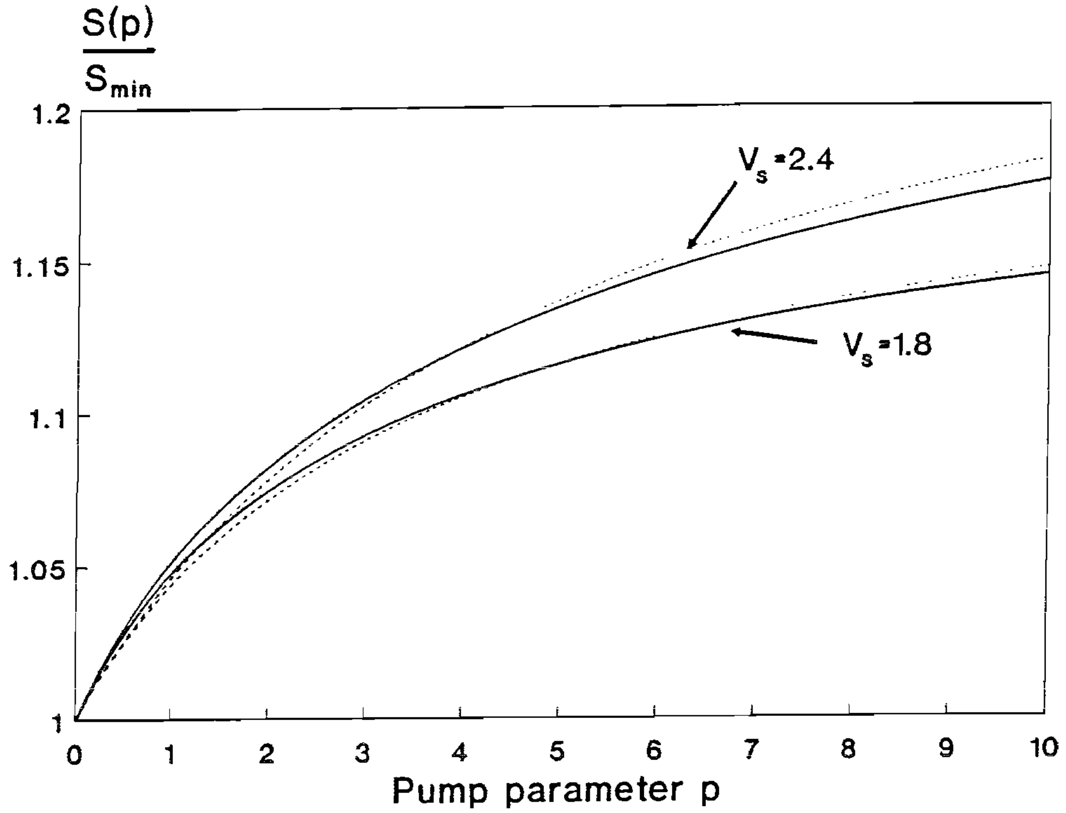

Fig.2.2 $S_0(p)/S_{min}$ vs normalised pump power p. Solid lines: numerical calculation of (2.31). Broken lines: Eqn.(A2.6)

3 and 4-level amplifiers:

$$\ln G^{4\text{-}level} = \frac{\sigma_{s_e}}{\sigma_{p_a}}\left(1 - e^{-r_0^2/\omega_s^2}\right)\frac{L}{L_0} + \frac{\sigma_{s_e}}{\sigma_{p_a}}\frac{\omega_p^2}{\omega_s^2}\left(S_{\min}\ln\alpha + (S_{\max} - S_{\min})\ln\left(\frac{\alpha C_{12}p(0)+1}{C_{12}p(0)+1}\right)\right) - \alpha_s L \quad (2.37)$$

$$\ln G^{3\text{-}level} = \frac{\sigma_{s_e}}{\sigma_{p_a}}\left(1 - e^{-r_0^2/\omega_s^2}\right)\frac{L}{L_0} + \frac{\left(\sigma_{s_e} + \sigma_{s_a}\right)}{\sigma_{p_a}}\frac{\omega_p^2}{\omega_s^2}\left(S_{\min}\ln\alpha + (S_{\max} - S_{\min})\ln\left(\frac{\alpha C_{12}p(0)+1}{C_{12}p(0)+1}\right)\right) - \alpha_s L \quad (2.38)$$

where

$$G \equiv \frac{P_s(L)}{P_s(0)} \quad (2.39)$$

is the small-signal gain of the 3 or 4-level fibre amplifier. Eqns.(2.37) and (2.38) give the small-signal gain of 3 and 4-level fibre amplifiers in analytical form, provided that α, the residual pump fraction at the amplifier end is known. This can be found by applying Newton's method to eqn.(2.19) or by solving numerically eqn.(2.17).

Case (b): Inclusion of pump background loss

By solving the integral on the denominator of the expression on the RHS of eqn.(2.31), S(p) can be written as

$$S(p) = \frac{S_0(p)}{1 - \frac{L_0}{L_p} p \left[\ln\left[\frac{p e^{-r_0^2/\omega_p^2} + 1}{p+1}\right]\right]^{-1}} \quad (2.40)$$

By using the approximation of eqn.(2.18) on the above equation, the integrals in eqns.(2.29) and (2.30) can determined, but the resulting expressions are complicated and cumbersome and hence a numerical approach is preferable.

2.2.4 Power-Dependent Overlaps and Optimum Cut-Off Wavelength

In order to maximise the gain of a fibre amplifier two parameters are of vital importance: (a) the existence of a good overlap between the signal spotsize and the inverted population and (b) the "interaction area" between the pump and the dopant must be made as small as possible. Increasing the numerical aperture (NA) of the fibre ensures that most of the signal and the pump power propagates inside the fibre core and helps to maximise the aforementioned overlap. The size of the "interaction area" is determined by both the NA and the fibre core radius a (and the dopant core radius as well, but in this analysis it has been assumed to be equal to the core radius). In fact, it transpires that there is an optimum (a NA) product that provides maximum amplifier gain for a given NA. This means that although increasing the fibre NA always results in higher amplifier gain, the fibre core-radius "a" should be decreased to provide the optimum (a NA) product. Since the cut-off wavelength $\lambda_c$is defined as

$$\lambda_c \equiv \frac{2\pi aNA}{2.405} = \frac{\lambda_k V_k}{2.405} \tag{2.41}$$

where k=(p,s), optimising the amplifier performance with respect to λ_c is then equivalent to optimising the (a NA) product.

For fibre amplifiers the optimum cut-off wavelength is usually defined as the wavelength that provides the maximum gain efficiency (eg dBs of gain / mW of launched pump power) under fully optimised conditions. That is, the length of the amplifier and the input pump power must be first optimised to provide the maximum possible gain efficiency. The case of a 4-level fibre amplifier with no signal background losses is the most simple; one has only to ensure that for every value of λ_c the length is sufficient to absorb all of the pump light. In this case, the optimum cut-off wavelength at low pump powers is determined by the requirement of a good overlap between the signal profile and the inverted population, ie such that most signal power propagates inside the region where there are inverted dopant ions. At low pump powers, the inverted population profile follows that of the pump and so the aforementioned overlap is a three-way overlap between the signal, inverted ion population and pump profiles. At high pump powers, the inverted population profile cannot follow the pump profile due to saturation effects and so the overlap is between the signal and the inverted ion profiles. Although this lowers the gain efficiency compared to the three-way overlap case, the optimum cut-off wavelength does not change significantly. For 3-level lasers the situation is more complicated: as the pump intensity across the dopant area varies, there will be signal absorption in the "wings" of its profile if there is insufficient pump light to provide gain in that region. In this case it is best to confine the inverted population in an area smaller than the core area, so that it only interacts with the central part of the pump and signal profiles.

The gain dependence on the overlaps leads to a definition of an effective core area A_{eff} which is pump power dependent. From eqns.(2.37) and (2.38) by substituting for $\ln\alpha$ from eqn.(2.19) and using again the approximation of eqn.(A2.2) in the Appendix, the expressions for the gain of 3 and 4-level amplifiers with no pump background losses become

$$\ln G^{4\text{-}level} \approx \frac{\sigma_{s_e}\tau_f}{h\nu_p}\,\frac{P_p(0)(1-\alpha)}{A_{eff}\left(P_p(0),P_p(L),NA,r_0\right)} - \alpha_s L \tag{2.42}$$

$$\ln G^{3\text{-}level} \approx \frac{(\sigma_{s_a}+\sigma_{s_e})\tau_f}{h\nu_p}\,\frac{P_p(0)(1-\alpha)}{A_{eff}\left(P_p(0),P_p(L),NA,r_0\right)} - \sigma_{s_a} N_{total}\left(1-e^{-r_0^2/\omega_s^2}\right)L - \alpha_s L \tag{2.43}$$

where

$$A_{eff}\left(P_p(0),NA,r_0\right) \equiv \pi r_0^2\,\Gamma\left(P_p(0),P_p(L),V_p,V_s\right) \tag{2.44}$$

and $\Gamma(P_p(0),P_p(L),V_p,V_s)$ is the value of the power-dependent overlap. Limiting expressions for this effective core area have appeared in the literature [5,6].

In the case of background pump losses the optimum cut-off wavelength shifts to higher values, because this ensures rapid pump absorption by the dopant ions and hence an increase in the pump absorption efficiency.

Fig.2.3 plots the gain efficiency of a praseodymium laser amplifier (4-level system) versus cut-off wavelength for six different cases. In all cases the length was chosen so that >99% of the pump light was absorbed and the signal background losses were set to zero. For curves (a), (b), (d) and (e) the pump backround losses were set to zero. Curves (a) and (b) correspond to an NA value of 0.20 and input pump powers 5mW for curve (a) and 1W for curve (b). In curve (a) the optimum cut-off is around 780nm, whereas for curve (b) the optimum occurs at 765nm with reduced gain eficiency throughout. This demonstrates the effect that the power-dependent overlap has on the gain efficiency and optimum cut-off wavelength of the amplifier. Curves (d) and (e) are analogous to curves (a) and (b) in terms of input pump powers (5mW for curve (d) and 1W for curve (e)) but the NA is 0.15 and the gain efficiency is significantly reduced. Since the pairs (a),(d) and (b),(e) share the same value for the optimum cut-off wavelengths (780 and 765nm respectively) it is evident that the optimum cut-off is independent of the fibre NA. These figures are in good agreement with results based on full numerical modelling of the amplifier (including ASE) predicting optimum cut-off wavelengths at 750nm [7] and 800nm [8].

Curves (c) and (f) include a pump background loss "absorption length" L_p (eq.(2.23)), 10 times higher than the dopant loss absorption length L_0. The values for the input pump powers and fibre NA's are 1W, 0.20 and 5mW, 0.15 respectively. The optimum cut-off wavelength has now shifted to 825nm and has become virtually independent of the input pump power.

In the case of erbium fibre amplifiers (3-level system) the situation is more complicated. For a given input pump power there exists an optimum amplifier length which maximises the gain (and hence the gain efficiency). Fig.2.4 plots the gain efficiency of an erbium amplifier (Y1 axis) at the optimum length L_{opt}/L_0 (Y2 axis) vs input pump power for three different values of the fibre cut-off wavelength. All background losses were set to zero for simplicity. As the three gain efficiency curves cross each other, it is evident that the optimum cut-off wavelength depends on the input pump power. As the pump power

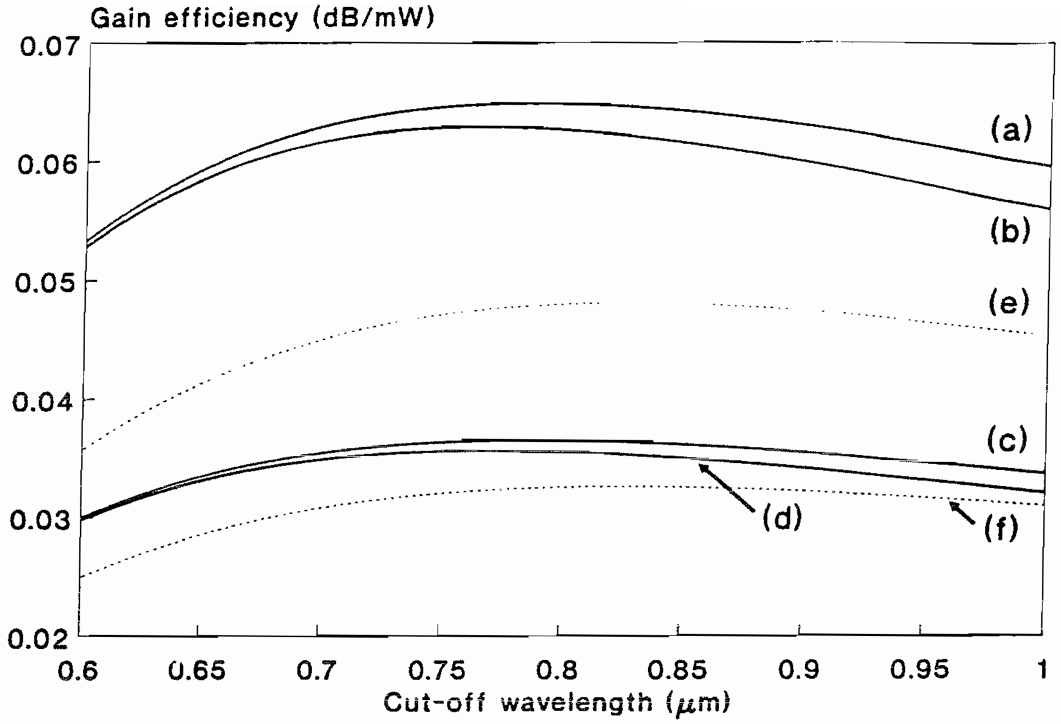

Fig.2.3 Pr^{3+} amplifier: Gain efficiency vs cut-off wavelength: (a),(b),(c) NA=0.2; (d),(e),(f) NA=0.15; (a),(d),(f) $P_p(0)$=5mW; (b),(c),(e) $P_p(0)$=1W; (a),(b),(d),(e) No pump background loss; (c),(f) L_0=1m, L_p=10L_0. σ_{pa}=0.429x10^{-25}m^2, σ_{se}=3.48x10^{-25}m^2 λ_p=1017nm, λ_s=1310nm, τ_f=110μs.

increases, however, the gain efficiency for each cut-off wavelength approaches a certain distinct maximum value which is different in each case. The optimum cut-off wavelength may be taken as the one that yields the best value for this gain efficiency limit and is therefore independent of the pump power. Fig.2.5 plots the gain efficiency vs cut-off wavelength at an input pump power of 20mW for two values of fibre NA. Y2 axis shows the value of the optimum length used for each point in normalised units. The cut-off wavelength that corresponds to maximum gain efficiency is around 835nm for both fibre NA's, again in good agreement with results derived using full numerical models predicting the optimum λ_c to be 800nm [9].

2.2.5 The Overlap Factor Γ and Self-locking

The eqns.(2.42-44) of the previous section show that minimising the overlap factor Γ leads to higher single-pass gains. This is, in fact, the principle behind passive "self-locking" in Ti:Sapphire systems, yielding pulses as short as 11fs with peak powers in excess of 100kW [10]. The mode-locking mechanism works as follows: During CW operation, third-order non-linear effects produce self-focusing of the lasing mode inside the gain medium and, as a result, the mode "shrinks" in dimension. Under certain optimised conditions, this effect leads to an increase in the mode overlap with the inverted population, producing higher gain with higher intracavity powers and hence pulsed operation is favoured. However, the relatively high self-starting pump powers (~6-10W) that are required makes this technique less attractive than the self-starting, passive mode-locking techniques that will be discussed and analysed in chapters three and four.

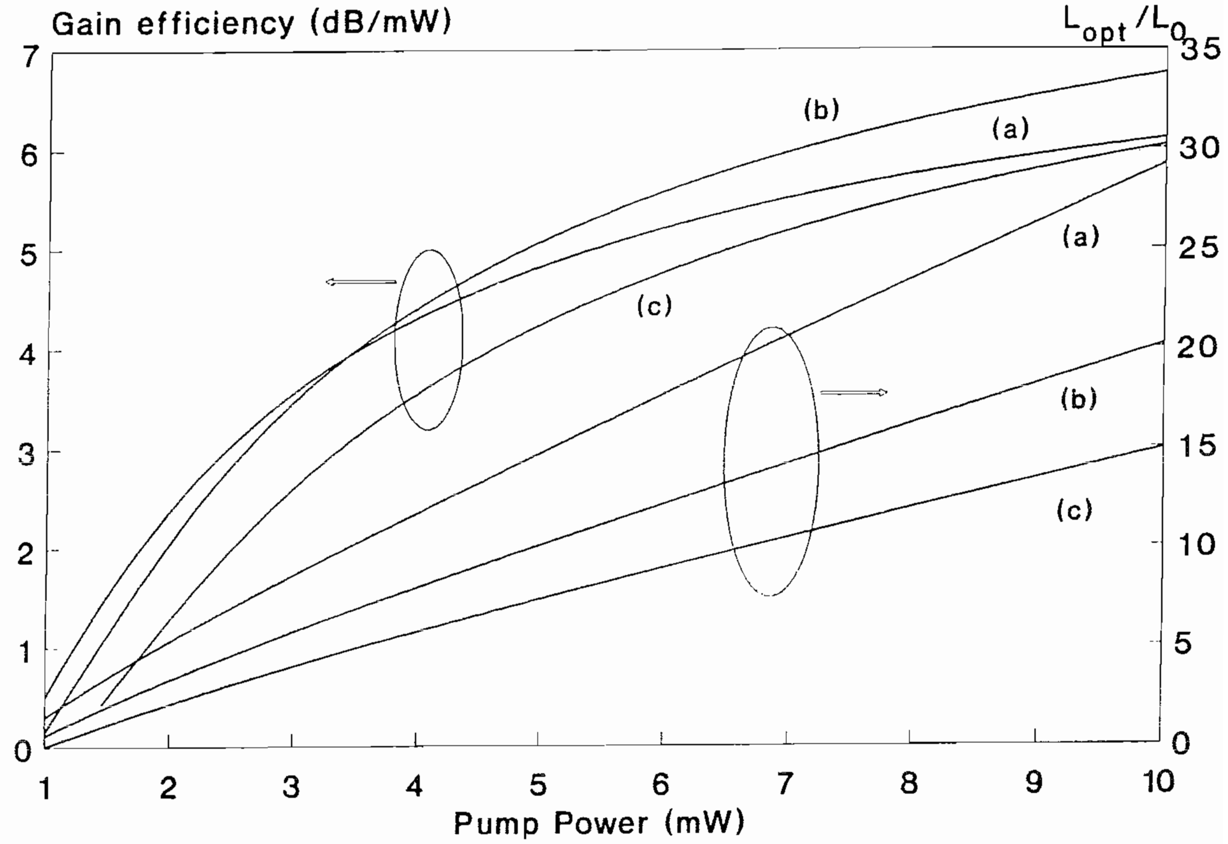

Fig.2.4 Er^{3+} amplifier: Pump power dependence of gain efficiency (Y1 axis) at the optimum length (Y2 axis) for three different values of cut-off wavelength: (a) 0.7μm, (b) 0.85μm and (c) 1μm. NA=0.2, $\sigma_{pa}=2.52\text{x}10^{-25}$, $\sigma_{sa}=7.9\text{x}10^{-25}$, $\sigma_{se}=7.11\text{x}10^{-25}$, λ_p=980nm, λ_s=1536nm, τ_f=12ms.

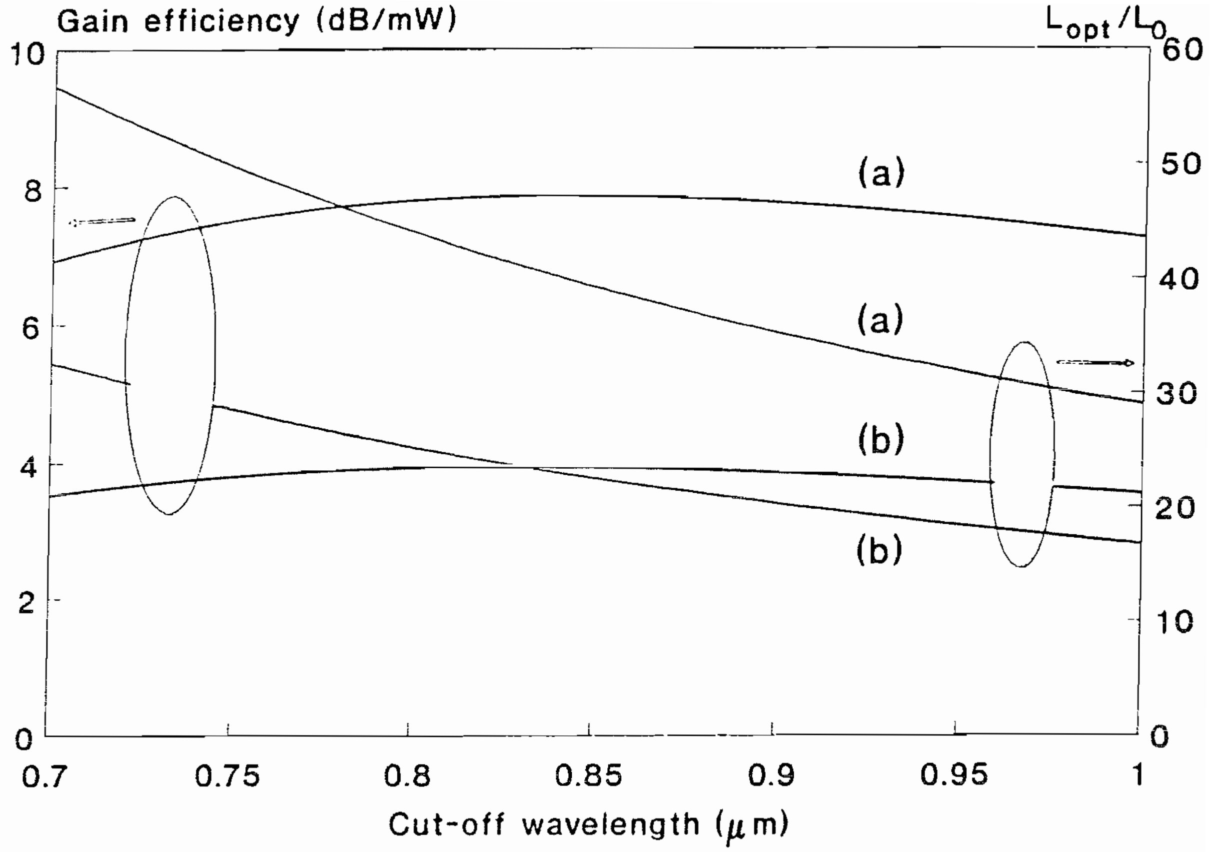

Fig.2.5 <u>Er^{3+} amplifier:</u> Gain efficiency vs cut-off wavelength at $P_p(0)=20$mW evaluated at the optimum length (Y2 axis) (a) NA=0.15, (b) NA=0.20. The rest of the other parameters are the same as in Fig.2.6.

2.2.6 Maximum Gain

To obtain an expression for the maximum gain for an amplifier of length L in the case of zero pump background losses, we let $\alpha \rightarrow 1$ in eqns.(2.37) and (2.38)

$$\ln G_{\max} = \left[\left(1 - e^{-r_0^2/\omega_s^2} \right) \sigma_{s_e} N_{total} - \alpha_s \right] L \tag{2.45}$$

In deriving this expression the effect of ASE has been neglected. In practice, the maximum achievable gain is limited by ASE. To find the corresponding maximum pump power that can be absorbed in a given amplifier of dopant volume V, we let $\alpha \rightarrow 1$ in eqn.(2.19):

$$P_{abs}^{\max} = \frac{h\nu_p}{\tau_f} N_{total} V \tag{2.46}$$

2.2.7 Gain Variation with Signal Wavelength

Erbium amplifiers have absorption and emission cross-sections that vary with wavelength and, as a consequence, the wavelength of maximum gain is a function of the input pump power. This effect is shown in Fig.2.6, in which the spectral gain of a GeO_2-Al_2O_3-SiO_2-type Er^{3+}-doped single mode fibre is plotted for various pump powers using eqn.(2.37) and published data [11] for the signal emission and absorption cross-sections σ_{se} and σ_{sa}. At low pump powers, the gain is maximum in the long wavelength ("red") side of the spectrum; as the pump power is raised, the point of maximum gain shifts to the "blue" side of the spectrum. Fig.2.7 is a graph of the wavelength at which lasing will occur as a function of the round-trip cavity loss. For graph (a) the fibre length used was 5 times the fibre absorption length L_0 whereas for graph (b) the length was 10 times the absorption length. The pump background loss was assumed to zero. Note that there are three discrete "windows" in which lasing occurs: the first is around 1.61μm, the second is around 1.56μm and the third is at 1.53μm. Note also that the "width" of the windows

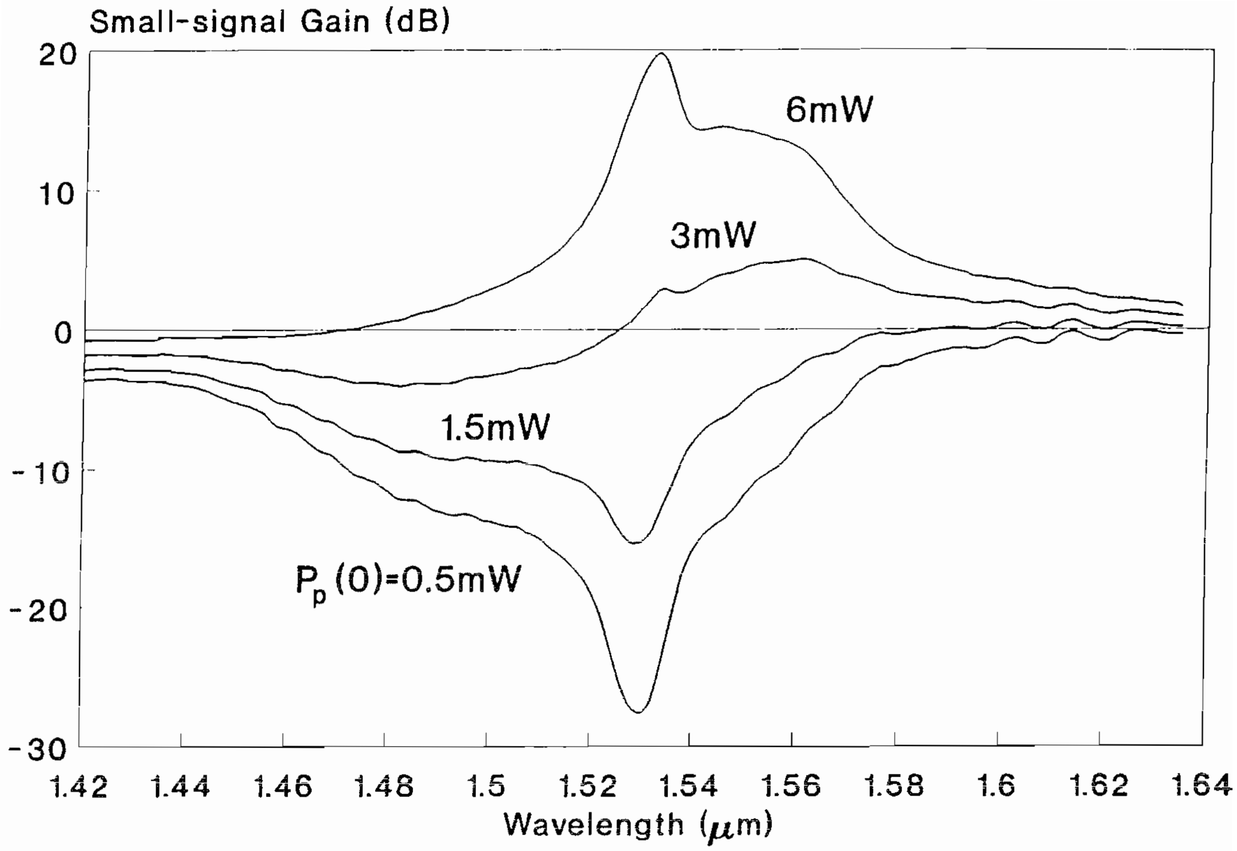

Fig.2.6 Er^{3+} amplifier: Gain dependence on wavelength and input pump power for a GeO_2-Al_2O_3-SiO_2-type fibre: NA=0.2, λ_c=835nm, L/L_0=10, τ_f=12ms.

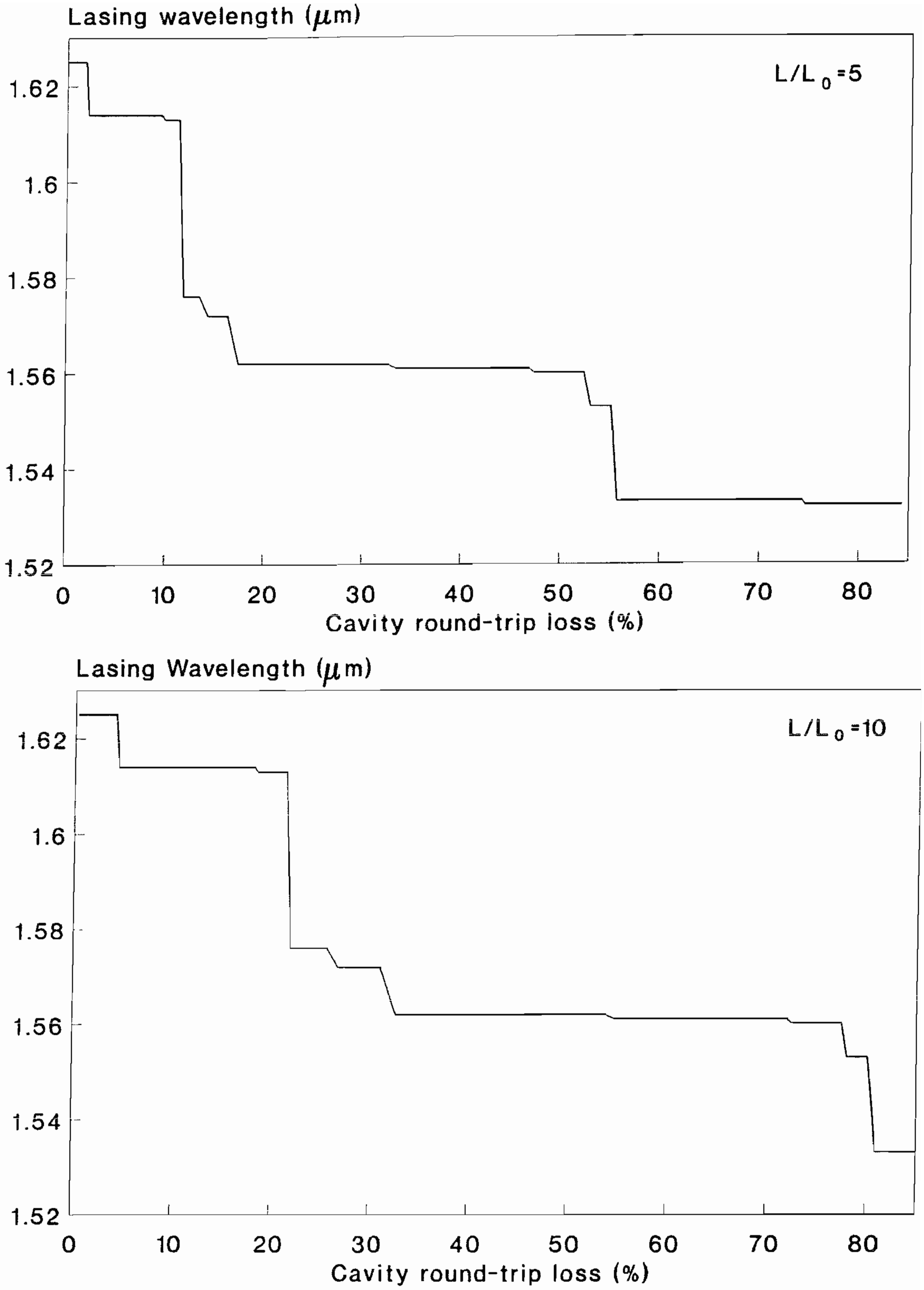

Fig.2.7 Er^{3+} fibre laser: Lasing wavelength vs cavity losses for the GeO_2-Al_2O_3-SiO_2-type fibre: (a) $L/L_0=5$ and (b) $L/L_0=10$. $NA=0.2$, $\lambda_c=835nm$, $\tau_f=12ms$.

(in terms of round-trip loss values) changes significantly with fibre length; the width of the 1.56μm window in graph (a), for example, spans a range of cavity loss between 15% and 55% whereas in graph (b) the span is broadened and shifted, ranging from 30% to 80%. These results are consistent with work published elsewhere [12,13]. This is a useful method to obtain a rough estimate of the laser intracavity losses, since estimates based on laser threshold calculations in 3-level systems involve large uncertainties. This is because the laser threshold in 3-level systems is only weakly dependent upon the intracavity losses, with pump saturation intensity being the most important factor. For example, the difference in the laser threshold across the range of cavity losses depicted in both graphs of Fig.2.7 was only a few mW.

The usefulness of this method of estimating the value of the cavity losses will become apparent in later chapters which deal with the passive mode-locked operation of fibre lasers.

2.3 CW FIBRE LASER CHARACTERISTICS

This section outlines the basic procedures that lead to laser threshold minimisation or output power maximisation in fibre lasers.

2.3.1 Fibre Laser Threshold Optimisation

The condition for laser oscillation in any laser cavity is

$$G_{rt}(1-Loss_{rt})=1 \tag{2.47}$$

where G_{rt} and $Loss_{rt}$ are the round trip intensity gain and fractional loss respectively. Since the expressions for the 3 and 4-level fibre amplifier gain are given in closed form with respect to the input pump power (due to the power-dependent effective area A_{eff}), no analytical expressions for a fibre laser threshold can be derived. At best, analytical expressions have been derived only for limiting values of A_{eff} [5,6] in the case of no pump background losses. It is therefore inevitable that an accurate optimisation of fibre laser threshold should be done by solving eqn.(2.47) numerically, using the 3 and 4-level amplifier gain expressions that were derived earlier.

In order to achieve full laser threshold optimisation, one has to find initially the optimum length for each value of fibre cut-off wavelength (all other parameters being constant). There will then be a specific (L_{opt}, λ_c) combination which provides the smallest threshold from all others. The value of fibre NA should be chosen as high as possible, provided that this is not at the expense of a reduced pump launch efficiency. In case there are no severe length restrictions due to background losses, the fibre length should be chosen to be at least a few times longer than the *critical* length L_c which, using eqn.(2.45), is given by

$$L_c=\frac{-\ln\sqrt{R}}{\left(1-e^{-r_0^2/\omega_s^2}\right)\sigma_{s_e}N_{total}-\alpha_s} \tag{2.48}$$

where R is the output coupling reflectivity. The critical length is the length below which no fibre laser will be able to reach threshold, no matter how hard it is pumped.

2.3.2 Fibre Laser Output Power Optimisation

The standard laser output characteristic is given by

$$P_{out}=\eta\left(P_p(0)-P_{thr}\right) \tag{2.49}$$

where P_{out}, P_{thr} are the laser output and threshold powers respectively and η is the laser slope efficiency. It represents the fraction of the input pump power above threshold that is converted to useful output laser power ie, by definition

$$\eta\equiv\frac{dP_{out}}{d(P_p(0)-P_{thr})} \tag{2.50}$$

Output power optimisation involves the determination of the unique combination of the parameters (R,L,λ_c), or, equivalently, (P_{thr},η), that yields maximum ouput power at a specified value of pump power.

In order to find an expression for η which includes cavity losses besides the laser output coupling, let's consider a laser cavity with constant circulating energy E_{circ}. The power that is dissipated maintaining this circulating energy is given by

$$P_{dis}=\frac{E_{circ}}{\tau_c}=P_p(0)-P_{thr} \tag{2.51}$$

where

$$\tau_c\equiv-\frac{T_{rt}}{\ln(R)+\sum_{i=1}^{N}\ln(1-L_i)} \tag{2.52}$$

with T_{rt} being the cavity round-trip time and L_i (i=1..N) being the values of various intracavity losses other than R.

Eqn.(2.51) can then be written as

$$\begin{aligned}P_p(0)-P_{thr}&=-\frac{E_{circ}}{T_{rt}}\left[\ln(R)+\sum_{i=1}^{N}\ln(1-L_i)\right]\\&\equiv P_{out}+P_{lost}\end{aligned} \tag{2.53}$$

where

$$\begin{aligned}P_{out}&=-\frac{E_{circ}}{T_{rt}}\ln(R)\\&=\left(P_p(0)-P_{thr}\right)\frac{\ln(R)}{\ln(R)+\sum_{i=1}^{N}\ln(1-L_i)}\end{aligned} \tag{2.54}$$

From this last equation it is evident that η_c, the part of the total slope efficiency that is due to various intrinsic intracavity losses, is given by

$$\eta_c = \frac{\ln(R)}{\ln(R) + \sum_{i=1}^{N} \ln(1 - L_i)} \qquad (2.55)$$

The total slope efficiency is then the product of the Stokes and pump absorption efficiencies with the coupling efficiency η_c:

$$\eta = \frac{\lambda_p}{\lambda_s}(1 - \alpha)\eta_c \qquad (2.56)$$

In the case of pump background losses the pump absorption efficiency $\eta_p = (1 - \alpha)$ should be replaced by

$$\eta_p \equiv \frac{\displaystyle\int_{P_p(0)}^{P_p(L)} \frac{\displaystyle\int_0^{r_0} N_1 e^{-r^2/\omega_p^2} 2\pi r dr}{\displaystyle\int_0^{r_0} N_1 e^{-r^2/\omega_p^2} 2\pi r dr + \frac{a_p}{\sigma_{p_a}} \pi \omega_p^2} dP_p}{P_p(0)} \qquad (2.57)$$

Other efficiencies such as the launch efficiency η_l, a pump fluorescent quantum efficinecy η_f [3] and an overlapping efficiency η_o may also be included, along with a corresponding modification for P_{thr}. The overlapping efficiency η_o appears in situations were the pump light is absorbed by atoms in places which are not "seen" by the signal and thus cannot contribute to any increase in the gain of the amplifier [14]. In such cases, the inverted population continues to build up in these areas even after lasing starts, as the lasing mode is unable to saturate the gain. In fibre lasers, however, where the signal spotsize is always larger than that of the pump, the values for η_o are very close to unity. The formula for the total slope efficiency, eqn.(2.56), is the same for both 3- and 4-level systems. It is interesting to note that signal reabsorption losses in 3-level lasers do not affect the laser slope efficiency. This is true, provided that there are no cavity losses other than the output coupling. In this case, signal photons that are absorbed by the ideal 3-level laser medium are not lost; they increase the population of the excited level and re-appear by stimulated emission back into the cavity; spontaneous emission can be ignored. If, however, there are other cavity losses present, some photons that are re-emitted are lost and so the circle of absorption and re-emission does not preserve energy as in the previous case. This results in a higher percentage of lost power than with no re-absorption taking place and a subsequent reduction in the slope efficiency.

2.4 CONCLUSIONS

This chapter has outlined the basic features of CW operation of fibre lasers and fibre amplifiers. The development of an analytical 3 and 4-level fibre amplifier model lead to the derivation of small-signal amplifier gain expressions, including the effect of the overlap variation between the signal and the inverted ion population with pump power. The optimum cut-off wavelength for the Pr^{3+} and the Er^{3+} fibre amplifiers for low or high pump power conditions and in the case of non-negligible pump background losses was estimated and found to be in good agreement with theoretical results published elsewhere. The amplifier model was then used to determine the lasing wavelength in Er^{3+} fibre lasers as a function of the intracavity losses. It was found that, depending on the cavity loss, any Er^{3+}-doped fibre laser will lase at one of three discrete lasing wavelengths, namely at 1.61, 1.56 or 1.53μm. The range of cavity loss values that correspond to each of these three wavelengths was found to depend on the fibre amplifier length. This information will be used in chapters 3 and 4 in which Er^{3+}-doped fibre laser configurations with active intracavity loss control are discussed. Optimisation methods for maximising a fibre laser's performance were also proposed.

REFERENCES:

1. D. Marcuse: "Loss analysis of single-mode fibre splices" *Bell Syst. J.* **56** p.703 (1977).

2. T. J. Whitley and R. Wyatt: "Alternative Gaussian spot size polynomial for use with doped fibre amplifiers" to be published in *IEEE Phot. Techn. Lett.*

3. A. Siegman: *Lasers*, Oxford University Press (1985).

4. F. F. Ruhl: "Prediction of optimum fibre lengths for erbium doped fibre amplifiers" *Electron. Lett.* **27** p.769 (1991).

5. T. J. Whitley and R. Wyatt: "Analytic expression for gain in an idealised 4-level doped fibre amplifier" WB2 In *Proc. OSA Topical Meeting on Optical Amps. and their Applications*, Santa Fe, New Mexico (1992).

6. P. Morkel: *Ph.D Thesis*, Southampton University (1990).

7. M. Kasarek: "Numerical analysis of Pr^{3+}-doped fluoride fibre amplifier" *IEEE Photon. Techn. Lett.* **4** p.1266 (1992).

8. B. Pedersen, W. J. Miniscalco and R. S. Quimby: "Optimisation of Pr^{3+}:ZBLAN fibre amplifiers" *IEEE Photon. Techn. Lett.* **4** p.446 (1992).

9. B. Pedersen, A. Bjarklev, O. Lumholt and J. H. Povlsen: "Detailed design analysis of Erbium-doped fibre amplifiers" *IEEE Photon. Techn. Lett.* **3** p.548 (1991).

10. M. Asaki, C. Huang, D. Garvey, J. Zhou, H. Kapteyn and M. Murnane: "Generation of 11-fs pulses from a self-mode locked Ti:sapphire laser" *Opt. Lett.* **18** p.977 (1993).

11. W. L. Barnes, R. I. Laming, E. J. Tarbox and P. R. Morkel: "Absorption and emission cross-section of Er^{3+} doped silica fibres" *IEEE J. Quant. Electron.* **QE-27** p.1004 (1991).

12. A. O. Nielsen, J. H. Povlsen, A. Bjarklev, O. Lumholt, T. P. Rasmussen and K. Rottwitt: "Fast method for accurate prediction of fibre laser oscillation wavelength" *Electron. Let.* **27** p.1644 (1991).

13. J. Chen, X. Zhu and W. Sibbett: "Derivation of the threshold pump power of erbium-doped fibre lasers" *Opt. Lett.* **17** p.926 (1992).

14. W. P. Risk: "Modelling of longitudinally pumped solid-state lasers exhibiting reabsorption losses" *J. Opt. Soc. Am. B* **5** p.1412 (1988).

APPENDIX TO CHAPTER 2

Approximation of eqn.(2.18):

A series expansion of the logarithmic function on the LHS of eqn.(2.18) yields

$$\ln\left[\frac{cp+1}{p+1}\right] = -\frac{p(1-c)}{p+1}\left[1-\frac{1}{2}\frac{p(1-c)}{p+1}+\frac{1}{3}\left[\frac{p(1-c)}{p+1}\right]^2-\ldots\right] \tag{A2.1}$$

provided $|p(1-c)/(p+1)| < 1$ where $c=\exp(-r_0^2/\omega_p^2)$. A second-order approximation to this function should then be a function of the form

$$\ln\left[\frac{cp+1}{p+1}\right] \approx -\frac{p(1-c)}{p+1}\left[1+\frac{\alpha p+\beta}{\gamma p+1}\right] \tag{A2.2}$$

For $p\to 0$, the above equation gives $\beta=0$ and for $p\to\infty$ we have $\alpha/\gamma=-(\ln(c)/(1-c)+1)$. Finally, for $p=1$ we have $2\ln((c+1)/2)=-(1-c)(1+\alpha/(\gamma+1))$. From the last two equalities we obtain

$$\alpha\equiv C_1=\frac{\left[\dfrac{2\ln\left[\dfrac{2}{c+1}\right]}{1-c}-1\right](\ln(c)+1-c)}{\ln c+2\ln\left[\dfrac{2}{c+1}\right]} \tag{A2.3}$$

$$\gamma\equiv C_2=-\frac{\left[\dfrac{2\ln\left[\dfrac{2}{c+1}\right]}{1-c}-1\right](1-c)}{\ln c+2\ln\left[\dfrac{2}{c+1}\right]} \tag{A2.4}$$

Approximation of eqn.(2.36):

Let $S_0(p)$ be approximated for $p>0$ by a hyperbolic function

$$S_0(p) \approx \frac{C_{10}p+C_{11}}{C_{12}p+1} \tag{A2.5}$$

From eqn.(2.30) with $\alpha_p=0$, $S_0(0)=S_{min}$, so $C_{11}=S_{min}$ and $S_0(\infty)=S_{max}$, so $C_{10}/C_{12}=S_{max}$. Eqn.(A2.5) is then equivalent to

$$S_0(p) \approx \frac{S_{max}C_{12}p+S_{min}}{C_{12}p+1} \tag{A2.6}$$

The formula for C_{12} that yielded the best results for a broad range of fibre V-values was empirically found to be

$$C_{12}=\frac{S_{min}\left(1-e^{-r_0^2/\omega_s^2}\right)\omega_s^2}{S_{max}^2 r_0^2} \tag{A2.7}$$

For $C_0 \equiv (1-\exp(-r_0^2/\omega_p^2))$, the values of the other constants are:

$$C_3=\frac{C_0}{2}\frac{L_p}{L_0} \quad ; \quad C_4=-C_2\frac{L_0}{L_p} \quad ; \quad C_5=-C_0(C_1+C_2)-\frac{L_0}{L_p}(1+C_2) \quad ; \quad C_6=-\left[C_0+\frac{L_0}{L_p}\right]$$

$$C_7=\frac{-C_0^2(C_1+C_2)-C_0\frac{L_0}{L_p}(C_2+2C_1-1)}{L_0/L_p\sqrt{b^2-4ac}} \quad ; \quad C_8=\frac{2a}{\sqrt{b^2-4ac}} \quad ; \quad C_9=\frac{b}{\sqrt{b^2-4ac}}$$

where $a=-C_4$, $b=C_0(C_1+C_2)+L_0/L_p-C_4$, $c=-(C_0+L_0/L_p)$

CHAPTER 3

PASSIVE MODE-LOCKING OF FIBRE LASERS I: SQUARE PULSES, SOLITONS AND SAGNAC LOOP MIRRORS

3.1 INTRODUCTION

Following the brief discussion on the main features of continuous wave (CW) operation of fibre lasers presented in the previous chapter, the rest of this thesis will be concerned with mode-locked fibre laser operation. Whereas in (multimode) CW operation the output power is effectively delivered continuously with the laser modes oscillating with random phases and amplitudes, in mode-locked operation the laser modes are "in phase" with one another and the output power is delivered in ordered, discrete packets of energy at time intervals equal to the cavity round trip time or multiples thereof. The standard way to achieve mode-locked operation is to provide a mechanism which discriminates against CW operation by ensuring a higher round-trip loss for CW radiation. This fact is based on the observation that a laser will, in general, operate in the mode having the lowest loss, since it is always the mode with the lowest loss (ie the longest cavity lifetime) that saturates the gain. However, additional requirements may also have to be met: for example, in many passively mode-locked systems the mean intracavity intensity needs to be above a certain critical value for the mode-locking to be initiated from a noise fluctuation.

There are two kinds of laser mode-locked operation termed either active or passive mode-locking. Active mode-locking involves a systematic and periodic modulation of the intracavity loss, the modulation period being equal to the cavity round-trip time or a multiple thereof (harmonic mode-locking). This is achieved by placing an acousto-optic or electro-optic modulator inside the laser cavity. Passive mode-locking on the other hand requires an intensity-dependent cavity loss, with the loss decreasing with increasing intracavity laser intensity. This is achieved by placing an intracavity element which exhibits a "saturable" loss, such that the transmission of light through it will increase if the laser intensity increases. The advantages of passive and active mode-locking for short pulse production depend on the application, as each has distinct characteristics:

Active mode-locking is more controllable than passive mode-locking in terms of desired pulsewidth, repetition rate and pulse-to-pulse stability. The disadvantage of this method is that the minimum pulsewidth and maximum repetition rate of pulse production are limited by the "speed" or bandwidth of the modulating element. However, during the last decade there has been considerable improvement in modulator design and now quoted bandwidths are well into the gigahertz regime. As a result, light pulses of only a few picoseconds duration at gigahertz repetition rates and with peak powers of tens of watts can be produced [1-3]. A brief analysis of active mode-locking, based on a theory by Kuizenga and Siegman, is presented in Chapter 5.

For the generation of ultra-short (<1ps) pulses, on the other hand, passive mode-locking is required. By using the broad gain bandwidth of the Ti:Sapphire laser, this method has recently produced pulses as short as 11fs [4], corresponding to a pulse of only a few optical cycles long. Since passive mode-locking relies upon the magnitude of the intracavity laser light intensity for the modulation of the cavity loss, its main drawback is its inevitable dependence upon stochastic variables and probabilities; in some cases the laser may not display a well-defined, reproducible mode-locked behaviour. In such cases both active and passive methods may be used simultaneously: the passive mechanism is used to dictate the pulse duration and shape, while the active mechanism ensures pulse stability.

As was mentioned earlier, passive mode-locking involves the use of an intracavity element with an intensity-dependent transmission which acts as, or is, a saturable absorber. For laser systems with a gain recovery time much longer than the cavity round-trip time, such as most solid-state lasers, one has to ensure that the recovery time of the saturable absorber action, ie the time required for its transmission to revert to its original value if the magnitude of the light intensity is instantaneously dropped, is of the same order of magnitude, or less, than the pulsewidth that one wishes to produce. This condition is well satisfied in the recently developed femtosecond systems [5] which rely upon the fast (<10fs) non-resonant Kerr-type nonlinearity of a passive modulator as the underlying mechanism to provide the saturable absorber action needed for passive mode-locking. Two such passive modulators, namely the non-linear optical loop mirror (or non-linear Sagnac loop) and the non-linear polarisation evolution switch are extensively described and analysed in this thesis. These are perfect examples of a class of optical devices generally named as "non-linear switches": "non-linear" because their operation relies on the non-linear propagation of light in the material and "switch" because of their transmission characteristic. The present chapter will analyse the use of the fibre Sagnac loop mirror as a non-linear switch for passive mode-locking of fibre lasers and will discuss its relevance for soliton pulse generation. Two fibre laser configurations that utilise these non-linear characteristics of the fibre Sagnac loop for passive mode-locking purposes will then be presented along with experimental results.

3.2 LINEAR CHARACTERISTICS OF SAGNAC LOOPS

A Sagnac loop is formed when the two output ports of a fibre coupler are spliced together as shown in Fig.3.1a. Fig.3.1b shows the analogous configuration using bulk optics. Light launched through port #1 is split into two counter-propagating waves which return to recombine in the coupler region after time T_{tr}, the loop transit time. Depending on the coupler's splitting ratio α:1-α, some of the launched light will emerge from port #1, the input port, while the rest will exit through port #2, the output port or "switching" port. The transmission of light from port #1 to port #2 via the loop is represented by the loop "transmission" or "transfer" function $T(\lambda,\alpha)$. The following analysis will produce a simple formula that describes the fibre Sagnac loop transmission in the presence of birefringence inside the loop. Although based on the assumption that polarisation-maintaining fibres are used to form the Sagnac loop, similar results are expected when ordinary, non-polarisation maintaining fibres are used, combined with polarisation controllers to control the light polarisation inside the loop.

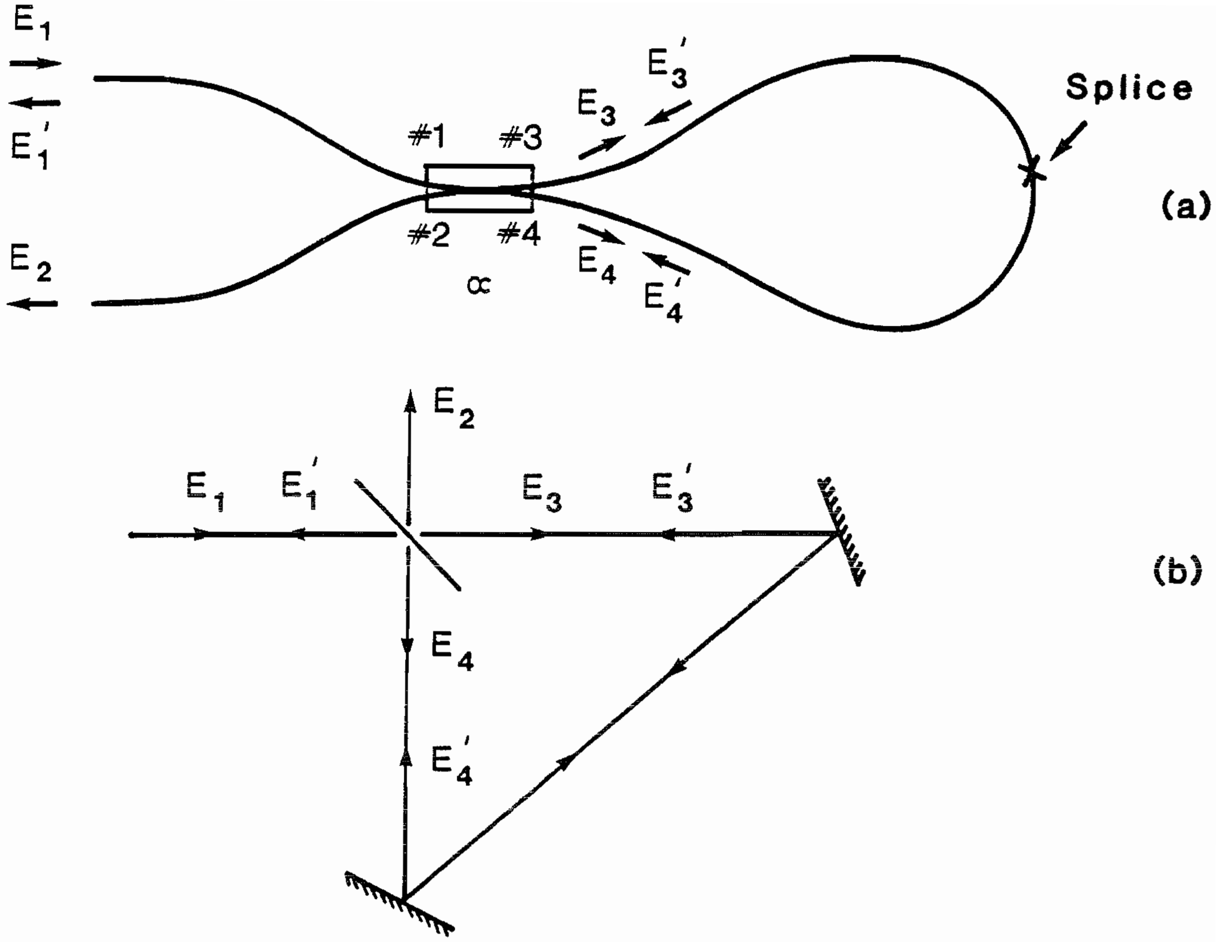

Fig.3.1 (a) An optical fiber Sagnac loop mirror (b) The analogous configuration using bulk optics.

3.2.1 Theoretical Analysis of the Fiber Sagnac Loop

Suppose light with electric field components E_{1x}, E_{1y} is launched at port #1 of a lossless four-port coupler which has ports #3 and #4 connected with a Hi-Bi fibre and the ends of the Hi-Bi fibre at the coupler ports are aligned so that the respective birefringence axes are parallel (Fig.3.2). A reference coordinate system may then be chosen with axes parallel to these birefringence axes. It is assumed that there is a splice inside the loop at distance L_1 from port #3 and distance $L_2=L-L_1$ from port #4. Let Ω_1, Ω_2 denote the two rotation angles of the birefringent axes, at L_1 and L_2 respectively, from their original orientations. Then the algebraic sum of these two angles represents the respective "misalignment" angle of the splice, ie a measure of how well aligned the two Hi-Bi axes are after splicing. We can write the following equations for the field components immediately after the splitting of the field at the coupler: For port #3

$$\begin{aligned} E_{3x} &= \alpha^{1/2} E_{1x} \\ E_{3y} &= \alpha^{1/2} E_{1y} \end{aligned} \tag{3.1}$$

and for port #4

$$\begin{aligned} E_{4x} &= j(1-\alpha)^{1/2} E_{1x} \\ E_{4y} &= j(1-\alpha)^{1/2} E_{1y} \end{aligned} \tag{3.2}$$

where the j factor indicates a $\pi/2$ phase change. Using Jones calculus [6] on these field vectors we can write the following matrix equations for the field components after counter-propagating inside the loop and are about to recombine at ports #3 and #4:

$$\begin{bmatrix} E'_{4x} \\ E'_{4y} \end{bmatrix} = (\ I\ )(\Omega_2)(\Omega_2)(L_2)(-\Omega_2)(\Omega_1)(L_1) \begin{bmatrix} E_{3x} \\ E_{3y} \end{bmatrix} \tag{3.3}$$

$$\begin{bmatrix} E'_{3x} \\ E'_{3y} \end{bmatrix} = (\ I\ )(\Omega_1)(\Omega_1)(L_1)(-\Omega_1)(\Omega_2)(L_2) \begin{bmatrix} E_{4x} \\ E_{4y} \end{bmatrix} \tag{3.4}$$

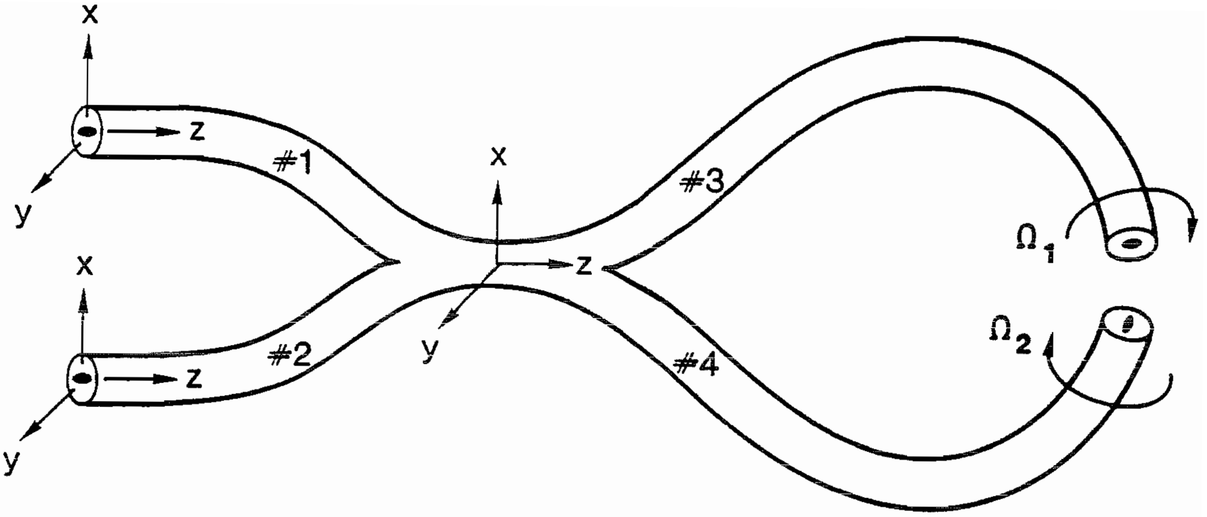

Fig.3.2 Schematic diagram for the Sagnac loop model.

where

$$(L_i) \equiv \begin{bmatrix} e^{j\beta_x L_i} & 0 \\ 0 & e^{j\beta_y L_i} \end{bmatrix} = e^{j\beta_x L_i} \begin{bmatrix} 1 & 0 \\ 0 & e^{j\Delta\beta L_i} \end{bmatrix} \equiv e^{j\beta_x L_i} (L_i^{/}) \qquad i=1,2 \tag{3.5}$$

$$(\Omega_i) \equiv \begin{bmatrix} \cos\Omega_i & -\sin\Omega_i \\ \sin\Omega_i & \cos\Omega_i \end{bmatrix} \qquad i=1,2 \tag{3.6}$$

and

$$(I) \equiv \begin{bmatrix} 1 & 0 \\ 0 & -1 \end{bmatrix} \tag{3.7}$$

is a matrix which indicates that E_{ij}' (i=3,4 j=x,y) are now with respect to a right-handed coordinate system with the same x-axis as the original but, with the z-axis pointing in the opposite direction. This is done to account for the reversal in the direction of the two counter-propagating fields. Eqs.(3.3) and (3.4) can be re-written as

$$\begin{bmatrix} E_{4x}^{/} \\ E_{4y}^{/} \end{bmatrix} = e^{j\beta_x L} (I) (2\Omega_2) (L_2^{/}) (\Omega_1 - \Omega_2) (L_1^{/}) \begin{bmatrix} E_{3x} \\ E_{3y} \end{bmatrix} \tag{3.8}$$

$$\begin{bmatrix} E_{3x}^{/} \\ E_{3y}^{/} \end{bmatrix} = e^{j\beta_x L} (I) (2\Omega_1) (L_1^{/}) (\Omega_2 - \Omega_1) (L_2^{/}) \begin{bmatrix} E_{4x} \\ E_{4y} \end{bmatrix} \tag{3.9}$$

In order to simplify the algebra, but without any loss of generality, Ω_2 and L_2 are set equal to zero, and from now on Ω_1 and L_1 will be denoted as Ω and L respectively. Eqns.(3.8) and (3.9) then simplify to

$$\begin{bmatrix} E'_{4x} \\ E'_{4y} \end{bmatrix} = e^{j\beta_x L}(I)(\Omega)(L'_1)\begin{bmatrix} E_{3x} \\ E_{3y} \end{bmatrix} \tag{3.10}$$

$$\begin{bmatrix} E'_{3x} \\ E'_{3y} \end{bmatrix} = e^{j\beta_x L}(I)(2\Omega)(L'_1)(-\Omega)\begin{bmatrix} E_{4x} \\ E_{4y} \end{bmatrix} \tag{3.11}$$

The transmission function $T(\lambda,\alpha)$ is given by

$$T(\lambda,\alpha)=\frac{|E_{2x}|^2+|E_{2y}|^2}{|E_{1x}|^2+|E_{1y}|^2} \tag{3.12}$$

and by setting $|E_{1x}|^2+|E_{1y}|^2=1$, $T(\lambda,\alpha)=|E_{2x}|^2+|E_{2y}|^2$ where

$$\begin{aligned} E_{2x}&=E'_{4x}\alpha^{1/2}+j(1-\alpha)^{1/2}E'_{3x} \\ E_{2y}&=E'_{4y}\alpha^{1/2}+j(1-\alpha)^{1/2}E'_{3y} \end{aligned} \tag{3.13}$$

From eqns.(3.12) and (3.13), using eqns.(3.10) and (3.11) and the identity $|E_{ij}|^2=E_{ij}E_{ij}^*$ (i=1-4, j=x,y) the following formula is obtained for the transmission function:

$$T_b(\lambda,\alpha)=(1-2\alpha)^2+2\alpha(1-\alpha)\sin^2\Omega[1-\cos(\Delta\beta L)] \tag{3.14}$$

where the b subscript denotes a birefringent loop. Since

$$\alpha=\alpha(\lambda)=\sin^2 C(\lambda) \tag{3.15}$$

where

$$C(\lambda)=\frac{\lambda}{\lambda_{3dB}}C_{3dB}\quad,\quad C_{3dB}=\frac{n\pi}{4} \tag{3.16}$$

n being the coupling cycle, λ_{3dB} the $\alpha=0.5$ wavelength and $\Delta\beta=2\pi/L_{b0}$, where L_{b0} is the natural beat length of the birefringent fiber ($=\lambda/\Delta n$), eqn.(3.14) can be used to give us information about the dependence of the power switched from port #1 to port #2 on α, Ω, L/L_{b0} (the number of beat lengths contained in the loop length L) and λ, the wavelength of the launched light, since both α and L_{b0} depend on it. Note that $T(\lambda,\alpha)$ is independent of the input state of polarization but the output polarisation state is in general dependent on the input polarisation state.

The various regimes of operation may now be identified from eqn.(3.14). Setting $\Omega=0$ we obtain the normal, birefringent-free characteristic ie $T_0=(1-2\alpha)^2$. Likewise, setting $\Omega\neq0$ and $L/L_{b0}=N$ (N=1,2,..., ie L is an integral number of beat lengths) the same birefringent-free formula is obtained. In order to see any birefringence effects both $\Omega\neq0$ and $L/L_{b0}\neq N$ should hold true. Fig.3.3 shows how T depends on the ratio L/L_{b0} at a particular wavelength, taking $\alpha=0.5$ and varying Ω from 0^0 to 90^0. We see that there is complete power transfer from port #1 to port #2 when $L/L_{b0}=0.5$ or odd multiples thereof.

Figs.3.4a-d and 3.5a-d show how birefringence degrades the normal $\sin^2(2C)$ wavelength dependence of $T(\lambda,\alpha)$ for various misalignment angles. For Figs.3.4a-d, L/L_{b0} was set equal to 3/2 at 1.5μm and for Figs.3.5a-d, L/L_{b0} was set equal to 101/2 at the same wavelength. α was chosen to be equal to 0.5 at 1.5μm and n was set equal to 3. Note that Ω plays the role of the "degradation amplitude" as defined in Ref.[7].

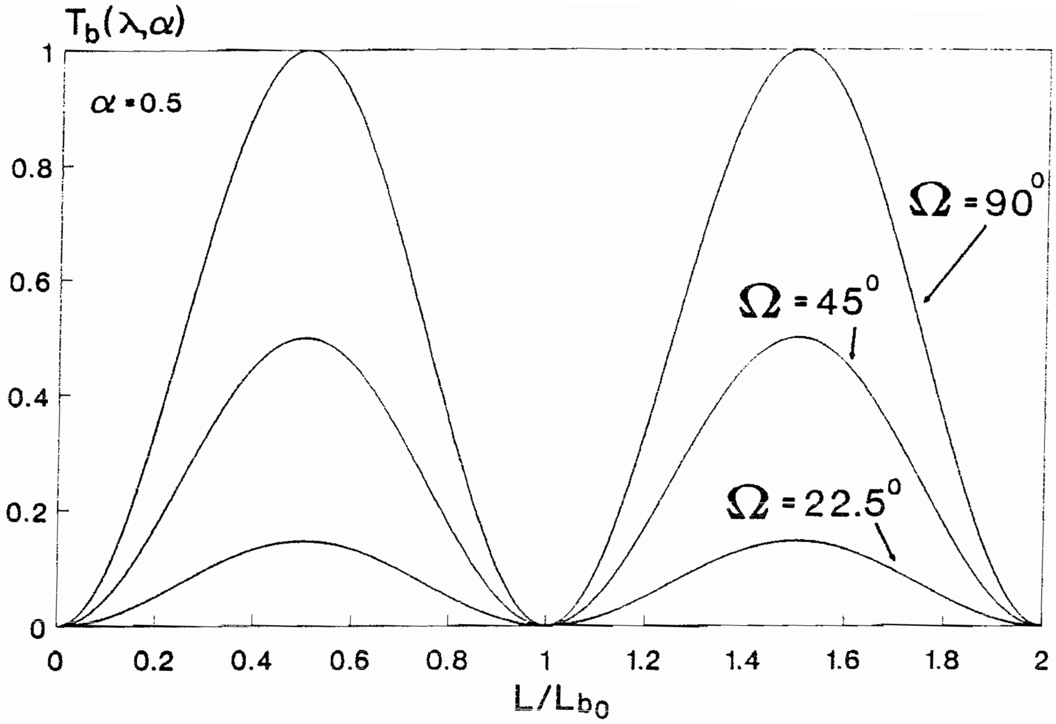

Fig.3.3 Birefringent loop transmission $T_b(\lambda,\alpha)$ as a function of the number of beat lengths L/L_{b0} for various values of the misalignment angle Ω. α is set equal to 0.5.

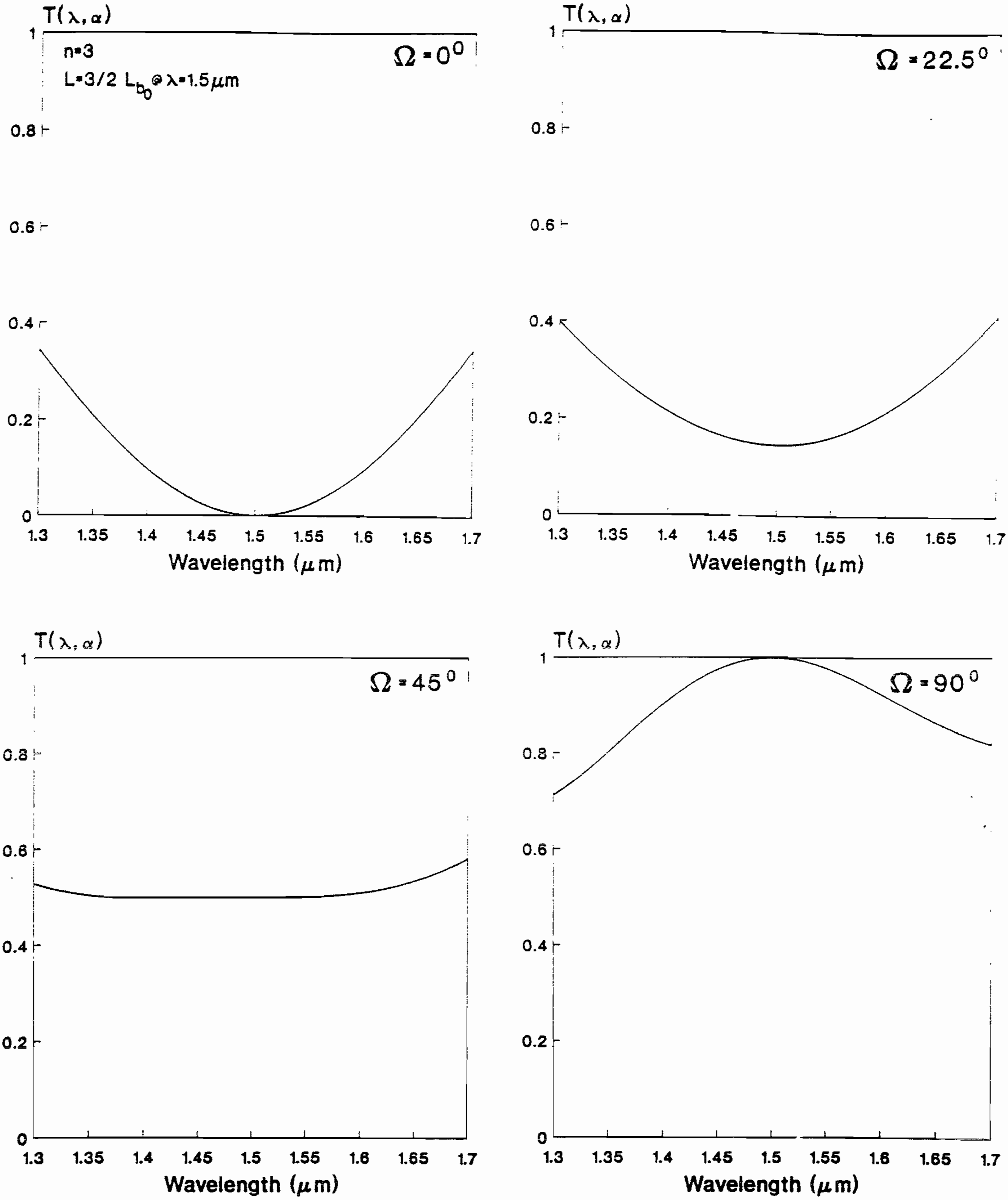

Fig.3.4 Degradation of the normal (birefringent-free) loop transmission $T_b(\lambda,\alpha)$ as a function of wavelength for various values of Ω. Calculated for $\alpha=0.5$ at $\lambda=1.5\mu m$, $n=3$ and $L/L_{b0}=3/2$ at $\lambda=1.5\mu m$.

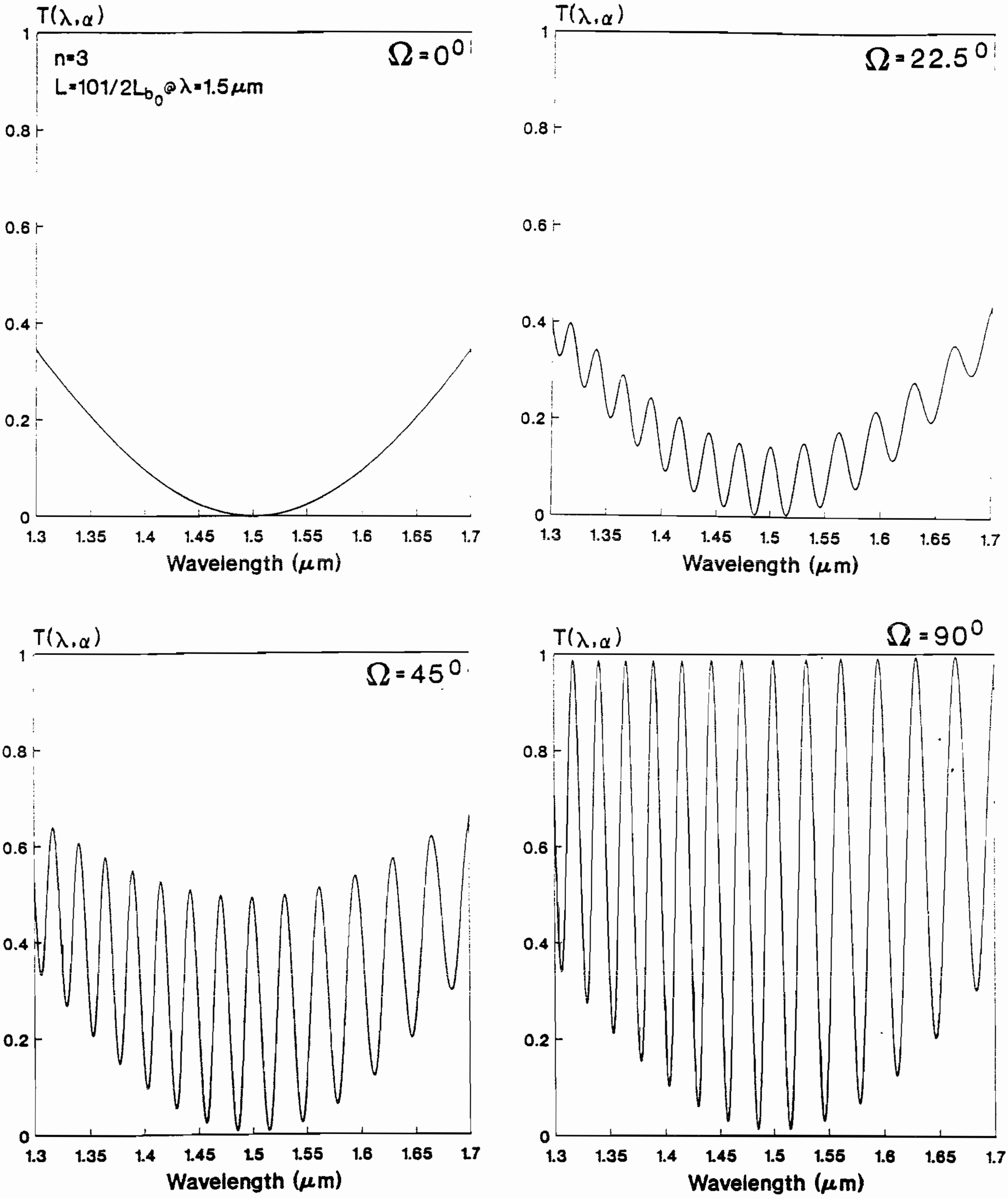

Fig.3.5 Same as Fig.3.4 but with $L/L_{b0}=101/2$ at $\lambda=1.5\mu m$.

3.3 NON-LINEAR CHARACTERISTICS OF THE SAGNAC LOOP

3.3.1 Introduction

Since an optical fiber has an intensity-dependent refractive index due to $\chi^{(3)}$ effects, unless $\alpha=0.5$ the optical lengths for the two counter-propagating waves of different intensities inside the Sagnac loop will be different and, as a result, the loop transmission function becomes intensity-dependent. Section 3.3.2 examines this effect in detail and will demonstrate its use for pulse switching. Section 3.3.3 reviews some of the basic theory governing soliton propagation in optical fibers and prepares the ground for section 3.3.4 in which soliton switching in the Sagnac loop is discussed.

3.3.2 Square Pulse Switching

The transmission function of a birefringent Sagnac loop, when the input light intensity is strong enough to cause significant non-linear effects, cannot be described by any general analytical formula. The transmission is no longer independent of the input state of polarisation because the non-linearity couples the two orthogonal polarisation components of each wave, thus making their evolution dependent on the initial conditions (ie the state of polarisation at the input of the loop). Numerical methods have been used to evaluate the loop transmission characteristics in this regime [8]. There are, however, two special cases in which it is possible to derive an analytical formula:

Case (a): Birefringent-free loop

Provided the input polarisation is linear and assuming there is no linear birefringence in the Sagnac loop, ie ($\beta_x=\beta_y=\beta$) the intensity-dependent propagation constant β may be written as

$$\beta=\frac{2\pi}{\lambda}(n_0+n_2I)\equiv\beta_0+\beta_{NL} \tag{3.17}$$

where n_0 and n_2 are the linear and non-linear refractive indices respectively. The previous analysis yields the following result for the transmission function

$$T_{NL}(\lambda,\alpha)=1-2\alpha(1-\alpha)\{1+\cos[(1-2\alpha)\beta_{NL}L]\} \tag{3.18}$$

which agrees with the formula derived in Ref.[9]. Fig.3.6 shows a graph of $T(\lambda,\alpha)$ vs a power-length product (PL) at a wavelength of $1.5\mu m$ and an effective area A_{eff} (=P/I) of $30\mu m^2$. It can be seen that full switching occurs at periodic intervals, the period being dependent on α. For small α the switching power-length product required is small, but the contrast is poor. As α approaches 0.5, the contrast is increased but at the expense of a higher power-length product required for full switching. This finally becomes infinite at $\alpha=0.5$. When the Sagnac loop is operating in the non-linear regime, it will be refered to as a Nonlinear Optical Loop Mirror (NOLM).

It has been shown [10] that the value of the power-length product requirement for switching may be radically reduced by including a fibre amplifier in one arm of the loop as shown in Fig.3.7. The counter-propagating field intensities now differ by $(1-(G+1)\alpha)$ instead of $(1-2\alpha)$ as in the previous case. The transmission function is now

$$T_{NL}(\lambda,\alpha)=1-2\alpha(1-\alpha)\{1+\cos[(1-\alpha(G+1))\beta_{NL}L]\} \tag{3.19}$$

and using a 50:50 coupler full contrast can be achieved at extremely low switching power-length products (200μW for 336m has been reported [11]). A NOLM which includes gain inside will be referred to as NALM (Nonlinear Amplifying Loop Mirror).

Case (b): Birefringent loop with $\Omega=90^0$

In the case of a birefringent loop with $\Omega=90^0$, assuming again linearly polarised input, the loop transmission (including gain) is given by

$$T_{b,NL}^{\Omega=90^0}(\lambda,\alpha)=1-2\alpha(1-\alpha)\left\{1+\cos\left[(1-\alpha(G+1))\beta_{NL}L+\Delta\beta L\right]\right\} \tag{3.20}$$

Compare eqn.(3.19) with eqn.(3.20): The argument of the cos term, which indicates the "bias" of the loop, now includes the extra $\Delta\beta L$ term. Fig.3.8 plots eqn.(3.20) for $\Delta\beta L=\pi$, all other parameters being the same as in Fig.3.6. It can be seen that the loop transmission characteristic is now exactly the reverse of what it was in Fig.3.6. Section 3.4.2 will report on a fibre laser cavity arrangement that utilises this "biasing" feature

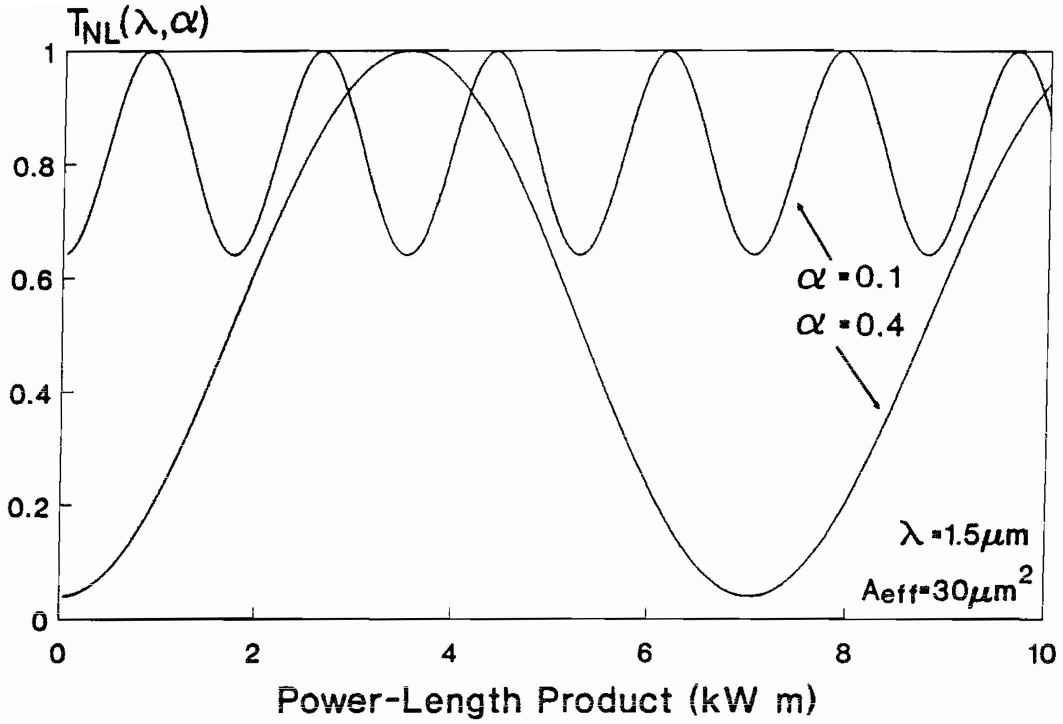

Fig.3.6 Graph of $T_{NL}(\lambda,\alpha)$ (eqn.(3.11)) vs the power-length product.

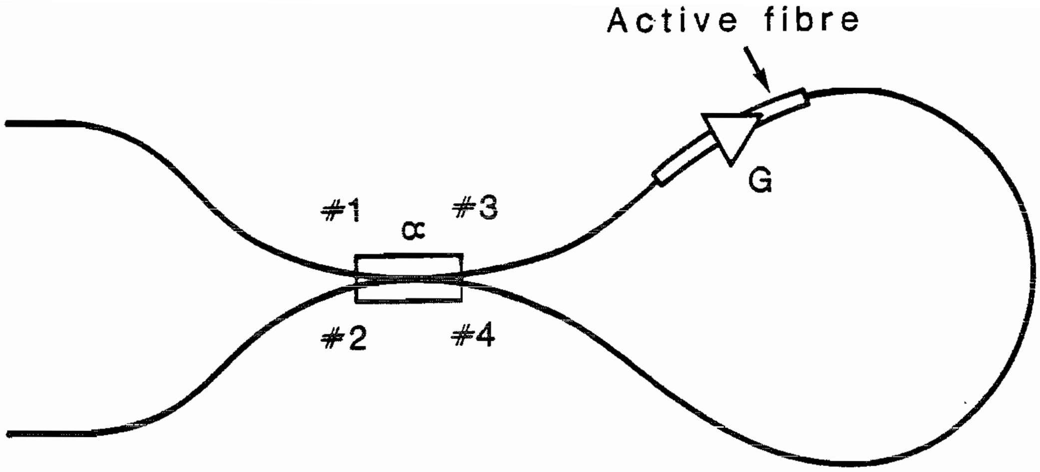

Fig.3.7 A nonlinear amplifying Sagnac loop mirror.

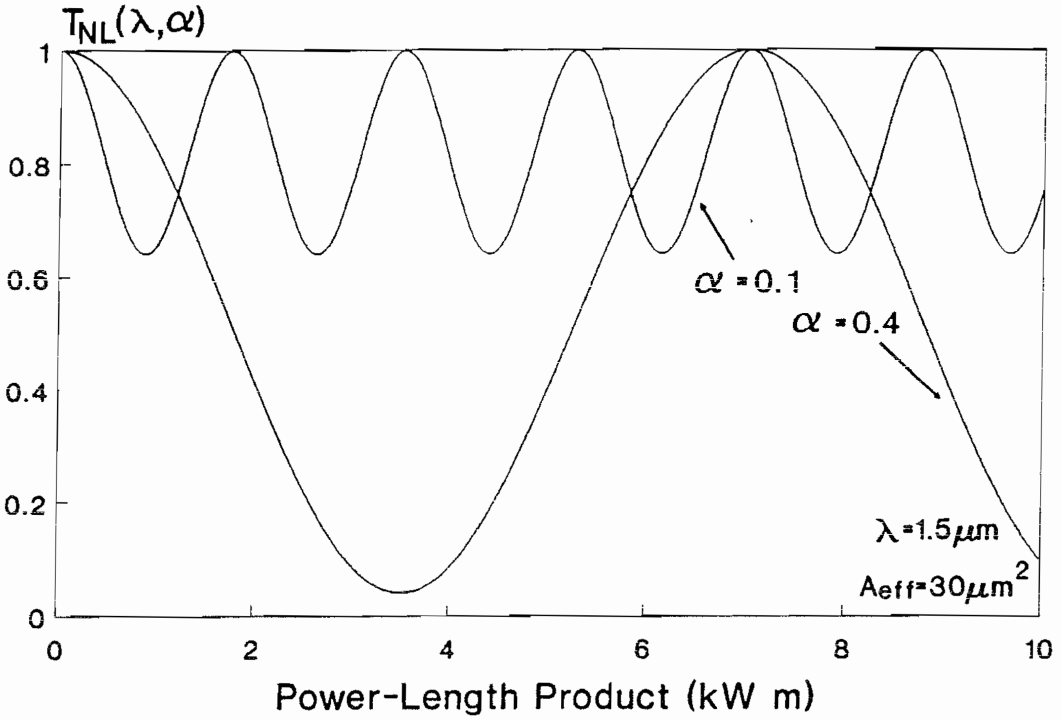

Fig.3.8 Graph of $T_{b,NL}(\lambda,\alpha)$ at $\Omega=90_0$ (eqn.(3.13)) vs the power-length product. All other parameters are the same as in Fig.4.6.

of the Sagnac loop for passive mode-locking.

The above results were derived assuming a single value for the input intensity at port #1. In practice, the finite rise and fall times of an input pulse will in general give rise to a distorted switched output pulse, since the switching action depends on the instantaneous intensity. Under certain conditions, however, solitons are able to propagate and the pulse shape is preserved. In order to understand the operation of the NOLM/NALM in this soliton regime, the following section will provide a brief introduction to the fundamental principles of soliton propagation in optical fibres. For a more detailed discussion the reader is referred to Ref.[12].

3.3.3 Soliton Propagation in Optical Fibres

It has been theoretically predicted [13] and consequently demonstrated experimentally [14] that the equation of motion for signals propagating through optical fibers can accept soliton solutions, provided certain conditions are satisfied. The soliton solutions that exist when the second-order derivative of the propagation constant of the fundamental mode in the fiber (β_2) is negative, take pulse forms with profiles that repeat themselves in a periodic fashion as the pulse propagates. The soliton "order" refers to the particular pattern that this periodic evolution follows. The equation of motion for the envelope of a light wave propagating through an optical fiber in the presence of an intensity-dependent refractive index and group-velocity dispersion is, with appropriate transformations, reduced to the non-linear Schrödinger equation:

$$i\frac{\partial u}{\partial z}+\frac{1}{2}\frac{\partial^2 u}{\partial t^2}+|u|^2u=0 \tag{3.21}$$

The general *soliton* solutions of eqn.(3.21) at z=0 are

$$u(z=0,t)=N\eta_N sech(\eta_N t) \qquad N=1,2,3,.. \tag{3.22}$$

where η_N is a constant determined by the initial condition and N is the soliton order number. u,z,t are the normalised amplitude, distance and time respectively, being associated with the real variables by

$$u = \tau \left[\frac{\frac{2\pi}{\lambda} n_2}{|\beta_2| A_{eff}} \right]^{1/2} P^{1/2} \quad , \quad z = \frac{|\beta_2| L}{\tau^2} \quad , \quad t = \frac{t' - z/v_g}{\tau} \tag{3.23}$$

We see that the coordinate system moves at the group velocity. With the appropriate choice of η_N, the arbitrary time scale τ allows a pulse of standard duration in the dimensionless retarded-time variable t to correspond to a pulse of any desired duration in real time t'. For $\eta_N = 1$, τ is equal to (see Appendix to Ch.3 for proof):

$$\tau \approx \frac{\tau_{FWHM}}{1.76} \tag{3.24}$$

where τ_{FWHM} is the real full-width-at-half-maximum pulsewidth.

The energy of a pulse with a sech^2 intensity profile, peak power P_{peak} and FWHM pulsewidth τ_{FWHM} is

$$P_{peak} \int_{-\infty}^{\infty} sech^2 \left(\frac{1.76 t}{\tau_{FWHM}} \right) dt = \frac{2}{1.76} P_{peak} \tau_{FWHM} \tag{3.25}$$

In normalised units the pulse is written as

$$u(0,t) = A sech(\eta t) \qquad ; \qquad A \equiv \tau \left[\frac{\frac{2\pi}{\lambda} n_2}{|\beta_2| A_{eff}} \right]^{1/2} P_{peak}^{1/2} \tag{3.26}$$

with corresponding normalised pulsewidth

$$\tau = \frac{\eta \tau_{FWHM}}{2\cosh^{-1}\left(\sqrt{2}\right)} \tag{3.27}$$

and energy

$$A^2 \int_{-\infty}^{\infty} sech^2(\eta t) = \frac{2A^2}{\eta} \tag{3.28}$$

In the frequency domain, the Fourier transform of u(0,t) from eqn.(3.26) is

$$FT\{A sech(\eta t)\} = \frac{A\pi}{\eta} sech\left[\frac{\pi^2 f}{\eta}\right] \tag{3.29}$$

and the corresponding pulsewidth-bandwidth product is

$$\tau_{FWHM}\,\Delta f_{FWHM} = \frac{4\left(\cosh^{-1}\left(\sqrt{2}\right)\right)^2}{\pi^2} \approx 0.3148 \tag{3.30}$$

Only solitons of first order, or "fundamental" solitons, are discussed in this thesis and these retain a constant sech pulseshape throughout their propagation distance. At time t and distance z, the soliton solution, eqn.(3.22), with N=1 evolves as

$$u(z,t) = \eta_1 sech(\eta_1 t)\ \exp\left\{\frac{j}{2}\eta_1^2 z\right\} \tag{3.31}$$

No corresponding analytical formula for the propagation of solitons of order>2 exists. Choosing u(0,0)=1 sets $\eta_1 = 1$ and the above equation becomes

$$u(z,t) = sech(t)\ \exp\left\{j\frac{z}{2}\right\} \tag{3.32}$$

Note that the phase factor $e^{jz/2}$ applies to the whole pulse (independent of t). This is because the chirp caused by self-phase modulation is cancelled by the group velocity dispersion such that the pulse envelope propagates at a constant group velocity with zero broadening.

The periodicity of $|u(z,t)|^2$ (pulse envelope) occurs at z intervals of $\pi/2$ and is obeyed by all higher-order solitons. The distance between two successive iterations of the pulse envelope is referred to as the soliton period z_0 and although it would really seem applicable to solitons of higher order than the first, it is commonly used as a length unit when considering perturbating effects in the propagation of the fundamental soliton. The soliton period is a pulse-profile period and <u>not</u> a phase period which, for example, in the case of the fundamental soliton is 4π. Hence one phase period is equivalent to eight soliton periods. Setting $z=\pi/2$ in the second transformation of eqn.(3.23) we obtain the following expression for the soliton period

$$z_0=\frac{\pi\tau^2}{2|\beta_2|} \tag{3.33}$$

and from the first transformation, having set $|u(z,0)|^2=(\eta_1)^2=1$, we obtain an expression for the fundamental soliton peak power:

$$P_0=\frac{|\beta_2|A_{eff}}{n_2k\tau^2} \tag{3.34}$$

The normalised area S determines the number of solitons that will propagate when a pulse with normalised amplitude envelope u(0,t) is launched in an optical fiber:

$$S\equiv\int_{-\infty}^{\infty}u(0,t)dt \tag{3.35}$$

From eqn.(3.22) the area of an N^{th} order soliton is

$$S_N=\int_{-\infty}^{\infty}N\eta_N sech(\eta_N t)dt=N\pi \tag{3.36}$$

The evolution of a sech pulse is dependent on its area: In general, a soliton of order N is formed for a sech pulse of area S, $S_N-\pi/2<S<S_N+\pi/2$. More specifically, if $S=(N+\epsilon)\pi, |\epsilon|<1/2$, as in the following pulse

$$u(0,t)=(N+\varepsilon)\eta_N sech(\eta_N t) \tag{3.37}$$

then the soliton part of the pulse corresponds to an initial pulseshape of the form

$$u(0,t)=(N+2\varepsilon)\eta_N sech\left[\eta_N\left[\frac{N+2\varepsilon}{N}\right]t\right] \tag{3.38}$$

This is an N^{th} order soliton with pulsewidth $\tau'=[N/(N+2\epsilon)]\tau$ and amplitude $u'(0,0)=u(0,0)+\eta_N\epsilon$. We see that both amplitude and pulsewidth have changed: for $\epsilon>1/2$ the pulse narrows with a corresponding power increase; the opposite occurs for $\epsilon<1/2$. In both cases, however, the pulse energy decreases by $\Delta E=2\eta_N\epsilon^2$. Fig.3.9 plots τ'/τ vs u(0,0). Note the discontinuities of the curve whenever $\epsilon=\pm1/2$.

Let us now consider the particular case of $S=(1+\epsilon)\pi$. Fig.3.10 shows the evolution of the pulse's amplitude on the way to become an exact soliton. Before it settles down to a fixed value, the amplitude oscillates and the pulse loses some energy. The full solution for the asymptotic soliton in this case is

$$u(z,t)=\eta(1+2\varepsilon)\ sech[\eta(1+2\varepsilon)t]\ \exp\left\{\frac{j}{2}[\eta(1+2\varepsilon)]^2 z\right\} \tag{3.39}$$

which in the case of an initial pulse

$$u(0,t)=A\,sech(t) \qquad , \qquad A=1+\varepsilon \tag{3.40}$$

can be simplified to

$$u(z,t)=(2A-1)\ sech[(2A-1)t]\ \exp\{2j(A-1/2)^2 z\} \tag{3.41}$$

The phase factor is important; it is this phase factor that enables soliton switching in a Sagnac loop to take place, as will be shown in the next section.

It is useful to estimate the "tolerance" of the two parameters of an initial optical pulse (ie pulse duration and peak power) for it to evolve to a fundamental soliton when it is

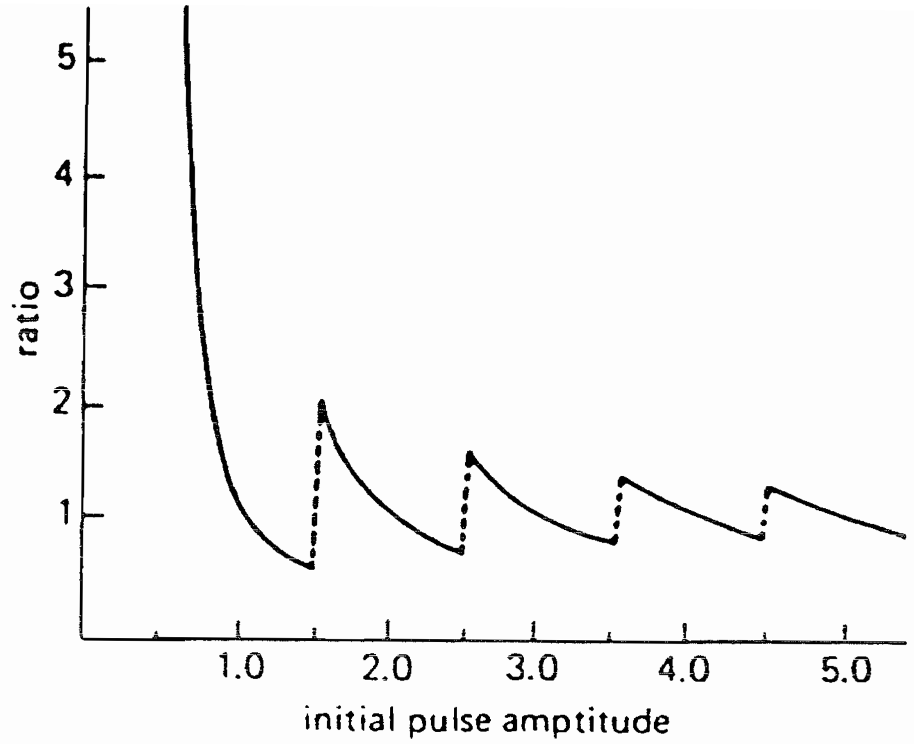

Fig.3.9 The ratio of the pulsewidths at $z=\infty$ and $z=0$ as a function of the initial pulse normalised amplitude $A=u(0,0)$. After Ref.[33].

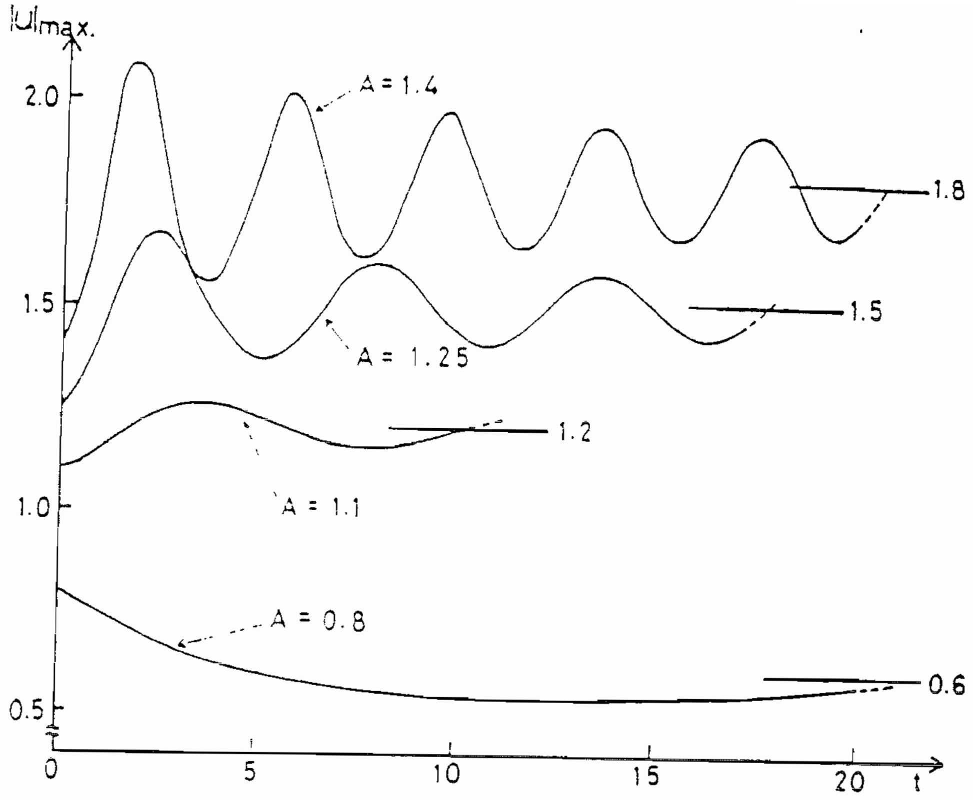

Fig.3.10 The temporal evolution of a pulse with a soliton amplitude $A=1+\epsilon$, $|\epsilon|<1$. After Ref.[34].

launched into an optical fibre of known dispersion, nonlinearity and mode area. This can only happen if $S_1-\pi/2<S<S_1+\pi/2$, which, in the case of a pulse described by eqn.(3.40), means that $0.25<A^2<2.25$. From the previous analysis this translates to

$$0.25 < \frac{P_{peak}\tau^2}{P_0\tau_0^2} < 2.25 \tag{3.42}$$

This relationship shows that a launched pulse can be between 0.25 and 2.25 times the peak power of a fundamental soliton P_0 of the same duration or, equivalently, between 0.5 and 1.5 times the pulsewidth of a fundamental soliton of the same power and still evolve to become a fundamental soliton. This demonstrates the great amount of flexibility that these wave packets exhibit when it comes to propagating as a single unit.

The incorporation of a fibre amplifier in a fibre Sagnac loop has a dramatic improvement in its nonlinear switching performance regarding the switching threshold. In view of this fact and for later discussions on solitons in fibre lasers, it is useful to outline the basic phenomena governing soliton propagation in an amplifying fibre. Experimental [15] and theoretical [16,17] results have shown that soliton propagation in optical fibre amplifiers is governed by four basic factors:

(a) The ratio of the amplifier length L_a to the soliton period z_0;
(b) The amplifier gain $G=\exp(gL_a)$;
(c) The ratio of the amplifier gain bandwidth to the soliton bandwidth;
(d) The influence of the Soliton Self-Frequency Shift (SSFS).

SSFS is a phenomenon whereby Raman effects cause a continuous downshift of the mean soliton frequency as it propagates through an optical fibre. The strength of this effect is shown to vary approximately with the inverse fourth power of the soliton pulsewidth [18]. It is therefore only significant for soliton pulses <500fs.

Of all the possible regimes of soliton propagation in amplifying fibres which are determined by the values of various parameters mentioned above, two of the most basic and common regimes arise by ignoring the effects of SSFS and amplifier bandwidth. The NLSE, eqn.(3.21) in this case is modified to

$$i\frac{\partial u}{\partial z}+\frac{1}{2}\frac{\partial^2 u}{\partial t^2}+|u|^2u-i\Gamma u=0 \qquad (3.43)$$

where

$$\Gamma\equiv\frac{z_0}{\pi L_a} \quad ; \quad L_a\equiv\frac{1}{g} \qquad (3.44)$$

and g is the amplifier gain coefficient in m^{-1}. Depending on the values of Γ and the amplifier length L_a, the two regimes can be described as follows:

(a) For $z_0 >> L_a$ and irrespective of the value of Γ the amplification can be considered as "lumped" ie the pulse exiting the amplifier is just amplified by an amount equal to the power gain of the amplifier with the rest of its other features (ie pulsewidth and optical spectrum) unchanged. This regime is called non-adiabatic.

(b) For $z_0 \leq L_a$ and $\Gamma < \Gamma_c$ where [16]

$$\Gamma_c\approx\frac{2}{\pi}(A+1)^2\ln\left[\frac{A+1}{A}\right] \qquad (3.45)$$

an input pulse A sech(t) is both progressively amplified and narrowed as it propagates through the amplifier and the regime is called adiabatic. As the pulse gets narrower and narrower, the adiabatic regime is inevitably affected by the SSFS and the amplifier gain bandwidth, and these two effects will ultimately determine the final pulseshape. The case of $\Gamma > \Gamma_c$ leads to the creation of additional binding solitons [16].

3.3.4 Sagnac Loop Soliton Switching

Now that the basic features of soliton propagation in optical fibres have been introduced, soliton switching in Sagnac loop mirrors can be discussed. Consider a Sagnac loop with a sech pulse as in eqn.(3.40) entering port #1. The pulse splits into two parts which, after traversing the loop, arrive at ports #3 and #4 to recombine. If these two parts are to retain their soliton character, the coupling coefficient α should be such that $\alpha > 0.25/A^2$ for $\alpha < 0.5$. Provided $\alpha \neq 0.5$, the two pulses will experience different phase shifts given by eqn.(3.39), so that when they arrive at ports #3 and #4 and recombine we can write

$$\begin{aligned} E_3' &= j(1-\alpha)^{1/2}\ A_2'\, sech(t/\tau_1')\ \exp\left\{2j\left[(1-\alpha)^{1/2}A-1/2\right]^2 z\right\} \\ E_4' &= \alpha^{1/2}\ A_1'\, sech(t/\tau_2')\ \exp\left\{2j\left[\alpha^{1/2}A-1/2\right]^2 z\right\} \end{aligned} \tag{3.46}$$

where

$$A_1' \equiv 2A\alpha^{1/2}-1\ ;\ \tau_1' \equiv 1/A_1' \qquad A_2' \equiv 2A(1-\alpha)^{1/2}-1\ ;\ \tau_2' \equiv 1/A_2' \tag{3.47}$$

and it was assumed that the loop is long enough for the amplitudes and pulsewidths of the two counter-propagating solitons to settle to their asymptotic values given by eqn.(3.41). The power switched to port #2 is given by

$$P_{sw}=E_2E_2^*\ ,\quad E_2=\alpha^{1/2}E_4'+j(1-\alpha)^{1/2}E_3' \tag{3.48}$$

which yields

$$\begin{aligned} P_{sw} = {} & \alpha^{1/2}A_1'^{\,2}sech^2(t/\tau_1')+(1-\alpha)^{1/2}A_2'^{\,2}sech^2(t/\tau_2') \\ & -2\alpha^{1/2}(1-\alpha)^{1/2}A_1'A_2'\,sech(t/\tau_1')sech(t/\tau_2')\cos\theta \end{aligned} \tag{3.49}$$

where

$$\theta \equiv 2z\left\{(\alpha^{1/2}A-1/2)^2-\left[(1-\alpha)^{1/2}A-1/2\right]^2\right\} \tag{3.50}$$

Integrating with respect to time gives the energy switched in normalised units

$$E_{sw}=2\left[\alpha A_1'+(1-\alpha)A_2'-\alpha^{1/2}(1-\alpha)^{1/2}A_1'A_2'\ I\ \cos\theta\right] \tag{3.51}$$

where

$$I \equiv \int_{-\infty}^{\infty} sech(t/\tau_1')\ sech(t/\tau_2')\ dt \tag{3.52}$$

If, on the other hand, the loop length is short so that pulse-shaping can be ignored, the formula for the switched energy becomes

$$E_{sw}=2A^2[1-2\alpha(1-\alpha)(1+\cos\theta)] \tag{3.53}$$

It can be seen that in both cases due to the phase uniformity of solitons, complete switching in the first-order $(0.5<A<1.5)$ regime can, in principle, be achieved when

$$\theta=2z\left\{\left(\alpha^{1/2}A-1/2\right)^2-\left[(1-\alpha)^{1/2}A-1/2\right]^2\right\}=\pm\pi \tag{3.54}$$

Fig.3.11 shows E_{sw} as a function of input energy $(=2A^2)$ as evaluated using eqn.(3.53) and as calculated by numerical integration [9] of the NLS for comparison. The agreement in the switched energy for fundamental solitons $(2A^2<4.5)$ is very good, even though pulse shape changes were ignored. This has also been demonstrated experimentally with maximum transmissions ~93% for 46pJ sech pulses [19] and ~90% for 55pJ Gaussian pulses [20].

3.4 PASSIVELY MODE-LOCKED FIBRE LASERS INCORPORATIONG FIBRE SAGNAC LOOPS

In this section two methods for passive mode-locking of fiber lasers are presented, based on the utilisation of Sagnac loop reflectors as non-linear switches. The first method, referred to as the "birefringence-biasing" method, exploits the birefringence effects mentioned in section 3.2 to bias the loop and invert its non-linear characteristic. The second arrangement, which is commonly referred to as the "Figure-of-8" arrangement, operates with the Sagnac in its unbiased, non-linear regime. The experimental results presented in each section are followed by a theoretical analysis of the mode-locked behaviour of these systems.

3.4.1 The Birefringence-Biased (B-B) Configuration

As mentioned earlier, one of the methods used in order to achieve passive mode-locking employs an intracavity element which has an intensity-dependent loss, the loss decreasing

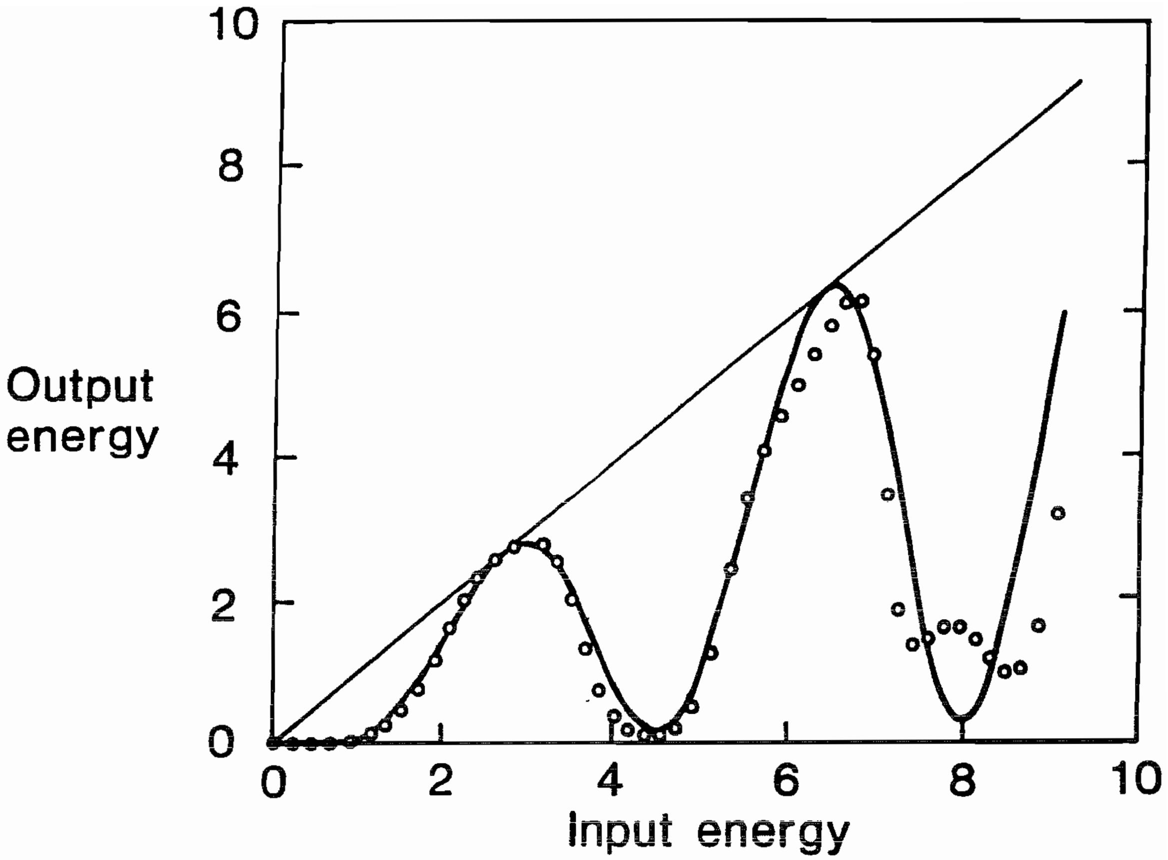

Fig.3.11 Sagnac loop transmission for soliton pulses. After Ref.[35].

with increasing intensity. Under the operating conditions of case (b) on page 48, the Sagnac loop features precisely this characteristic: in this case the Sagnac loop acts as an intensity-dependent mirror, with its reflectivity increasing with increasing intensity, until a maximum of 100% reflectivity is reached. Note, however, that there is a significant difference between the transmission characteristic of a saturable absorber and a Sagnac loop as shown in Fig.3.6: once the saturable absorber is "bleached" its transmission is constant, ie no longer intensity-dependent. Fig.3.6 on the other hand, shows that once the point of maximum transmission has been reached the transmission starts to decrease again. In this case, the "preferred" pulse (ie the one which experiences the least loss upon passing through the loop) is a rectangular pulse, ie of fixed power and arbitrary duration.

The fibre laser configuration that exploits the intensity-dependent reflectivity of a birefringent Sagnac loop in the "biased", $\Omega=90^0$, regime is called the Birefringence-Biased (B-B) configuration.

3.4.2 Experimental Details and Results on the B-B Configuration

The experimental arrangement is shown in Fig.3.12. The Sagnac loop was a 500m long length of fiber wound on a drum. Polarisation controllers were used near the coupler ports to bias it to the desired point of operation. Port #1 was spliced to ~3m of Nd^{3+} fiber with a dopant concentration of 200ppm and all fibers used were single mode at the lasing wavelength of 1.08μm. The coupler had a 50:50 splitting ratio at 1.08μm and the amplifier was pumped using a Ti:Sapphire laser at 810nm through a dichroic mirror (80% transmission of 810nm and 99% reflection of 1.1μm). The output was through port #2.

The laser had a pumping threshold of ~60mW. Passive mode-locking at the cavity round trip frequency of 440kHz was achieved spontaneously by adjusting the polarisation controllers while rotating the drum slightly. Square pulses of various durations were observed, depending on the bias conditions. Fig.3.13 shows two examples. Note that these pulse traces were obtained from the output port of the loop, ie they represent the

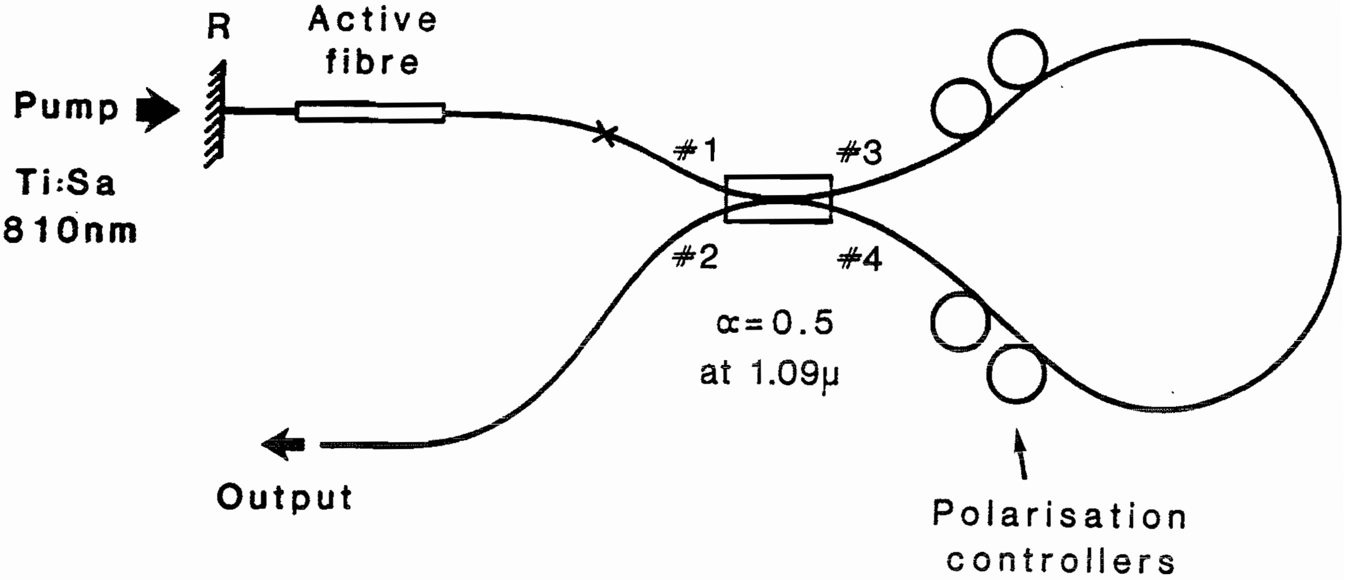

Fig.3.12 Experimental arrangement for passively mode-locked Sagnac loop laser using birefringence biasing.

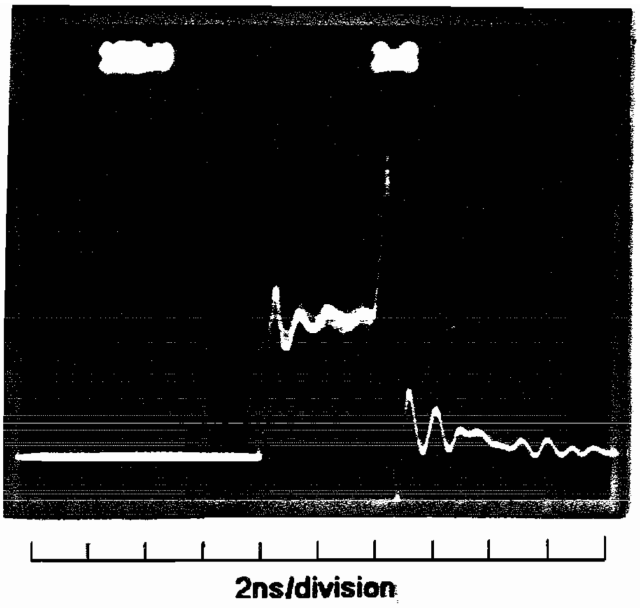

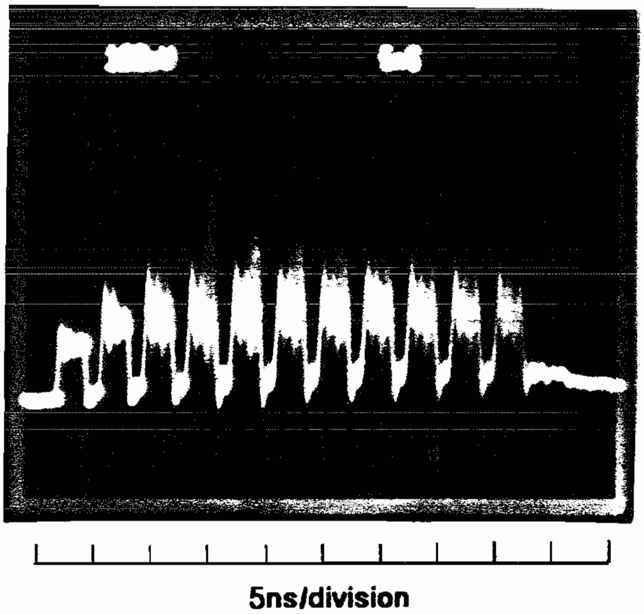

Fig.3.13 Passively mode-locked pulses obtained using the experimental arrangement of Fig.3.12.

rejected parts of the pulses that circulate in the laser cavity. When mode-locking was initiated there was a drop in the mean output power, indicating an increase in the reflectivity of the loop. Since the mode-locking mechanism depends on the correct biasing of the loop (ie $\Omega=90^0$, $\Delta\beta L=n\pi$), the laser's performance is dependent on external disturbances such as temperature, pressure etc and this explains why the mode-locked operation was not very stable. The solution to this problem would be to construct a cavity by using only polarisation maintaining fibres.

3.4.3 The Figure-of-8 (F-8) Configuration[1]

Fig.3.14 shows the Figure-of-8 (F-8) laser configuration [33,34]. At low input powers the NALM acts as a conventional loop mirror reflecting light back to the port from which it came. Thus low intensity light circulating anticlockwise in the isolator loop enters the NALM at port A and is reflected back to the same port, ie towards the isolator, where it is lost. As the intensity of light incident at port A is increased, the loop becomes nonlinear and light is switched to port B, whereupon it circulates anticlockwise in the isolator loop providing feedback to the gain medium. The system thus experiences the lowest loss for high light intensities and is therefore biased to operate in a pulsed mode. As shown in sections 3.3.2 and 3.3.4 the pulses that experience the least amount of loss are either rectangular with a peak intensity determined by the switching power of the loop, or fundamental solitons which develop a uniform phase over the entire pulse envelope as they propagate and can thus be fully switched. The low input powers required to switch a NALM operating at high gains means that pulsed operation is able to build up from noise at the NALM input. The noise is provided by reducing the linear cavity loss to a level sufficient for the onset of CW lasing. This is achieved either by applying a birefringence-induced phase bias within the NALM, or by arranging for asymetric splitting at the NALM coupler. This latter option would permit the system to be constructed entirely of polarisation maintaining fibre, thus improving the system stability [21].

---

[1] The experiments on the F-8 laser were carried out in collaboration with Dr. D. J. Richardson

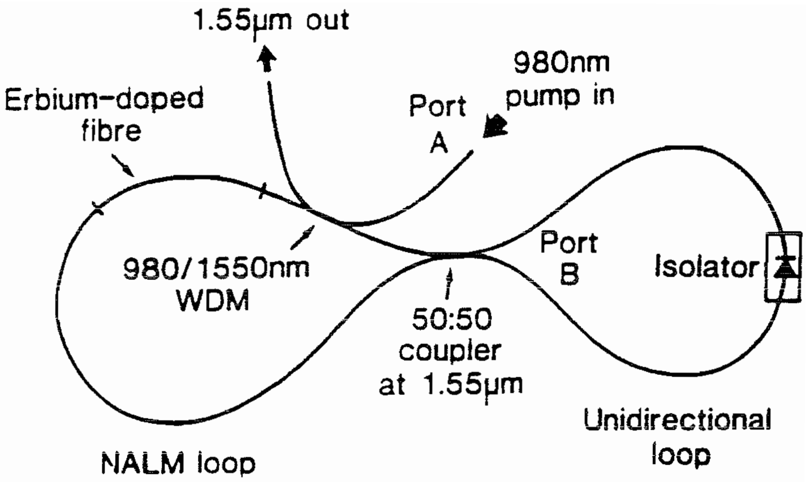

Fig.3.14 The Figure-of-eight configuration.

3.4.4. Experimental Details and Results on the Figure-8 Configuration

In our experiments the loop coupler had a 50:50 power splitting ratio at 1.55μm while a 980/1550 WDM coupler was used for pumping the erbium amplifier. Output coupling was provided by a 30:70 coupler placed in the isolator loop. The isolator was deliberately chosen to be polarisation sensitive, with an insertion loss of 0.4dB and an isolation of 40 dB. This was because polarisation insensitive isolators possess a significant amount of birefringence which obstructs the formation of ultra-short pulses. The unidirectional isolator loop had a total length of 8m, while the total NALM length was varied between 8 and 36m. The doped fibre, located asymmetrically within the NALM, was 3m long and contained 800ppm of Er^{3+}. All fibers used were single mode at 1.55μm and had a dispersion parameter of D= ~5ps/nm/km. The round trip cavity loss was estimated to be ~3dB. The pump laser was a Ti:Sapphire laser operating at 980nm. Polarisation controllers were used in both the unidirectional and Sagnac loops.

Once a certain input pump power level was reached, typically 50mW, passive mode locking was observed at the cavity round trip frequency. Once mode-locked, the input power could then be reduced well below the power required for self-starting. When mode-locked, the system lased at 1563nm, which according to the analysis in chapter 2 indicates a low-loss cavity. At low pump powers and for certain loop birefringence settings, a self-Q switch/mode-locked lasing regime was encountered. In this regime the lasing wavelength shifted to 1535nm, the wavelength shift being associated with the change in the cavity loss due to the change in the loop bias.

Both long duration (>100ps) square pulses and solitons (1-0.32ps) were observed with this system. The square pulses were generated at the cavity round-trip frequency and had an optical bandwidth of ~35nm. As mentioned previously, their rectangular shape owes its existence to the switching characteristic of the NALM, which causes the laser cavity loss to decrease progressively with pulse intensity until a certain point is reached where the loss starts to increase again. Hence, the power of the internal circulating pulse remained clamped to this value while its width must increase to accommodate a higher average circulating power. The effect is shown in Fig.3.15 where the pulse is seen to narrow as the pump power is decreased. Autocorrelation traces of these pulses showed strong evidence of substructure on a 100fs time scale.

At low pump powers (<100mW) the square pulses became less stable and the system switched to the soliton regime of operation. In general, the soliton pulses were seemingly randomly spaced within bunches, with the bunches repeating at the cavity round trip frequency. Fig.3.16 shows a example of this random pulsing. Since the detector response time is far longer than the pulse duration, the oscilloscope effectively displays the pulse energy. The pulse with twice the amplitude of the others is due to two pulses occuring within the detector response time. With appropriate adjustment of the polarisation controllers and the input pump power, harmonic mode-locking occured, Fig.3.17. Repetition rates ranging from 50MHz to 10GHz were observed within the bunches and autocorrelation was required to measure the highest repetition rates. In a practical system, the addition of a pulse multiplier such as a Fabry-Perot cavity or a recirculating delay line has been shown to stabilise the repetition rate [22]. A background-free autocorrelation of a typical soliton pulse is shown in Fig.3.18. The τ_{FWHM} of the pulses was 660fs. The corresponding optical spectrum of width 4.5nm, also shown in Fig.3.18, yields a time-bandwidth product of 0.32, which indicates bandwidth-limited mode-locked operation. Note the two side lobes located 7nm either side of the main peak. This feature is always present when the laser enters the soliton regime and becomes progressively more pronounced as the soliton duration is reduced. The effect originates from the repetitive nature of the various perturbations that the soliton is subjected to whilst circulating the fibre laser cavity [23]. As will be shown in the next section, this effect imposes a major limitation to the pulse durations that can be achieved in all fibre soliton lasers and will subsequently be refered to as "resonant loss".

3.5 THEORETICAL INVESTIGATION OF MODE-LOCKED FIBRE LASERS WITH SAGNAC LOOP MIRRORS

This section aims to provide some insight into the mode-locked systems described in the previous section. Section 3.5.1 investigates the parameters affecting the square pulse regime and section 3.5.2 discusses the soliton regime.

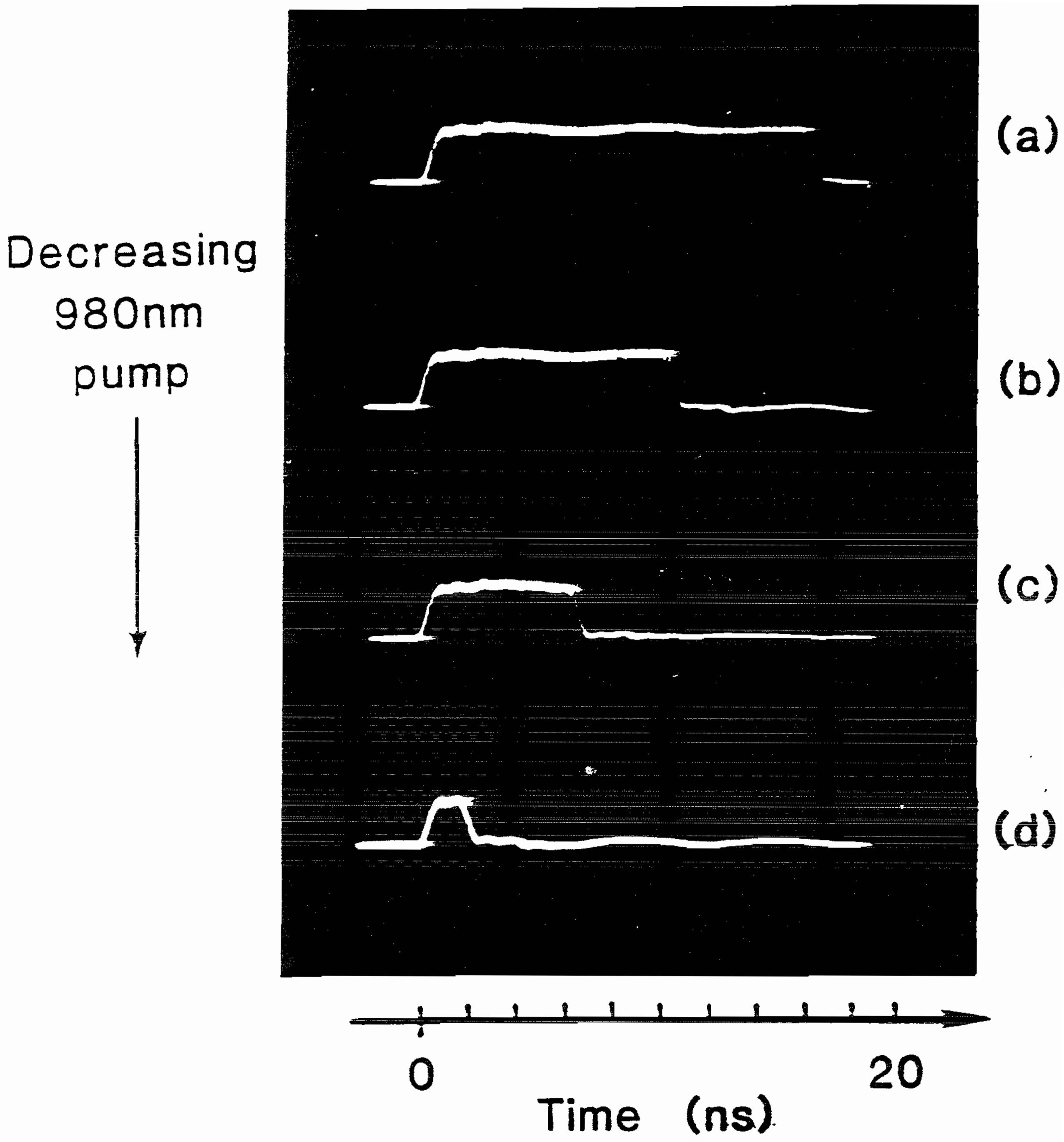

Fig.3.15 Output pulse shape of rectangular mode-locked pulses produced by the F-8 fibre laser as a function of pump power

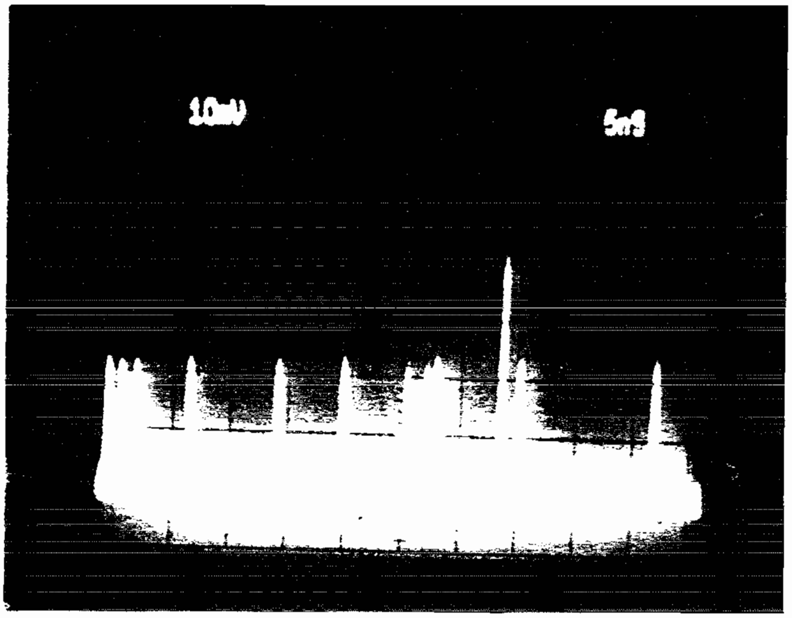

Fig.3.16 Typical internal structure of soliton pulse bunches generated at the cavity round-trip frequency. Pulse of apparently twice the amplitude of the others is due simply to two pulses occuring within a time period less than the detector response time. Soliton pulses were of 450fs duration.

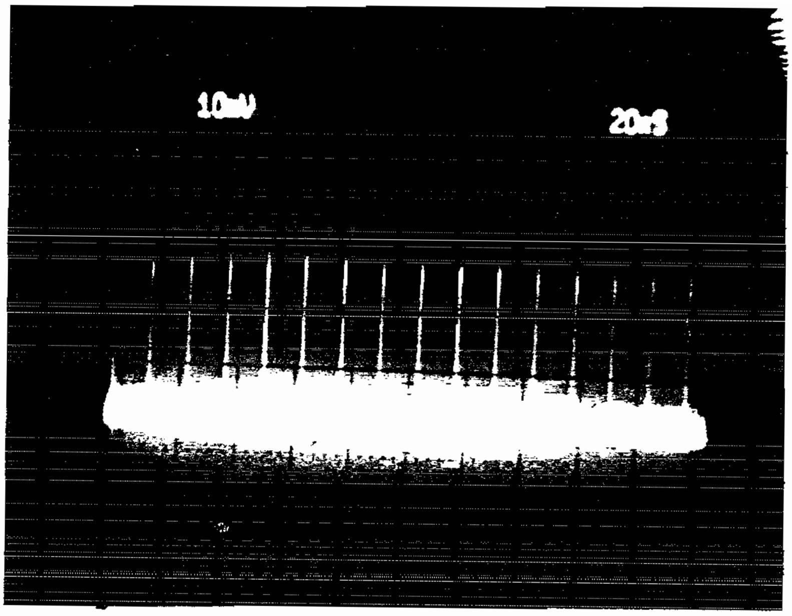

Fig.3.17 Harmonic mode-locking of F-8 fibre laser, f=67.2 MHz. Pulses have a half width of 450 ps and peak power of 40 W. 980nm pump power was 50mW

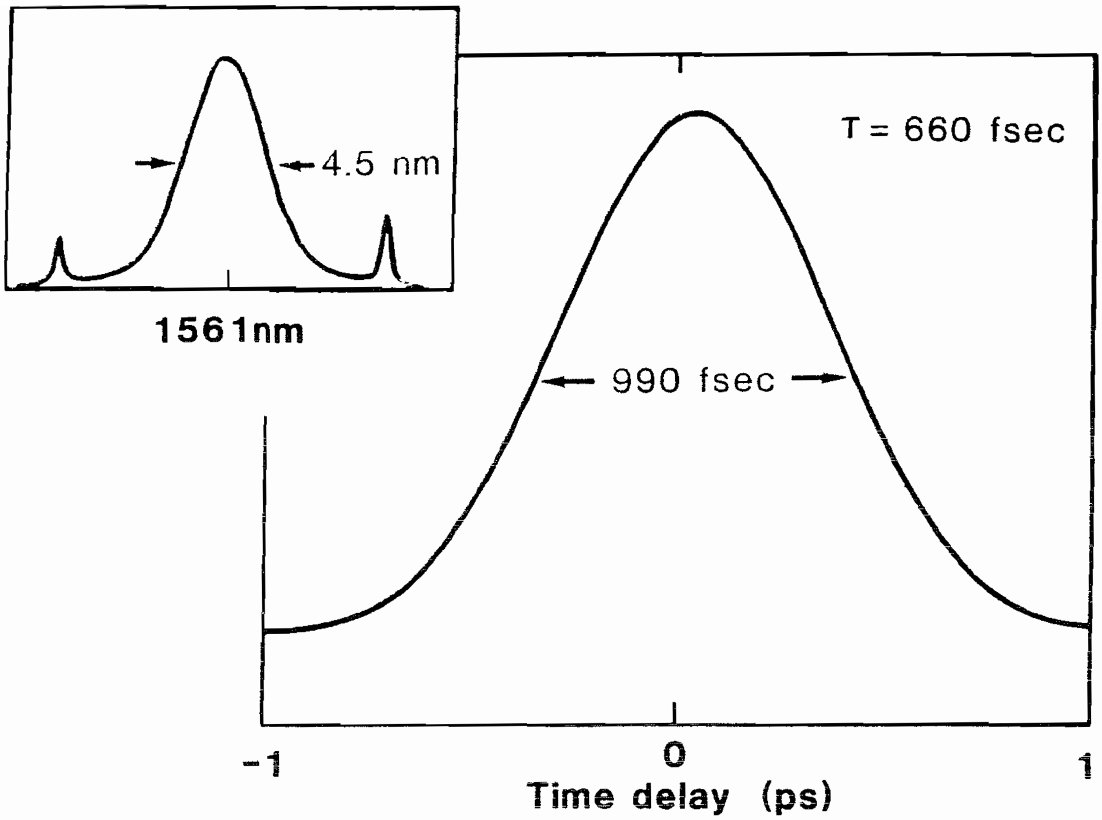

Fig.3.18 Background-free autocorrelation trace and optical spectra of 660fs soliton pulses.

3.5.1 Square pulse regime

If the gain medium is placed outside the Sagnac loop, from eqn.(3.14) the requirement for square pulse switching is

$$\Delta\beta_{NL}=\pm\pi \quad or \quad P_{sq}=\frac{\lambda A_{eff}}{2n_2|1-2\alpha|L} \tag{3.55}$$

If the gain medium is placed asymmetrically inside the loop (NALM) the case becomes more complicated due to apparently conflicting requirements regarding the gain of the active fiber: high gain improves pulse-switching and hence minimises the cavity loss, but minimising the cavity loss implies low gain. The saturated gain satisfies

$$G_s=\frac{1}{1-Loss} \tag{3.56}$$

where

$$Loss=1-R(1-T_{NL,b}^{\Omega=90^0})=1-R2\alpha(1-\alpha)(1+\cos(\theta+\pi)) \tag{3.57}$$

for the birefringence bias system and

$$Loss=1-RT_{NL}=1-R\left(1-2\alpha(1-\alpha)\{1+\cos\theta\}\right) \tag{3.58}$$

for the F-8 system. In both cases

$$\theta=\left[1-\alpha(G_s+1)\right]\beta_{NL}L \tag{3.59}$$

and R is an effective mirror reflectivity which accounts for all cavity losses except for the loss due to the loop transmission. The point of operation will be where the loss is minimised so, again, $\theta=\pi$ for both cases or

$$P_{sq}=\frac{\lambda A_{eff}}{2n_2L\left|1-\alpha\left(1+\frac{1}{R(1-(1-2\alpha)^2)}\right)\right|} \tag{3.60}$$

for the birefringence-bias case and

$$P_{sq}=\frac{\lambda A_{eff}}{2n_2L\left|1-\alpha\left(1+R^{-1}\right)\right|} \tag{3.61}$$

for the F-8 case.

3.5.2 Soliton Regime

In discussing the limitations imposed on the pulsewidth of the soliton pulses which circulate inside a passively mode-locked fibre laser cavity, the following assumptions are made:

(i) The normalised amplitude A of the pulse must satisfy

$$0.5 < A < 1.5$$

at all points inside the cavity

(ii) The gain spectrum of the fiber amplifier has an infinite bandwidth so that frequency-dependent gain and gain dispersion effects can be ignored

(iii) All pulse shaping effects can be ignored so that eqn.(3.53) can be used

(iv) The pulse is amplified non-adiabatically upon passing through the amplifier

(v) SSFS effects are not significant.

Assumption (i) ensures that no great losses occur during the round trip that may result in the break-up the soliton pulse, as discussed in section 3.3.3. Ignoring the effect of resonant loss for the time being, consider the two cases of the gain positioned either inside or outside the Sagnac loop.

With the gain medium placed outside the loop (NOLM), and using the same reasoning as in Sec.3.5.1., we may set

$$\theta=-2z\left[(1-2\alpha)A^2+\left(\alpha^{1/2}-(1-\alpha)^{1/2}\right)A\right]=\pm\pi \tag{3.62}$$

Solving for $z(=\pi L/2z_0)$ and using the formula for the soliton period (eqn.(3.33)) leads to the following expression for the soliton pulsewidth:

$$\tau=\left[\frac{2}{\pi}|\beta_2|\,\left|(1-2\alpha)A^2+\left(\alpha^{1/2}-(1-\alpha)^{1/2}\right)A\right|L\right]^{\frac{1}{2}} \tag{3.63}$$

with a corresponding peak power

$$P_{sol}=A^2P_0 \tag{3.64}$$

Note that $\tau \propto L^{1/2}$. A is the value of the soliton amplitude before it enters the Sagnac loop and, subject to the restrictions in (i) above, it can vary slightly between jumps in the number of circulating pulses: The experimental results showed that when the F-8 laser operates in the soliton regime, pump power variations do not cause pulse broadening as happens in the square-pulse regime. Instead, the number of soliton pulses that circulate inside the cavity changes in discrete steps. In a detailed study of this energy quantisation behaviour [24], however, it was found that the soliton pulse energy ($\propto A^2$) inside the loop is not precisely quantised but, depending on the number of circulating pulses, it can vary up to ~10% during successive power jumps. This is particularly noticable when there are only a few circulating pulses.

With the gain medium inside the Sagnac loop, proceeding as in Sec.3.5.2, we consider the two expressions that involve the saturated gain G_s and the angle θ:

$$G_s=\frac{1}{R\left[1-2\alpha(1-\alpha)(1+\cos\theta)\right]} \tag{3.65}$$

and

$$\theta=2z\left[\left[\left(\alpha G_s\right)^{1/2}A-\frac{1}{2}\right]^2-\left[(1-\alpha)^{1/2}-\frac{1}{2}\right]^2\right] \tag{3.66}$$

For minimum loss we require $\theta=\pi$ yielding

$$\tau=\left(\frac{2}{\pi}|\beta_2|\left|\left(\sqrt{\alpha G_s}A-\frac{1}{2}\right)^2-\left(\sqrt{1-\alpha}-\frac{1}{2}\right)^2\right|L\right)^{\frac{1}{2}} \tag{3.67}$$

Note that in both cases the non-linear refractive index n_2 and the effective area A_{eff} are not involved in the determination of the soliton pulsewidth.

3.5.3 The Effect of Resonant Loss on the Soliton Pulsewidth

In the previous section the soliton pulsewidth for a minimum loss condition was calculated with the assumptions (i)-(v) above, but without taking into account the effect of resonant loss. The actual pulsewidths observed in our experiments were longer, because resonant loss ultimately sets a limit to the soliton pulsewidth. In order to understand the impact this effect has on the performance of mode-locked soliton fibre lasers, it will be useful to outline the governing principles.

It was shown in Sec.3.3 that the fundamental soliton has a phase period equivalent to 8 soliton periods. Intuitively, one may predict that if this soliton experiences periodic perturbations of loss and gain and if the perturbation period is made equal to the soliton's phase period, its phase will systematically be distorted upon each perturbation period. Eventually this will lead to its temporal collapse. During the last two years there have been extensive experimental and theoretical studies on this effect [23,25-27,35,37] and the main conclusions that can be drawn are as follows:

(i) Any periodic perturbation on the fundamental soliton pulse leads to the gradual creation of a dispersive wave. This wave, in general, contains frequency components that are well outside the initial soliton frequency spectrum and, because the wave is dispersive, these components travel at different velocities and away from the soliton.

(ii) The frequency components of this dispersive wave that are phase matched to the perturbation period experience a linear growth in power with distance. This implies that although during one perturbation period the total gain equals the loss, the soliton gradually loses its energy to the dispersive wave. The phase matching criterion yields [23,26]

$$\Delta\nu_n = \pm\frac{1}{2\pi\tau}\left[\frac{n8z_0}{L_c}-1\right]^{\frac{1}{2}} \qquad (3.68)$$

where $\Delta\nu_n$ is the frequency separation from the soliton carrier frequency and L_c is the perturbation length. For sinusoidal gain-loss perturbation with maximum gain/loss coefficient g_{max} (in m^{-1}), the rate of energy loss per period of perturbation is (see Appendix to Chapt.3)

$$\Gamma_r = \frac{\left[\frac{z_0}{L_c}(g_{max}L_c)\right]^2 sech^2\left[\frac{\pi}{2}\left[\frac{8z_0}{L_c}-1\right]^{\frac{1}{2}}\right]}{4\left[\frac{8z_0}{L_c}-1\right]^{\frac{1}{2}}} \tag{3.69}$$

(iii) In the absence of a mode-locking mechanism, the draining of energy away from the soliton eventually leads to a gradual increase of the soliton pulsewidth τ. This, in turn, increases the soliton period so that less and less energy is lost to the dispersive wave and the soliton reaches a steady state. If a mode-locking mechanism is present, (ie a mechanism by which the round trip loss is also a function of τ), the soliton pulsewidth reaches an equilibrium value which yields the lowest combined loss. Fig.3.19 plots the soliton loss per cavity round trip against the ratio z_0/L_c separately for the NOLM and for the resonant loss as well as for the combined loss of these two. It can be seen that the resonant loss shifts the point of minimum loss of the system to higher values of z_0/L_c, and hence to higher soliton pulsewidths, compared to the point of minimum loss for the NOLM loss alone.

No analytical expression can be derived for the equilibrium position, but an approximate limiting expression based on eqn.(3.68) can be deduced by assuming that if the resonant loss per round-trip should only have a perturbative effect on the intracavity circulating soliton, it should drain away no more than a few percent of the total soliton energy. As Fig.3.20 shows, for average gain/loss modulation below ~40-50% this condition is satisfied for ratios of $z_0/L_c \geq 0.3$. Viewed from a different perspective, this is equivalent to assuming that for stable soliton propagation the first sideband should fall outside the main soliton spectrum, ie $\Delta\nu_1 \geq \Delta\nu_{FWHM}$. From eqn.(3.68) we can now obtain the

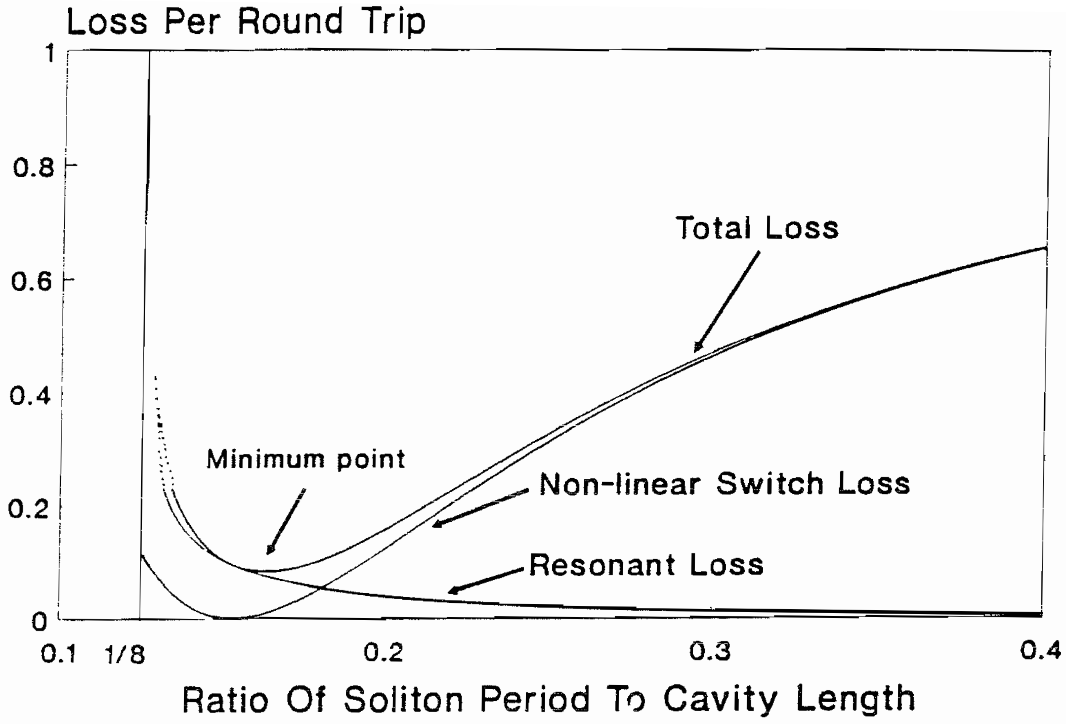

Fig.3.19 Illustration of mechanisms limiting the soliton pulsewidth: The non-linear switch loss was calculated using eqn.(3.44) with $A=1.3$ and $\alpha=0.4$. The resonant loss was calculated from eqn.(A3.13) for $g_{max}L_c=1.14$, corresponding to an average round trip gain/loss modulation of ~30%.

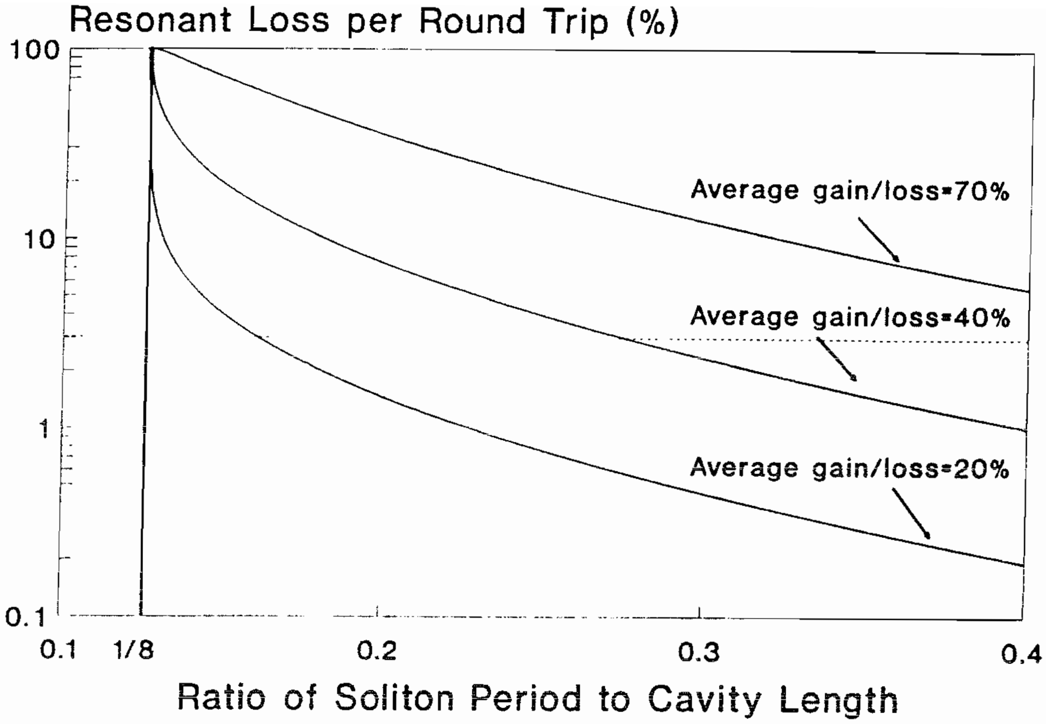

Fig.3.20 Round-trip resonant loss vs ratio of soliton period to cavity length for three different values of average gain/loss modulation. The broken line, ~~drawn arbitrarily~~ at 3%, indicates the region where the resonant loss can no longer be considered as insignificant.

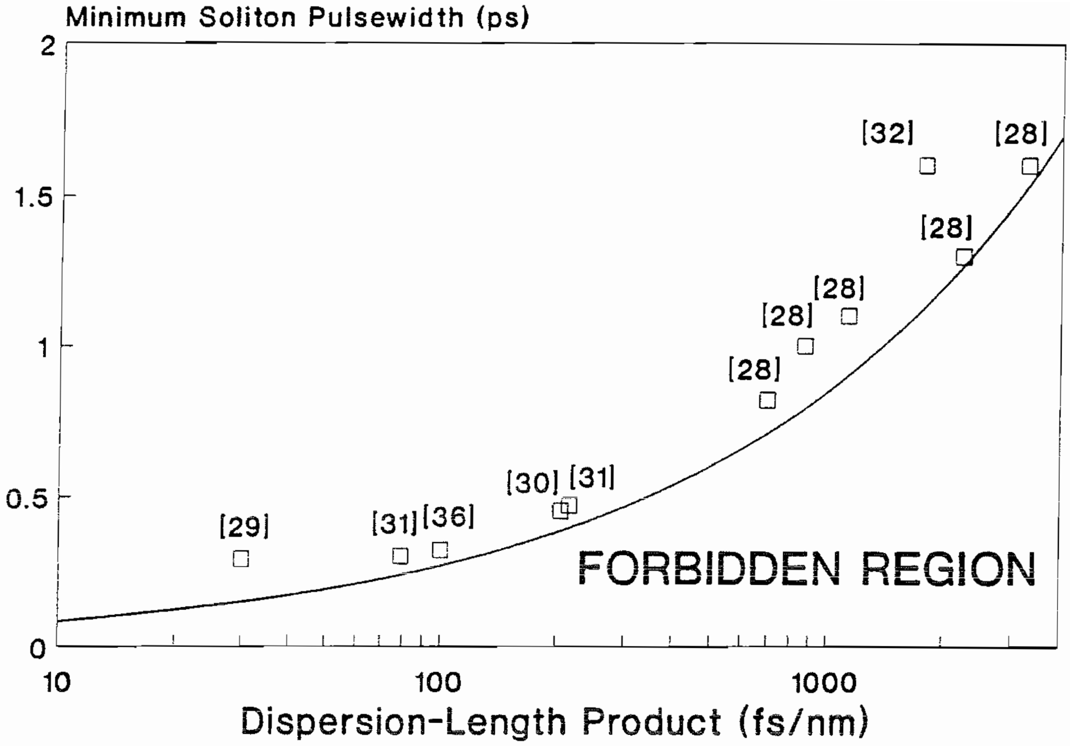

Fig.3.21 Soliton pulsewidth versus dispersion-length product (log scale). Solid line: Eqn.(3.70). The data points are taken from the references cited.

following *limiting* expression for the soliton pulsewidth τ:

$$\tau \geq \lambda \sqrt{\frac{0.09DL}{c}} \tag{3.70}$$

where $\Delta\nu_1$ is the frequency separation of the first sideband from the central frequency of the soliton, $\Delta\nu_{FWHM}$ is the full width at half maximum of the soliton spectrum, L is the length period of the perturbation ($L=L_c$ for Fig-8 and ring lasers, $L=2L_c$ for Fabry-Perot). As Fig.3.21 shows, the above expression is in good agreement with experimental results that have so far been obtained in Fig-8, ring and Fabry-Perot lasers by various research groups [28-32]. It must be emphasised that eqn.(3.70) provides a minimum estimate for the soliton pulsewidth; further restrictions on the soliton pulsewidth may be imposed by the particulars of a given system. Ultimately, for pulsewidths in the femtosecond regime, the SSFS will start to impose an extra limitation as the optical spectrum of the pulse gradually shifts outside the gain bandwidth of the amplifier.

3.6 CONCLUSIONS

The use of the non-linear optical loop mirror for passive mode-locking of fibre lasers was demonstrated and its non-linear characteristics were analysed. Two fibre laser configurations utilising non-linear optical loop mirrors were presented, namely the birefringence-bias (B-B) and the Figure-8 (F-8) system. In the normal group-velocity dispersion regime, the B-B system produced square pulses of 1-10ns duration but further experiments are needed to examine its behaviour in the anomalous dispersion regime, where solitons can be generated. Soliton behaviour was successfully demonstrated by the F-8 system, producing fundamental solitons of subpicosecond duration that earned it the status of the first all-fibre soliton laser. A theoretical analysis showed that the resonant loss mechanism, which is inherent in all soliton lasers, imposes a lower limit on the pulse durations that can be produced in soliton lasers. It was subsequently shown that in order to minimise the influence of this effect and hence achieve shorter pulsewidths, the intracavity losses should be kept as low as possible and the dispersion-length product of the cavity should be minimised.

REFERENCES

1. A. A. Godil, A. S. Hou, B. A. Auld and D. M. Bloom: "Harmonic mode-locking of a Nd:BEL laser using a 20-GHz dielectric resonator / optical modulator" *Opt. Lett.* **16** p.1765 (1991).

2. P. A. Schultz and S. R. Henion: "5-GHz mode-locking of a Nd:YLF laser" *Opt. Lett.* **16** p.1502 (1991).

3. S. J. Walker, H. Avramopoulos and T. Sizer II: "Compact mode-locked solid-state lasers at 0.5 and 1-GHz repetition rates" *Opt. Lett.* **15** p.1070 (1990).

4. M. T. Asaki, C. Huang, D. Garvey, J. Zhou, H. Kapteyn and M. Murnane: "Generation of 11-fs pulses from a self-mode-locked Ti:sapphire laser" *Opt. Lett.* **18** p.977 (1993).

5. For a good comprehensive review of the recent developments in the generation of ultrashort pulses the reader is referred to: F. Krausz et al: "Femtosecond solid-state lasers" *IEEE J. Quant. Electron.* **28** p.2097 (1992).

6. R. Jones: "A new calculus for the treatment of optical systems" *J. Opt. Soc. Am.* **31** p.488 (1941).

7. T. Birks and P. Morkel: "Jones calculus analysis of single-mode fiber Sagnac reflector" *Appl. Opt.* **27** p.3107 (1988).

8. N. Finlayson, B. K. Nayar and N. J. Doran: " Switch inversion and polarisation sensitivity of the nonlinear-optical loop mirror" *Opt. Lett.* **17** p.112 (1992).

9. N. J. Doran and D. Wood: "Nonlinear-optical loop mirror" *Opt. Lett.* **13** p.56 (1988).

10. M. E. Fermann, F. Haberl, M. Hofer and H. Hochreiter: "Nonlinear amplifying loop mirror" *Opt. Lett.* **15** p.752 (1990).

11. D. J. Richardson, R. I. Laming, D. N. Payne: "Very low threshold Sagnac switch incorporating an Erbium-doped fiber amplifier" *Electr.Lett.* **26** p.1179 (1990).

12. G. Agrawal: *Non-linear Fibre Optics* (Academic Press).

13. A. Hasegawa and F.Tappert: "Transmission of stationary nonlinear optical pulses in dispersive dielectric fibers. I. Anomalous dispersion" *Appl.Phys.Lett.* **23** p.142 (1973).

14. L. Mollenauer, R. Stolen and J. Gordon: "Experimental observation of picosecond pulse narrowing and solitons in optical fibers" *Phys.Rev.Lett.* **45** p.1095 (1980).

15. M. Nakazawa, Y. Kimura, K. Suzuki and H. Kubota: "Wavelength multiple soliton

amplification and transmission with an Er^{3+}-doped optical fibre" *J. Appl. Phys.* **66** p.2803 (1989).

16. K. Blow, N. J. Doran and D. Wood: "Generation and stabilization of short soliton pulses in the amplified nonlinear Schrodinger equation" *J. Opt. Soc. Am. B* **5** p. 381 (1988).

17. W. Hodel, J. Schutz and H. P. Weber: "Limits to the amplification efficiency of ultrashort fundamental solitons using Er-doped fibres" *Opt. Comm.* **88** p.173 (1992).

18. J. P. Gordon: "Theory of the soliton self-frequency shift" *Opt. Lett.* **11** p.662 (1986).

19. K. Blow, N. J. Doran and B. Nayar: "Experimental demonstration of optical soliton switching in an all-fiber nonlinear Sagnac interferometer" *Opt.Lett.* **14** p.754 (1989).

20. M. Islam, E. Sunderman, R. Stolen, W. Pleibel and J.Simpson: "Soliton switching in a fiber nonlinear loop mirror" *Opt.Lett.* **14** p.811 (1989).

21. D. Taverner, D. J. Richardson and D. N. Payne: "Polarisation-maintaining Figure-8 laser" *Nonlinear Guided-wave Phenomena*, Third topical meeting, paper WC3 (1993).

22. M. Nakazawa, E. Yoshida and Y. Kimura: "Repetition rate control of an LD-pumped femtosecond erbium-doped fibre laser using a sub ring cavity" in *Nonlinear Guided-wave Phenomena*, Second topical meeting, Postdeadline paper 9 (1991).

23. N. J. Smith, K. J. Blow and I. Andonovic: "Sideband generation through perturbations to the average soliton model" *J. Light. Techn.* **10** p.1329 (1992).

24. A. B. Grudinin, D. J. Richardson and D. N. Payne: "Energy quantisation in Figure-8 fibre laser" *Electron. Lett.* **28** p.67 (1992).

25. J. P. Gordon: "Dispersive perturbations of solitons of the nonlinear Schrodinger equation" *J. Opt. Soc. Am. B* **9** p.91 (1992).

26. S. M. J. Kelly: "Characteristic sideband instability of periodically amplified average soliton" *Electron. Lett.* **28** p.806 (1992). Note that the +1 in the central expression of this paper should be replaced by -1.

27. J. N. Elgin: "Perturbations of optical solitons" *Phys. Rev. A* **47** p.4331 (1993).

28. V. J. Matsas, D. J. Richardson, T. P. Newson and D. N. Payne: "Characterisation of a self-starting, passively mode-locked fibre ring laser that exploits nonlinear polarisation evolution" *Opt. Lett.* **18** p.358 (1993).

29. M. Nakazawa, E. Yoshida and Y. Kimura: "Low threshold, 290fs erbium doped fibre laser with a nonlinear amplifying loop mirror pumped by InGaAsP laser diodes"

Appl. Phys. Lett. **59** p.2073 (1991).

30. D. J. Richardson, A. B. Grudinin and D. N. Payne: "Passive, all-fibre source of 30fs pulses" *Electron. Lett.* **28** p.778 (1992).

31. I. N. Duling III: Personal communication.

32. V. J. Matsas, W. H. Loh and D. J. Richardson: "Self-starting, passively mode-locked Fabry-Perot fibre soliton laser using nonlinear polarisation evolution" *IEEE Phot. Techn. Lett.* **5** p.492 (1993).

33. D. J. Richardson, R. I. Laming, D. N. Payne, V. J. Matsas and M. W. Phillips: "Self-starting, passively mode-locked erbium fibre ring laser based on the amplifying Sagnac switch" *Electron. Lett.* **27** p.542 (1991).

34. I. N. Dulling III: "Sub picosecond all-fibre erbium laser" *Electron. Lett.* **27** p.544 (1991).

35. D. U. Noske, N. Pandit and J. R. Taylor: "Source of spectral and temporal instability in soliton fibre lasers" *Opt. Lett.* **17** p.1515 (1992).

36. D. J. Richardson, R. I. Laming, D. N. Payne, M. W. Phillips and V. J. Matsas: "320 fs soliton generation with passively mode-locked erbium fibre laser" *Electron. Lett.* **27** p.730 (1991).

37. M. L. Dennis and I. N. Duling III: "Dispersion measurement and optimisation in mode-locked fibre lasers" CLEO Proceedings, Baltimore 1993, paper CFB5.

APPENDIX TO CHAPTER 3

A.3.1 Proof of (3.14)

The soliton solution of eq.(3.11) at z=0 is

$$\begin{aligned} u(0,t) &= N\eta_N sech(\eta_N t) \\ &= N\eta_N sech\left[\eta_N \frac{t'}{\tau}\right] \end{aligned} \tag{A3.1}$$

The pulse's full-width-at-half-maximum (FWHM) should then satisfy

$$N^2\eta_N^2 sech^2\left[\eta_N \frac{\tau_{FWHM}}{2\tau}\right] = \frac{1}{2}N^2\eta_N^2 \tag{A3.2}$$

or, equivalently,

$$\cosh\left[\eta_N \frac{\tau_{FWHM}}{2\tau}\right] = \sqrt{2} \tag{A3.2$'$}$$

Hence,

$$\tau_{FWHM} = \frac{2\cosh^{-1}\left(\sqrt{2}\right)}{\eta_N}\tau \tag{A3.3}$$

For $\eta_N = 1$ we obtain

$$\tau_{FWHM} \approx 1.76\tau \tag{A3.4}$$

A.3.2 Resonant loss formula (3.60)

The expression for the energy-loss coefficient derived by Gordon [23] is

$$\Gamma_r = \frac{\left[\pi k \left|A_n\right| sech\left[\frac{\pi}{2}\Omega\right]\right]^2}{4\Omega} \tag{A3.5}$$

where

$$\Omega \equiv \sqrt{2k-1} \quad ; \quad k \equiv \frac{4z_0}{L} \tag{A3.6}$$

and $|A_n|$ is the Fourier amplitude of the n^{th} spatial harmonic component of the periodic perturbation A(z)

$$A(z) = \sum_{n=-\infty}^{\infty} A_n e^{inkz} + A_n^* e^{-inkz} \tag{A3.7}$$

Let

$$A(z) = A_{\max}\cos(kz) \tag{A3.8}$$

For this case $A_n = A_{\max}/2$. From the transformations on page 93 of Ref.[23] we have

$$\frac{dG(z)}{dz} = -\Gamma_G(z)G(z) \tag{A3.9}$$

where

$$G(z) = 1 + A(z) \tag{A3.10}$$

Note that Γ_G as defined by Gordon is minus twice the Γ as defined by eqn.(3.35) (hence the subscript G).

Substituting eq.(A3.10) into (A3.9) gives

$$\Gamma_G = \frac{A_{\max}k\sin(kz)}{1 + A_{\max}\cos(kz)} \tag{A3.11}$$

For values of $A_{\max}$ significantly less than 1, the function described by eqn.(A3.11) is approximately sinusoidal with the same period as A(z) and of maximum amplitude equal to $A_{\max}k$ (see Fig.A3.1). Hence, for a sinusoidal gain-loss of maximum normalised amplitude $\Gamma_{\max} = g_{\max} z_0/\pi$ (with Γ as defined by eqn.(3.35)), the corresponding $|A_n|$ is

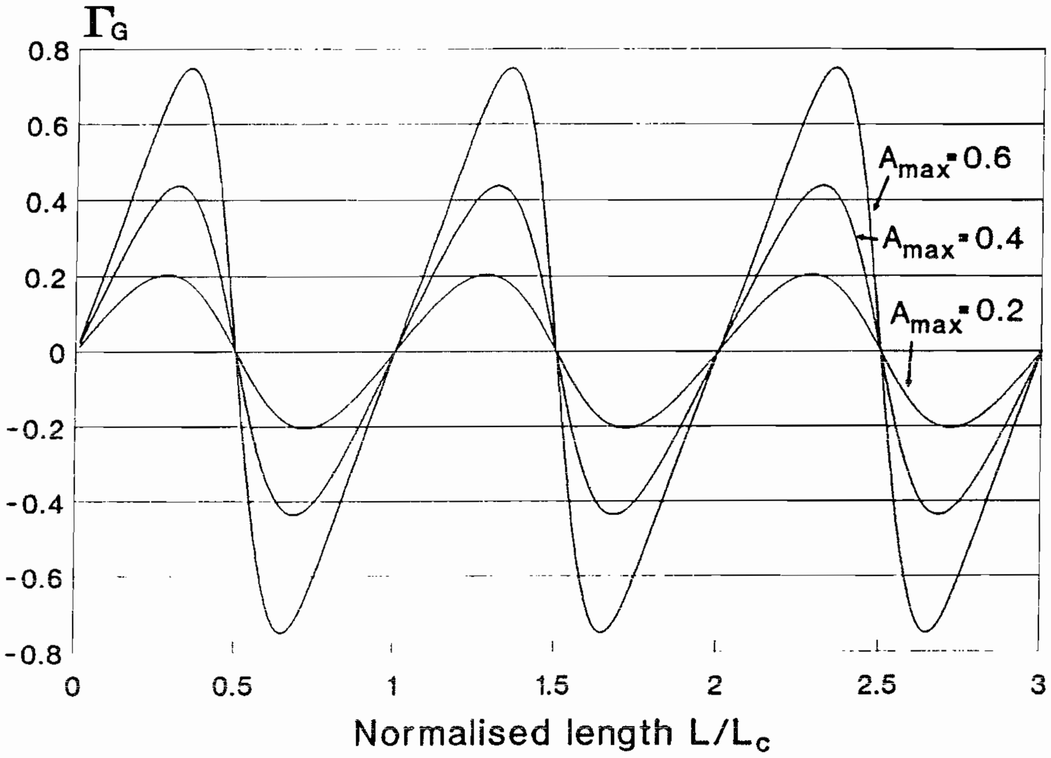

Fig.A.3.1 Γ_G vs kz (Eqn.(A3.11) for different values of A_{max}. k (Eqn.(A3.6)) was set equal to 1.

$$|A_n| \approx \frac{g_{\max} L_c}{4\pi} \tag{A3.12}$$

and the energy lost to the dispersive wave per round trip (=perturbation period) is then

$$1-e^{-\Gamma_r z}=1-e^{-\Gamma_r \frac{\pi}{2}\frac{L}{z_0}} \tag{A3.13}$$

Note that the average gain-loss over a half-period is

$$\langle G\rangle = e^{\frac{g_{\max} L_c}{\pi}} \tag{A3.14}$$

CHAPTER 4

PASSIVE MODE-LOCKING OF FIBRE LASERS II: SYSTEMS BASED ON NON-LINEAR POLARISATION EVOLUTION

4.1 INTRODUCTION

Following the successful use of the Sagnac loop as a non-linear switch for passive mode-locking of fibre lasers, this chapter introduces a second type of non-linear switch that has been proved to be equally successful. Its operation is based on the fact that the polarisation evolution of light as it propagates through a birefringent medium is intensity-dependent. This effect has been given the general name "Non-Linear Polarisation Evolution" (NLPE), but it has also been referred to as "Non-Linear Polarisation Rotation". The origins of the NLPE technique for passive mode-locking of solid-state lasers date back as far as 1972 [1] but more extensive studies were performed five years later by K. Sala [2]. Although Sala's experiments on a Nd:glass Fabry-Perot system were quite successful (achieving self-starting mode-locked operation) the NLPE technique was not adopted by any other group until 1991 when M. Hofer et al. [3] demonstrated self-sustaining passive mode-locked operation of a Nd^{3+}-doped fibre laser in a Fabry-Perot configuration.

This chapter will introduce the fundamental principles behind NLPE and will present for the first time experimental results which demonstrate how NLPE can be used to produce self-starting passively mode-locked operation in Er^{3+}-doped ring or Fabry-Perot fibre lasers. The experiments show that, as with the Figure-8 fibre laser configuration, the pulse type generated with the NLPE fibre laser schemes is the fundamental optical soliton.

4.2 REVIEW OF THE THEORY OF NON-LINEAR POLARISATION EVOLUTION OF LIGHT IN BIREFRINGENT MEDIA

In 1964 P. D. Maker, R. W. Terhune and C. M. Savage [4] showed that the intensity-dependent refractive index due to the third-order non-linear susceptibility χ^3 leads to self-induced changes in the polarisation state of an intense light beam propagating through an isotropic non-linear medium. Many years later, H. G. Winful [5,6], motivated by previous encouraging experimental results which demonstrated the feasibility of all-optical logic gates and intensity discriminators using birefringent optical fibres [7,8], presented a full solution to the problem and showed its association with the existence of a polarisation instability.

The non-linear polarisation evolution of light in a birefringent medium can be visualised to be the result of a self-induced change in the fibre's birefringence: Consider a birefringent medium with birefringent axes f (fast) and s (slow) and corresponding refractive indices n_f and n_s ($n_f < n_s$, see Fig.4.1). If a light beam of intensity I propagates along the fast axis of the birefringent medium then the refractive indices of the two axes for light of the same wavelength are given by

$$\begin{aligned} n_s' &= n_s + \frac{1}{3} n_2 I \\ n_f' &= n_f + n_2 I \end{aligned} \qquad (4.1)$$

Similarly, if the light beam is oriented along the slow axis, the new refractive indices n'_f, n'_s will be

$$\begin{aligned} n_s' &= n_s + n_2 I \\ n_f' &= n_f + \frac{1}{3} n_2 I \end{aligned} \qquad (4.2)$$

Equivalently, one may interpret this as a change in the beat length L_b. Figs.4.2, taken from Ref.[6], show a phase plane representation of the evolution of the state of polarisation of light in a birefringent fibre at (a) low and (b) high input powers. Starting

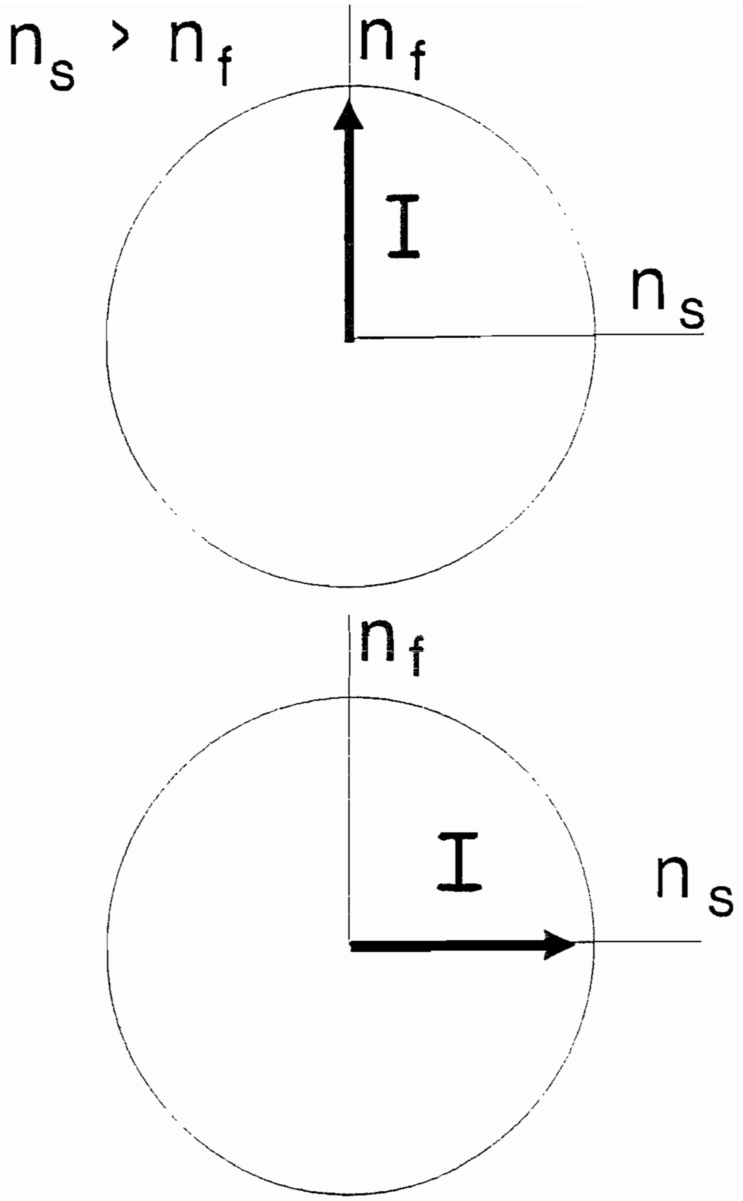

Fig. 4.1 Non-linear refractive index change in birefringent media.

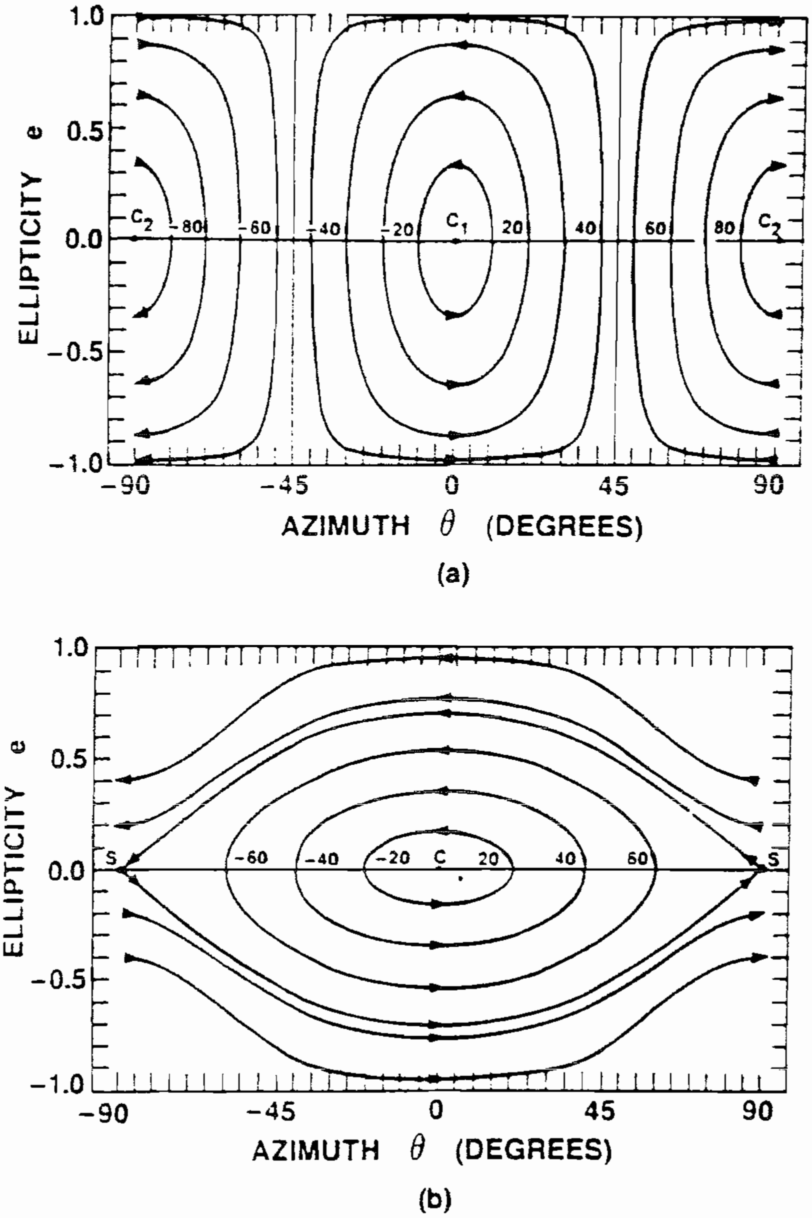

Fig.4.2 Phase-plane trajectories of the polarisation state (a) Low input power ($p << 1$). (b) High input power ($p=1$) Points labeled S are unstable saddle points. (After Ref.[6])

from an arbitrary input polarisation state, the polarisation evolves with distance along a trajectory indicated by the arrows in Figs.4.2(a,b) and all orbits close after a distance equal to the beat length. Closed orbits represent oscillatory motion with input orientations of less than 45^0 from the slow axis leading to oscillatory motion about that axis, whereas larger angles result in oscillations about the fast axis. Figs.4.2(a,b) show that although at low input powers both axes, points C_1,C_2, are stable oscillation points, at high input powers only the slow axis, point C, is still a stable point of oscillation whereas oscillation along the fast axis, point S, has become unstable. Introducing a normalised input power p given by

$$p \equiv \frac{n_2 I}{\frac{3}{2}\Delta n} \tag{4.3}$$

the instability occurs for p values close to unity. This is because for p=1, light directed at the fast axis has exactly the amount of input intensity required to make n'_f and n'_s equal, ie to cancel the intrinsic birefringence Δn of the medium.

Solving the differential equations for the NLPE of light in birefringent fibres involves the use of elliptic functions but for some particular cases approximate solutions have been derived [9]. The exact solution of the optical fibre's beat length variation L_b with input power p is given by

$$\frac{L_b}{L_{b_0}} = \frac{2K(m)}{\pi\left[1+p^2-2p\cos(2\theta)\right]^{1/4}} \tag{4.4}$$

where L_{b0} is the fibre's natural beat length as given in p.45, K(m) is the quarter period of the Jacobian elliptic function cn(x/m) and θ is the azimuth angle of the polarised light with respect to the fast axis. For linearly polarised light at $\theta=45^0$, the approximate expression for L_b is given by

$$\frac{L_b}{L_{b_0}} = \left[\frac{3}{8}+\frac{5}{8}\sqrt{1+p^2}\right]^{-1/2} \tag{4.5}$$

Thus, by placing a polariser at the end of a birefringent fibre carrying light of variable intensity, a non-linear transmission characteristic is obtained; this is the principle behind the passively mode-locked operation of fibre lasers which use NLPE.

4.3 NON-LINEAR POLARISATION EVOLUTION IN A FIBRE RING LASER CONFIGURATION

This section studies the effects of NLPE in a fibre ring laser arrangement. The theoretical section 4.3.1 shows that these effects are best observed when low birefringent fibres are used and discusses the variation of the switching power with the fibre beat length number. Dispersion effects have been initially neglected for simplicity but this case will be covered later in the chapter. The experimental results that are subsequently presented provide a full characterisation of the NLPE ring laser configuration in which the various mode-locking regimes are discussed and the mode-locked performance associated with various cavity parameters is investigated.

4.3.1 Theory

Consider a ring laser cavity which includes a birefringent element [L], a polariser [P] and a rotating element [Ω] as shown in Fig.4.3. Starting from point A and representing [L], [P] and [Ω] with their Jones matrices we can write the following eigenvalue equation for the components of the electric field circulating inside the cavity:

$$[P]\,[\Omega]\,[L]\begin{bmatrix} E_f \\ E_s \end{bmatrix} = \lambda \begin{bmatrix} E_f \\ E_s \end{bmatrix} \qquad (4.6)$$

where the subscripts f and s denote that the electric field has been resolved with respect to the fast and slow axes of the birefringent element. By using a right-handed coordinate system of axes, the matrices [P], [L] and [Ω] take the form

$$[P] \equiv \begin{bmatrix} \cos^2\theta & \sin\theta\cos\theta \\ \sin\theta\cos\theta & \sin^2\theta \end{bmatrix} \qquad (4.7)$$

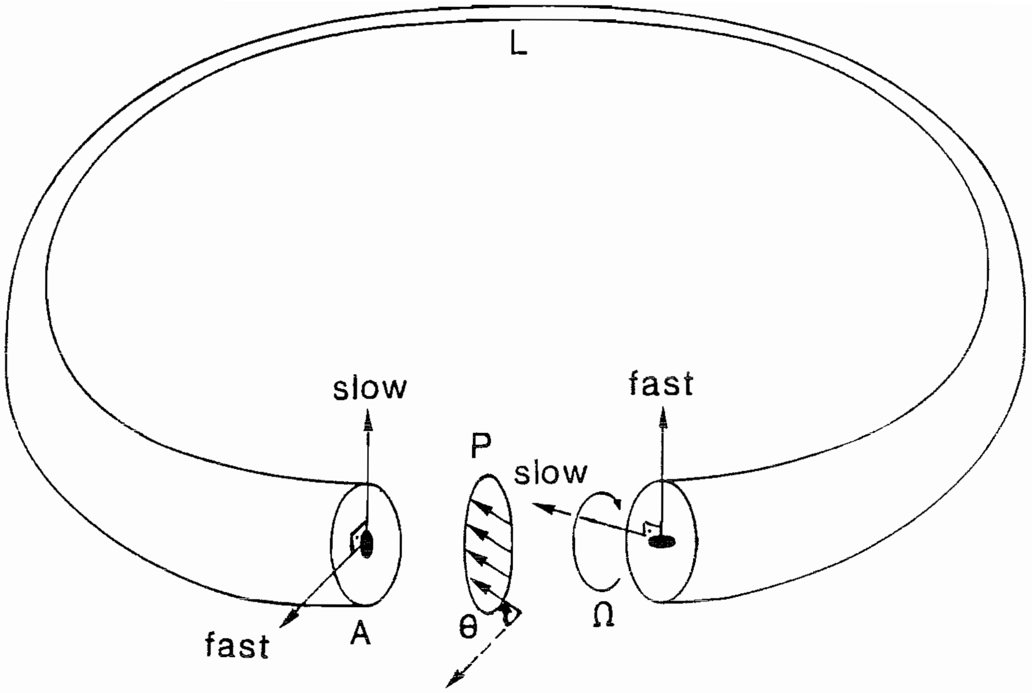

Fig.4.3 Conceptual fibre ring laser cavity schematic.

$$[L] \equiv \begin{bmatrix} e^{j\beta_x L} & 0 \\ 0 & e^{j\beta_y L} \end{bmatrix} \tag{4.8}$$

$$[\Omega] \equiv \begin{bmatrix} \cos\Omega & -\sin\Omega \\ \sin\Omega & \cos\Omega \end{bmatrix} \tag{4.9}$$

The eigenvalues λ that obey eqn.(4.6) are the following:

$$\lambda_1=0, \qquad \lambda_2=e^{i\beta_f L}\cos(\theta-\Omega)\cos\theta+e^{i\beta_s L}\sin(\theta-\Omega)\sin\theta \tag{4.10}$$

where β_f, β_s are the two propagation constants along the axes of the birefringent element of length L, θ is the azimuth angle of the polariser with respect to the fast axis and Ω is the rotation angle. Note that the system possesses only one polarisation eigenmode because one of the eigenvalues is zero. The magnitude of the second eigenvalue gives the round trip intensity transmission T of the system:

$$T \equiv |\lambda_2|^2=\cos^2\Omega-\frac{1}{2}\sin(2\theta)\sin(2(\theta-\Omega))\left[1-\cos\left[2\pi\frac{L}{L_{b_0}}\right]\right] \tag{4.11}$$

where L_{b0} is the natural (linear) beat length of the birefringent element. Three cases are of particular interest:

(a) If cos (2π L/L_{b0})=1, ie the ring is made up of an integer number of beat lengths at the wavelength of operation, then the round trip transmission is equal to $\cos^2\Omega$, ie independent of the orientation of the polariser θ.

(b) If cos (2π L/L_{b0})=-1, ie the ring is made up of a half integer number of beat lengths at the wavelength of operation, and $\Omega=0$ then the transmission becomes equal to 1-$\sin^2(2\theta)$.

(c) If $\theta=0$ then the transmission becomes wavelength independent.

The beat length variation with input power ultimately then results in an intensity dependent cavity transmission T(p). Fig.4.4 shows the numerically evaluated cavity transmission T(p) for $\theta=45^0$, 30^0 and 20^0 with $L/L_{b0}=1$ and $\Omega=90^0$, so that T(0)=0 at the wavelength of operation. Note that T(p) reaches a maximum value of 1 around p=2.5 and then starts falling again, a behaviour similar to that observed from the non-linear optical loop mirror, see Fig.3.6.

Provided that Ω is set such that the cavity loss is maximised for low powers (T(0)=0) at a particular wavelength and θ is set equal to 45^0 (for maximum switching efficiency), we can use the approximate expression eqn.(4.5) and write the following equation for the "switching" power, ie the power required for T(p) to reach its first maximum:

$$\left[\frac{3}{8}+\frac{5}{8}\sqrt{1+p^2}\right]^{-1/2}=\frac{2}{2+L_{b_0}/L} \tag{4.12}$$

which has the solution

$$p_{sw}=\sqrt{\frac{1}{25}\left[2\left[2+\frac{L_{b_0}}{L}\right]^2-3\right]^2-1} \tag{4.13}$$

Fig.4.5 displays how the switching power p_{sw} depends on the number of beat lengths L/L_{b0} in the cavity. Notice that the p_{sw} has fallen drastically after 20 beat lengths, hence the advantage of working in the multi-beatlength regime. In terms of real power units, eqn.(4.3) in conjunction with eqn.(4.13) indicate that for the same number of beat lengths the use of low birefringent fibre provides an additional reduction in the optical power required in order to observe the non-linear polarisation effects. In the experiments described below, 10-200m of low birefringence spun fibre were used to form a part of a ring or a Fabry-Perot fibre laser cavity. This enabled non-linear polarisation switching to take place at input pump powers as low as 80mW.

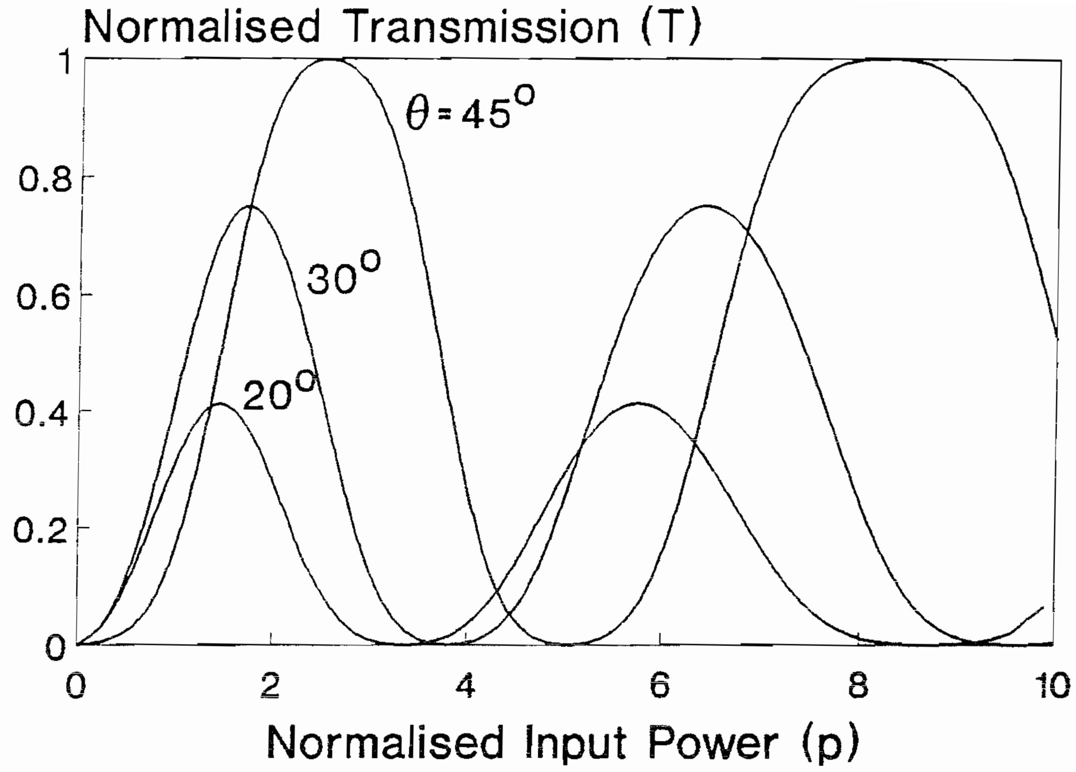

Fig.4.4 Cavity transmission T vs normalised input power p for linearly polarised light at $\theta=45$, 30 and 20 degrees to the fast axis and $\Omega=90^0$.

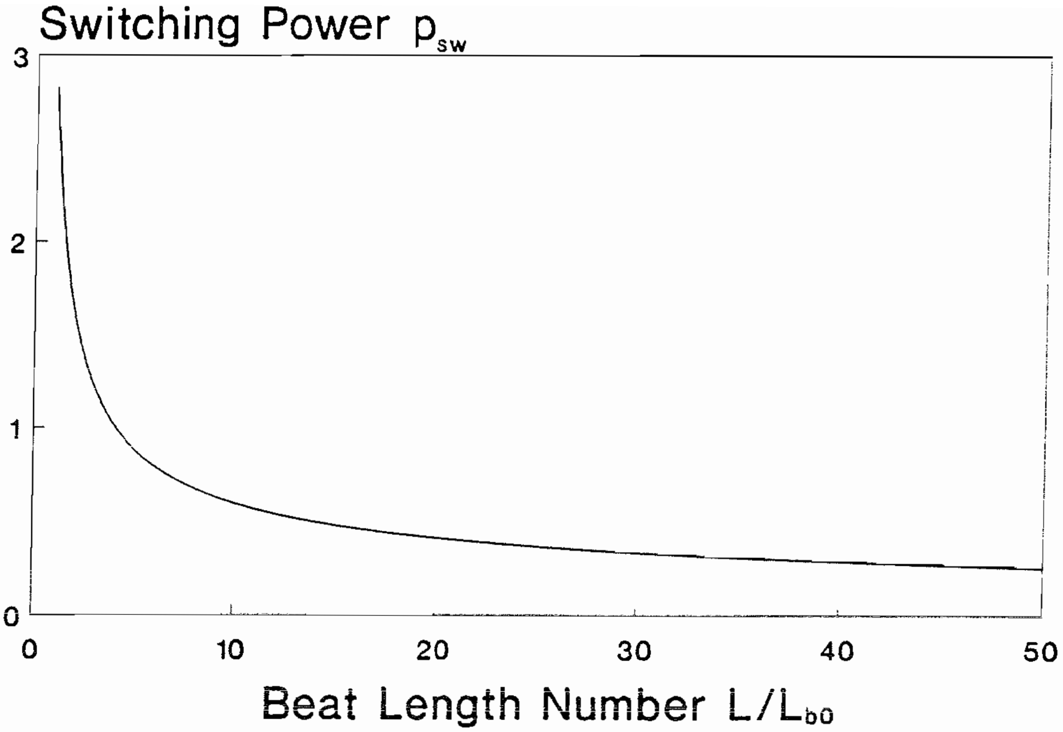

Fig.4.5 Normalised switching power p_{sw} vs Beat length number (Equation (4.13)).

4.3.2 Experimental Details and Results

Initially, the experimental configuration shown in Fig.4.6 was used. The pump source was an argon-ion pumped Ti:Sapphire laser providing up to 3W of cw light at 980nm to pump the EDFL through a wavelength division multiplexing (WDM) coupler. The remaining output port of the WDM served for monitoring the launched pump power. The cavity comprised of 4m of erbium-doped fibre, 180m of passive, low birefringence spun fibre, a fibre pigtailed polariser (FP), both supplied by York Fibres Ltd, a pigtailed polarisation-insensitive optical isolator (OI) from BT&D Technology and two sets of polarisation controllers (PC's) one placed before the FP and one before the OI. These served as the means to control Ω and θ and thus control the total loss of the system. Output coupling was provided by a 90:10 coupler as shown. The active fibre had an erbium dopant concentration of 800ppm, NA=0.15 and a cutoff wavelength of λ_c=960nm. The passive fibre was characterised by an NA of 0.1, a cutoff wavelength of λ_c=1250nm, a group velocity dispersion parameter of D=17ps/nmkm @ 1.56μm, an effective core area of 124μm^2 and an estimated beat length >10m @ 1.56μm.

For a certain setting of the PCs, the laser exhibited a CW threshold of 25mW launched pump power; because of the presence of a polariser in the ring, the orientation of the PCs controls the total loss of the system. In this way, the output power of the laser could be reduced to as low as 3% of its full power (minimum loss) value, i.e. an extinction ratio of 15 dB. When set in this high-loss condition, the laser is encouraged to operate in a pulse mode by the fact that high-intensity pulses cause the onset of nonlinear birefringence and a concomitant swing in the polarisation state reaching the polariser, thereby reducing the resonator loss. After appropriate adjustment of the PC's, self-starting mode-locking could be initiated by increasing the launched pump power to a "second" threshold value of 80mW. Figs.4.7(a,b) show the CW and mode-locked optical spectra respectively. When running CW, the optical spectrum of the laser exhibited a number of equally spaced peaks. This is a consequence of eqn.(4.11) which indicates a wavelength-dependent cavity loss with period $\Delta\lambda=\lambda L_{b0}/L$. It is believed that the isolator leads, which are made of polarisation maintaining fibre, were the dominant source of birefringence in our cavity and provided the 1nm peak spacing in the optical spectrum.

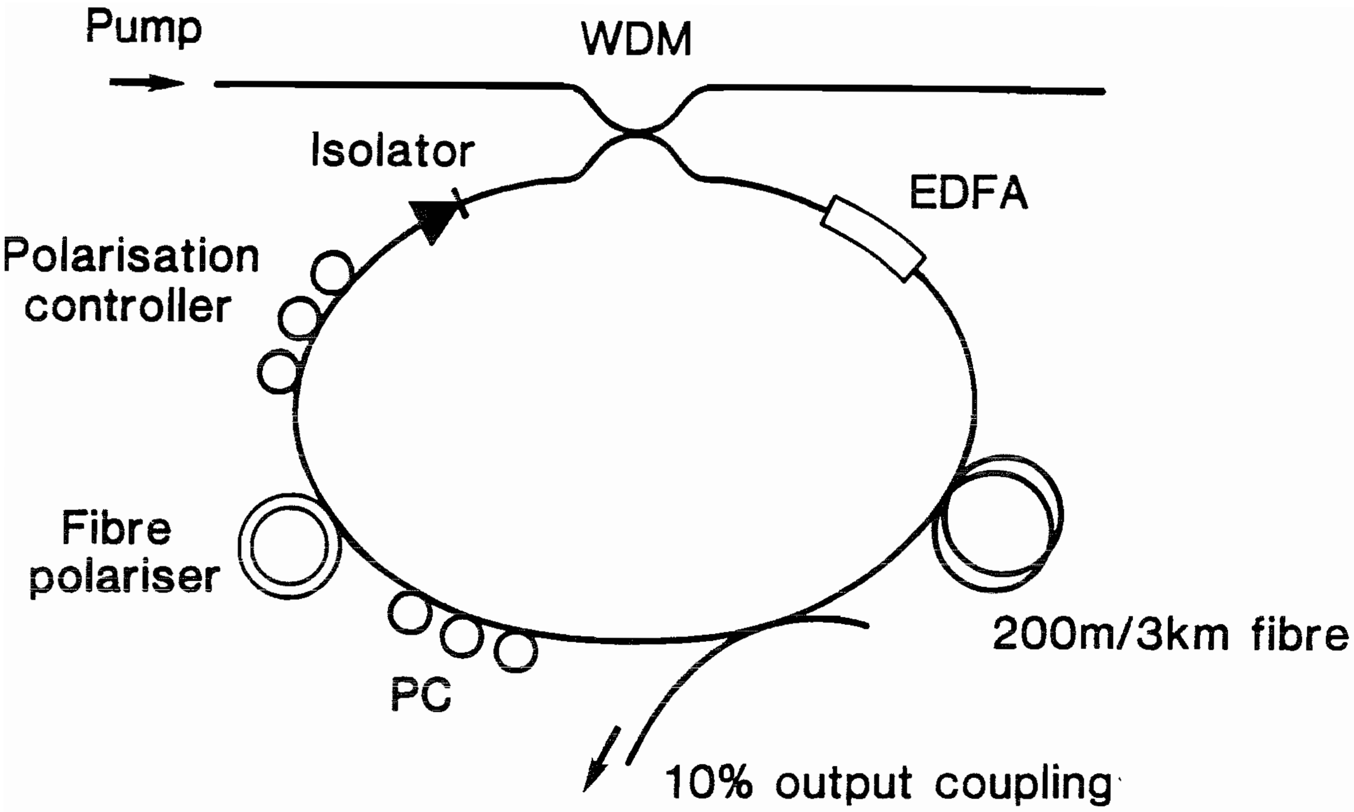

Fig.4.6 Experimental configuration of a fibre ring laser corresponding to the cavity schematic of Fig.4.3

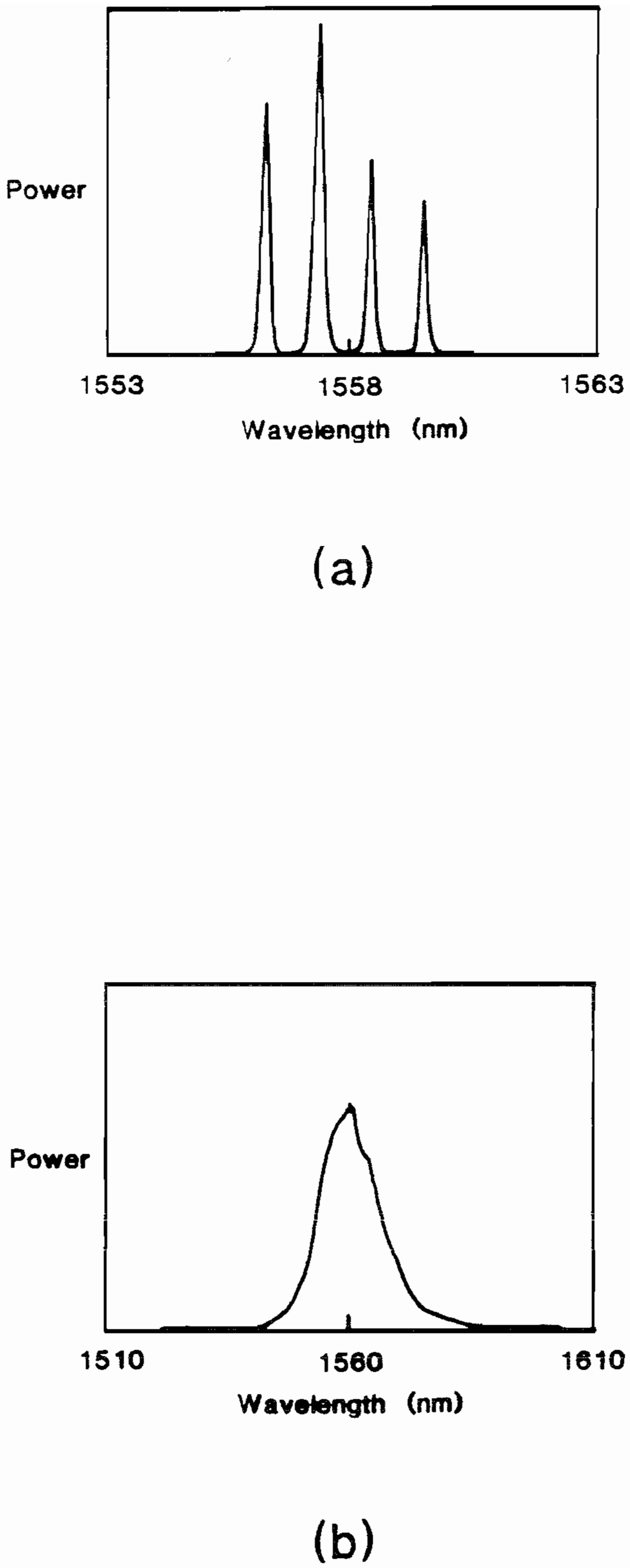

Fig.4.7 (a) CW and (b) mode-locked spectra of the 200m fibre ring laser

When the laser was mode-locked, the peaks disappeared and a broad (>10nm) lasing linewidth resulted. With intracavity pulse powers in the region of 40W, there was no evidence in the optical spectrum of self-modulational instability [10] or stimulated Raman scattering. Fig.4.8 shows the dependance of the pulsewidth on pump power for a particular arrangement of the PC's. The pump power values, in descending order, are 850, 450 and 250mW, leading to pulse durations of 7, 4 and 2 ns respectively as shown. The square pulse shape is indicative of a switching level similar to that observed in the mode-locked Sagnac loop lasers discussed in Chapter 3. This is because of the similarity between the transmission characteristics of the NLPE-based non-linear switch and those of the NALM / NOLM. By careful adjustment of the PC's with the pump power kept at a fixed level, this switching level, and hence the intracavity pulse power, could be made to vary between 20-40 W with an associated variation in pulsewidth of 4-2ns respectively. Mode-locking could be sustained at a minimum launched power of 79mW, indicating minimal hysterisis in the mode-locking behaviour.

Replacing the 180m of low-bi fibre with 3km of standard telecommunications fibre (λ_c=1201nm, NA=0.11, D=18ps/nmkm @ 1.55μm) resulted in a less stable mode-locked behaviour. The mode-locking threshold, pulse repetition rate, shape, duration and optical spectrum were all very sensitive to the setting of the PC's. The laser could either operate at the fundamental, as seen in Fig.4.9(a), or higher harmonics of the fundamental round trip frequency. The pulse duration varied between 300ns for the fundamental repetition rate and 0.75ns at the highest repetition rate observed. Pulse bunching and pulse break-up effects were also observed as seen in Figs.4.9(b,c), indicating a departure from the pure mode-locked behaviour. Typical values for the cw lasing and mode-locking thresholds, which, as with the 200m fibre, were dependent on the PC's orientation, were 32mW and 700mW of launched pump power respectively, but, once mode-locked, the pulses could be sustained at a much lower pump level (80mW). This hysterisis effect was not observed in the experiments with the 200m fibre. For launched pump powers greater than 750mW we observed broad (150nm) laser oscillation, with the harmonically mode-locked laser producing pulses of 2ns duration at a repetition rate of 2.2MHz, which was the 33rd harmonic of the cavity (see Figs.4.10 and 4.11). The pulse power was 6.8W which is above the threshold power for stimulated Raman scattering for our fibre which

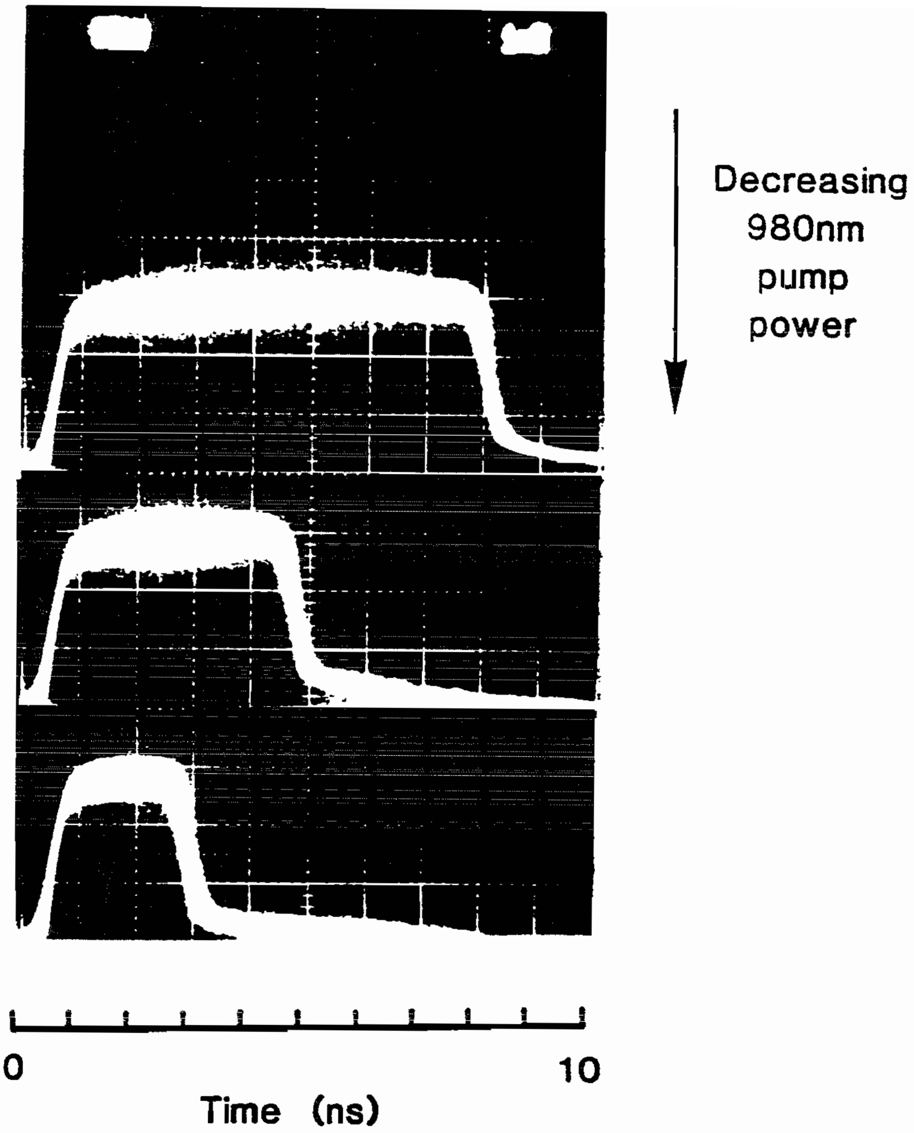

Fig.4.8 Pulsewidth dependence on pump power of the 200m mode-locked fibre ring laser.

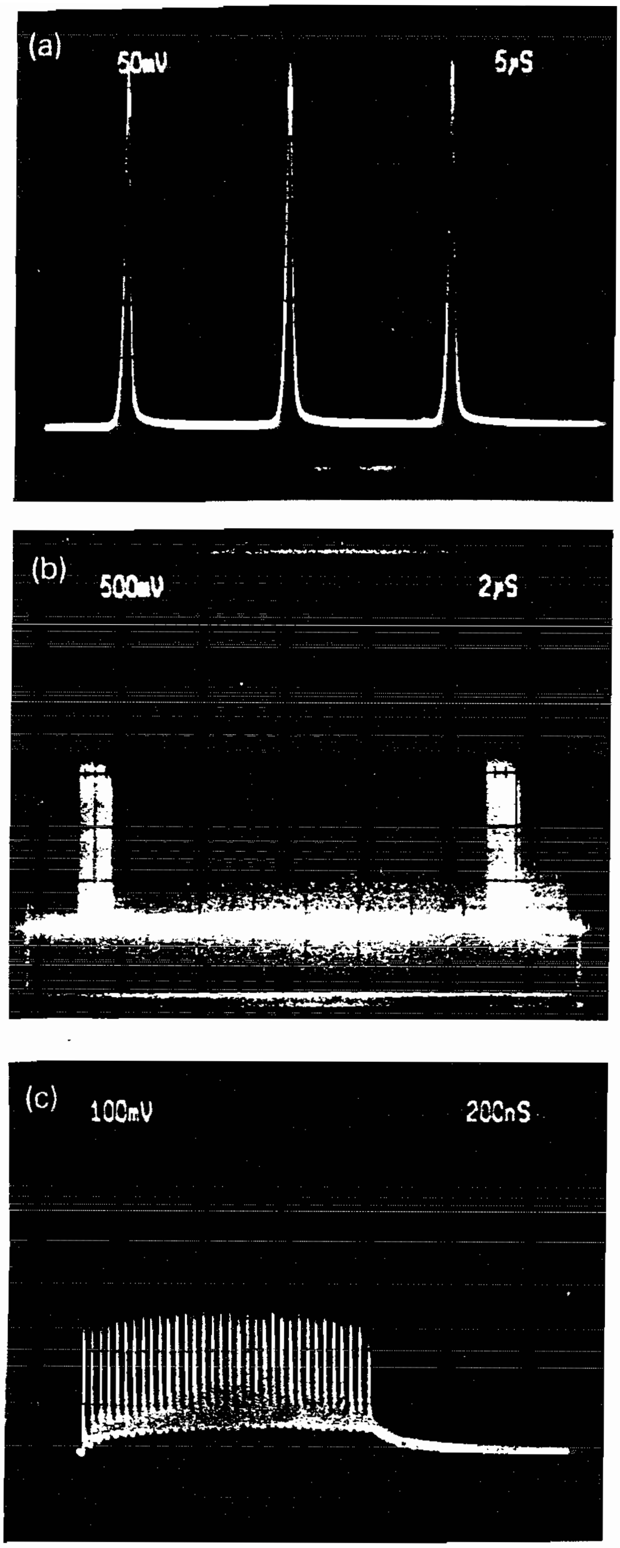

Fig.4.9 3km fibre ring laser: (a) Fundamental mode-locking (b) Pulse bunches circulating around cavity at the round trip frequency (c) Exploded view of individual bunch

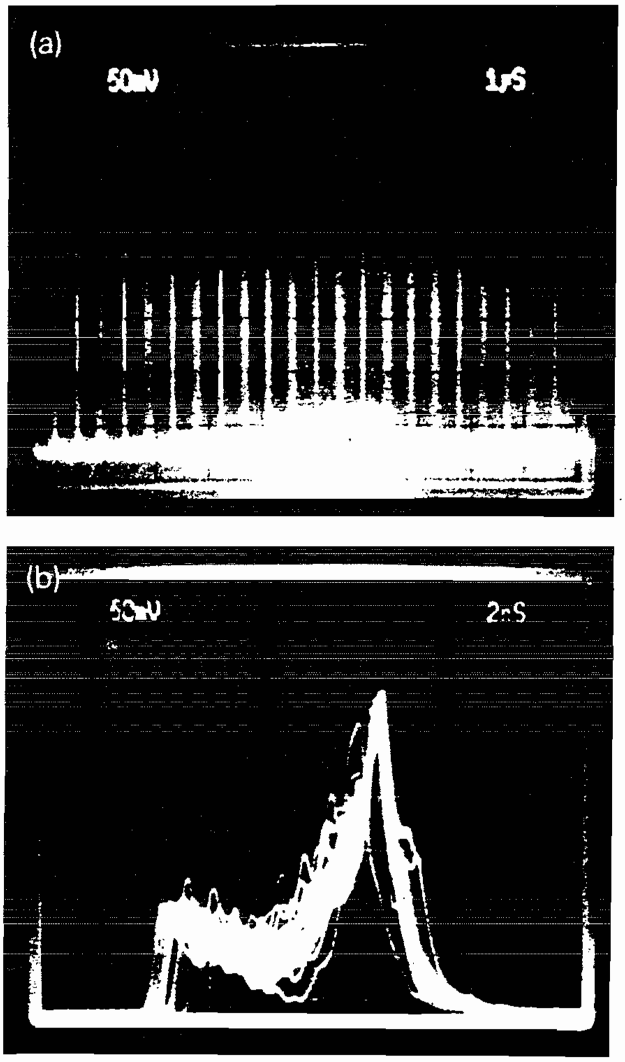

Fig.4.10 3km fibre ring laser: (a) 33rd harmonic mode-locking when the lasing linewidth was 150nm (b) View of individual pulse.

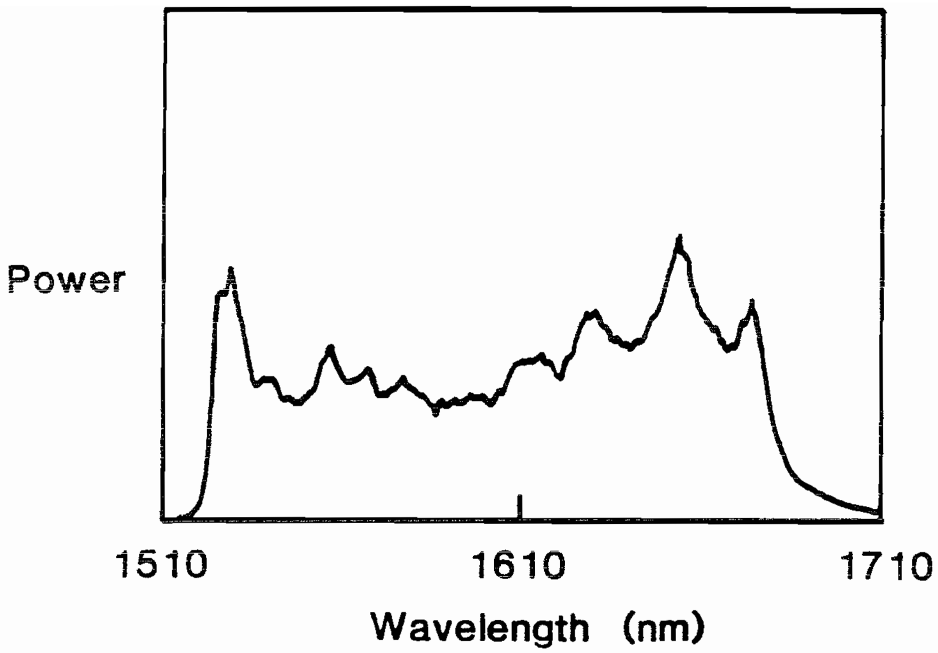

Fig.4.11 Optical spectum of pulses in Fig.4.10

was calculated to be 1.5W. Since the insertion loss of the FP in the region of 1600-1700nm is considerably higher (1-2 dB respectively) than that at 1500nm (0.24dB), even broader lasing linewidths than 150nm should be possible with a different polarising intracavity element.

By replacing the polarisation-independent isolator with a polarisation-dependent one, thereby discarding the need for a fibre polariser, and changing back to the 180m of spun Lo-Bi fibre, our results improved dramatically in terms of the new pulse durations and the stability of the system. The modified experimental setup is shown in Fig.4.12. The remaining output port of the WDM coupler served to monitor the launched pump power and for active pump stabilisation using a servo-loop.

As with the previous set-up (Fig.4.6), long duration (>500 ps) square pulse behaviour was observed with this system at high pump powers. The square pulses were generated at the cavity round-trip frequency with an optical bandwidth of 30-40 nm. However, at low pump powers (<150 mW) the square pulse split into a multitude of smaller pulses of much shorter duration, seemingly randomly spaced within bunches and repeating at the cavity round-trip frequency.

Fig.4.13(a) shows the evolution in the optical spectrum of the laser as the pump power is raised and Fig.4.13(b) shows the corresponding output power hysterisis curve. The CW lasing threshold was 27mW of launched pump power. With appropriate adjustment of the PCs, self-starting mode-locking could be initiated by increasing the launched pump power to a "second" threshold value of 70mW. From the slope efficiencies of the two hysterisis lines the fractional difference in the cavity loss between CW and mode-locked operation was estimated to be ~4-5%. As shown in Fig.4.12(a), the onset of mode-locked operation was marked by an abrupt change in the optical spectrum: The narrow CW line developed into a much broader, approximately sech^2 spectrum which possessed two distinct symmetrically-located side-lobes. The onset of mode-locking was often accompanied by an additional CW component, an additional sharp spectral feature on the soliton spectrum, which could subsequently be eliminated on reduction of the pump power. Note that Fig.4.13(a) is plotted in log intensity to emphasize these features. Side-

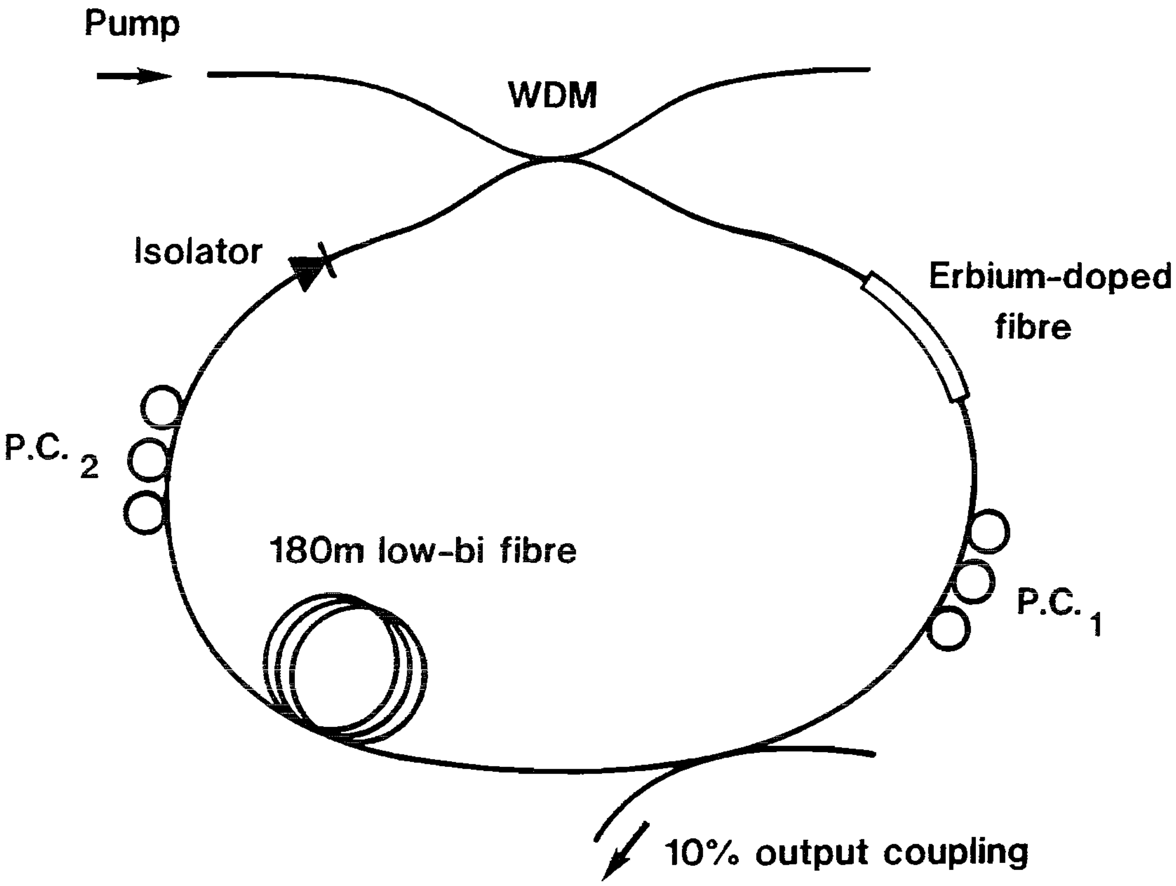

Fig.4.12 Experimental configuration of the soliton ring fibre laser: The fibre polariser used in the set-up of Fig.4.6 has been replaced by a polarisation-dependent isolator.

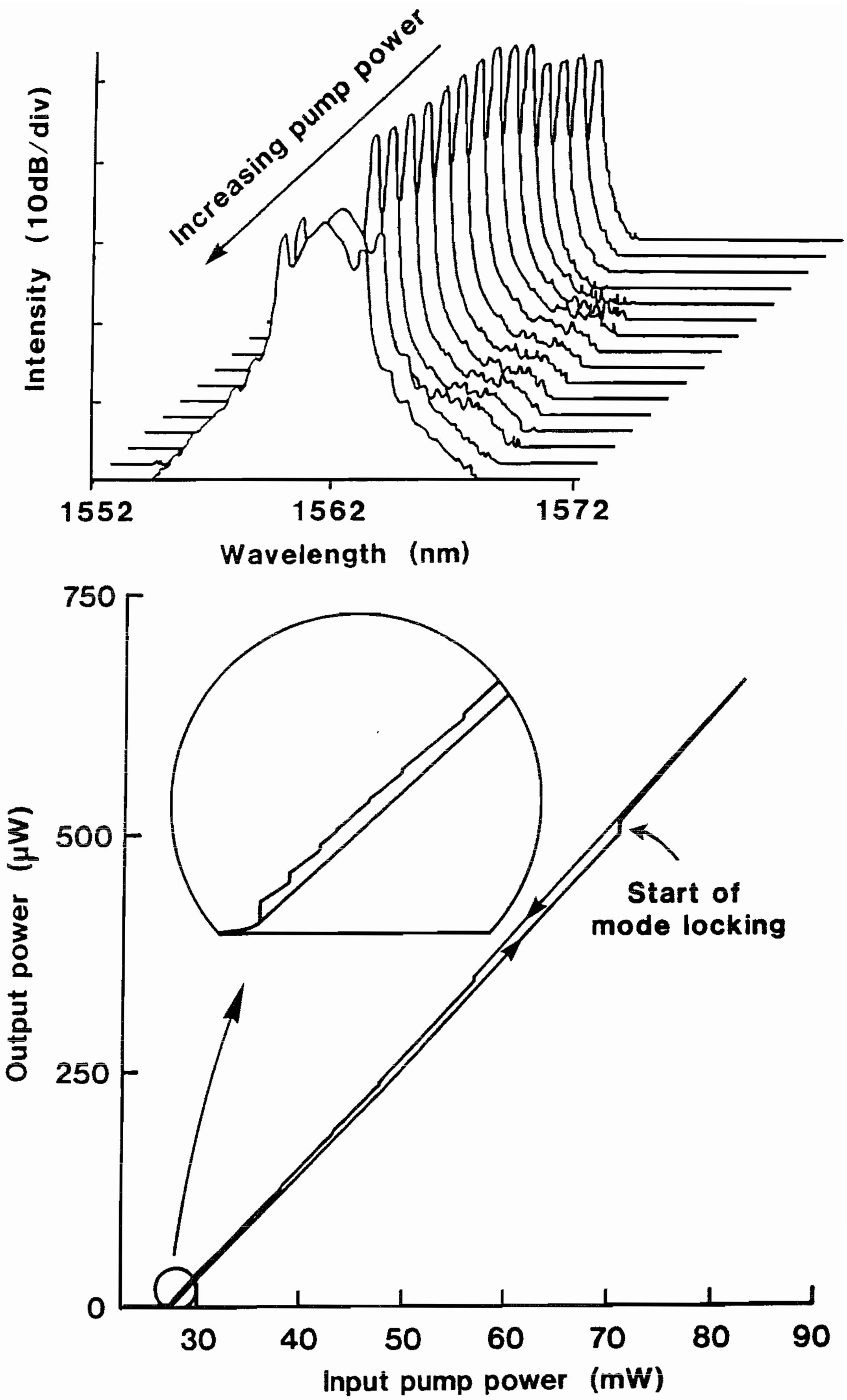

Fig.4.13 180m fibre ring soliton laser: (a) Optical spectrum variation with increasing pump power showing onset of mode-locking and corresponding power hysterisis curve (b).

lobe suppression to > 30dB of the peak level was readily obtainable with this laser by appropriate control of the PC controllers and the input pump power. Once mode-locking had been initiated, gradually decreasing the pump power produced discrete and abrupt downward jumps in the laser output power, coinciding with the disappearance of individual pulses from the cavity. This is shown in the inset of Fig.4.13(b). This process would continue until at a particular pump power, which was very close to the CW threshold power of 27mW, only one pulse would remain inside the laser cavity, indicating fundamental mode-locking. Fig.4.14 shows this time-domain behaviour for an initial number of 8 circulating pulses. Immediately after a jump in pulse number, any excess energy above that required to support the reduced number of pulses is removed by energy shedding into the dispersive wave and absorption at the nonlinear switch. Note that there is a certain "tolerance" in the pulse energy between successive jumps (owing to the slow response time of the detector, the pulse energy is proportional to the height of each pulse on the oscilloscope trace) and this tolerance can be best observed in these last two pictures which demonstrate fundamental mode-locked operation; as the pump power decreases, the intracavity soliton re-adjusts its normalised amplitude A to span part of the 1.5-0.5 range, depending on the cavity losses. The appearance of any pedestal component in the autocorrelation trace as a result of this process was not observed, although slight changes in pulsewidth were observed when a small number of pulses were present in the cavity.

By monitoring the number of pulses in the cavity and recording the change in output power every time a pulse disappeared, the intracavity pulse energy was estimated to be ~48 pJ. An autocorrelation measurement (Fig.4.15) for this particular setting of the PCs revealed a sech^2 pulse shape with a pulse duration of 1.55 ps. The FWHM bandwidth of the optical spectrum was 1.68 nm, thus yielding a time-bandwidth product of 0.32. The energy of a fundamental soliton of 1.55 ps duration for the parameters given above is 47 pJ, which is in excellent agreement with the measured value of 48 pJ and this indicates that the pulses in the laser are fundamental solitons.

Further autocorrelation measurements showed that by tuning the PCs the pulsewidth could be varied between 1.55 ps up to about 4 ps, with corresponding ratios of soliton period

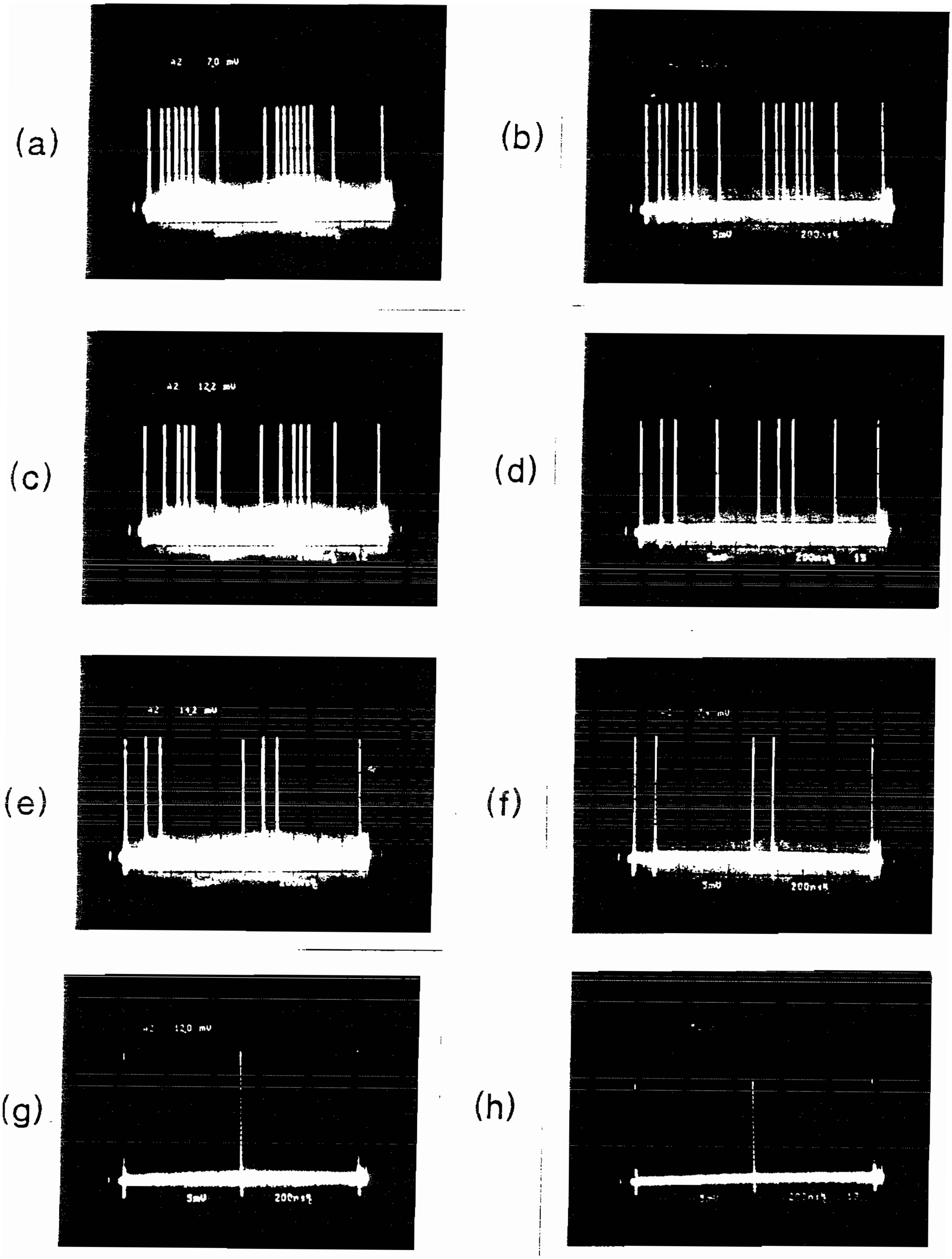

Fig.4.14 Time-domain behaviour in the fibre ring soliton laser, showing the sudden dissapearence in the number of circulating pulses for decreasing pump power.

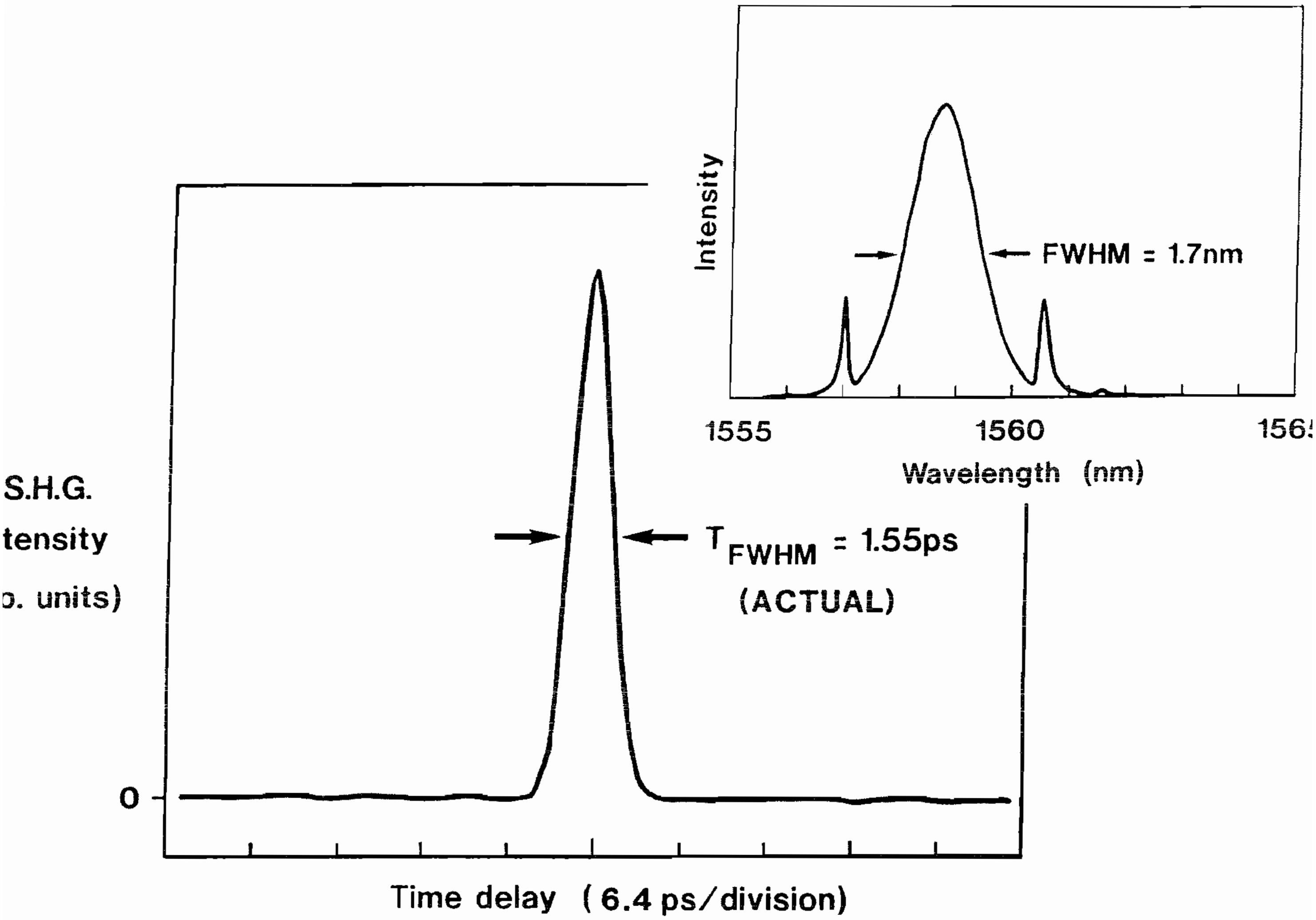

Fig.4.15 Autocorrelation trace and optical spectrum of 1.55ps solitons produced in the 180m fibre ring laser.

to total cavity length of 0.29 and 2 respectively. The autocorrelation traces were found to be well fitted by sech^2 pulse forms and were pedestal free. It should be noted that side-lobe suppression improved as the pulse duration was increased, or, equivalently, as the ratio of the cavity length to soliton period decreased. This fact was expected, according to the theory based on the average soliton approach presented in Chapter 3. The side-lobe intensity was effectively suppressed >40 dB relative to the central peak for the longest duration pulses.

The pulse duration also depended to some extent on the pump power. When operating with the PCs set to give minimum pulse duration, the pulse width narrowed from 2 ps at a pump power of 150 mw down to 1.55 ps at a power of 30 mW. The time-bandwidth products at these pump powers were 0.38 and 0.32 respectively. The wavelength tuning range was of the order of 5 nm, although it should be noted that mode-locked operation could be obtained around both 1.538 and 1.558 μm. In addition, it should be noted that simultaneous, multiple wavelength mode-locked operation could be obtained, as shown in Fig.4.16. This fact highlights an important difference between this laser and the figure-eight laser: In the present case the intensity-dependent loss mechanism that facilitates passive mode-locking varies periodically with wavelength. Since in the Er^{3+} system the laser gain is also wavelength-dependent (see Chapter 2), there exists a case in which two different wavelengths which experience different losses have, nevertheless, exactly the same threshold, thus allowing the dual wavelength operation shown in Fig.4.16. Simultaneous mode-locked operation at as many as three central frequencies was observed during the course of all these experiments.

By changing the setting of the PCs and working at pump powers within the soliton regime of operation ($<$150mW), a new mode of solitonic behaviour was observed, which was quite different from the one previously described. The difference between the two modes of solitonic operation, which from now on will be named as modes #1 and #2, is most strikingly demonstrated by observing their spectral behaviour as a function of pump power, as well as comparing their respective power hysterisis curves.

In mode #1 (Fig.4.17a, same as 4.13a), the central wavelength and spectral shape of the

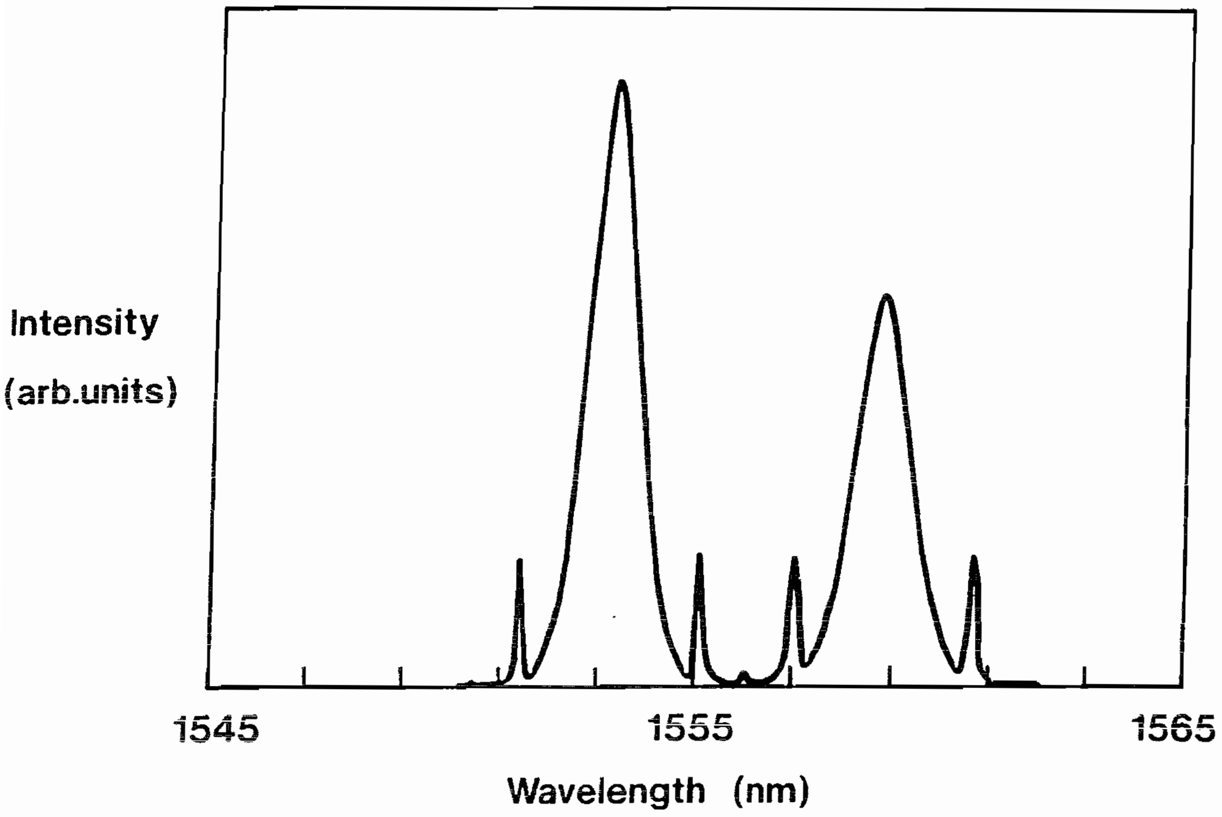

Fig.4.16 Dual wavelength soliton operation.

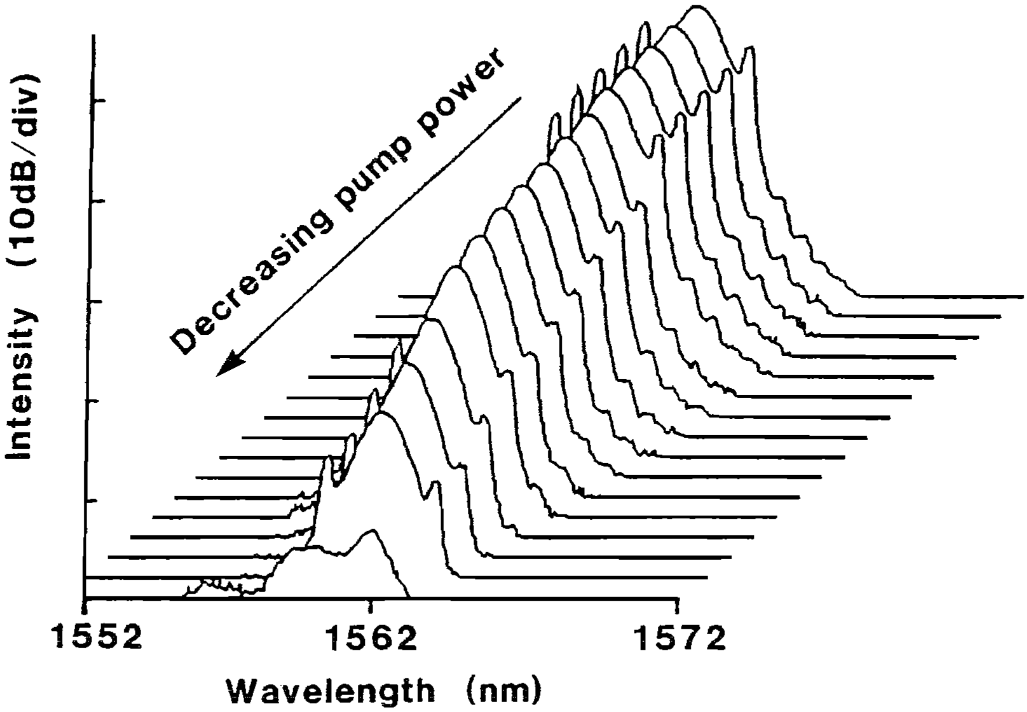

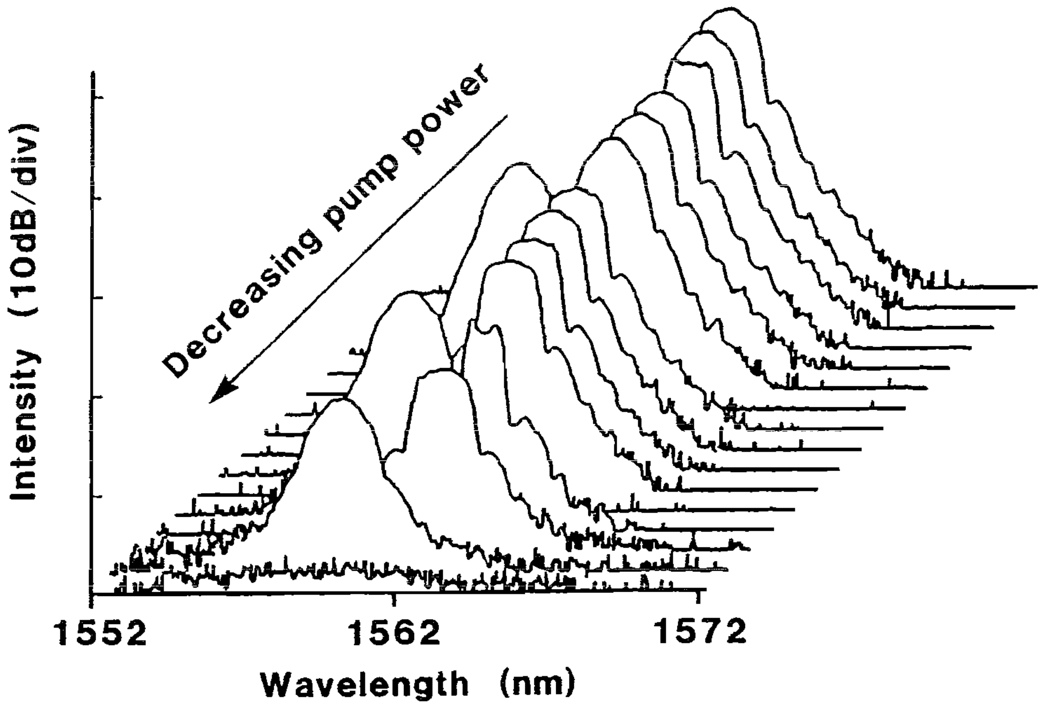

Fig.4.17 (a) Optical spectrum variation for operating mode #1 with decreasing pump power and (b) Optical spectrum variation for operating mode #2 with decreasing pump power. (In both graphs the y axis is logarithmic with arbitrary power units and the resolution is 0.1nm)

pulses remained constant as the pump power was varied. However, the ratio of the amplitude of the side-lobes to that of the central frequency was generally found to depend on the pump power (as well as depending on the PCs setting as mentioned above). In mode #2 (Fig.4.17b), discrete changes in the central wavelength and spectral shape were observed with varying pump power. These became particularly prominent at pump powers close to the CW threshold value.

The output power characteristic of the laser for the two soliton modes is shown in Fig.4.18. In mode #1 (dashed lines, same as in Fig.4.13b) the CW threshold was 27 mW and, as mentioned earlier, mode-locking was found to self-start at a second "threshold" of 70 mW (not shown in Fig.4.18). A higher CW threshold of 30 mW was observed for the system operating in mode #2 (bold lines, Fig.4.18), however the second "threshold" was now reduced to 47 mW. Once initiated, mode-locking this mode could be maintained at pump powers significantly lower than its CW threshold of 30mW. Abrupt jumps, both upwards and downwards, in the output power were observed in this instance. Jumps downwards were associated with pulse disappearances and were not constant from jump to jump particularly when a small number of pulses remained in the cavity. The (much smaller and more difficult to see) jumps upwards were associtaed with discrete wavelength shifts ($\sim$3nm). The fundamental difference between these two solitonic modes is currently not understood.

In order to monitor the state of polarisation (SOP) of the circulating light before it reaches the optical isolator, an extra 90:10 coupler was placed immediately before the polarising optical isolator and the SOP of light emerging from the output port of this coupler was monitored as a function of pump power by using a real-time polarisation analyser (Electro-Optic Development). Unfortunately, this instrument employs a fibre input lead of unknown birefringence and therefore a measurement of the absolute state of polarisation at the polariser input was not possible. The device could however be used to detect changes in the polarisation state. The results of the measurements are shown in Fig.4.19. It was observed that the SOP at the output port remained approximately constant during CW operation up until the onset of mode-locking, at which point an abrupt change in the SOP was observed. The SOP remained fixed at pump powers

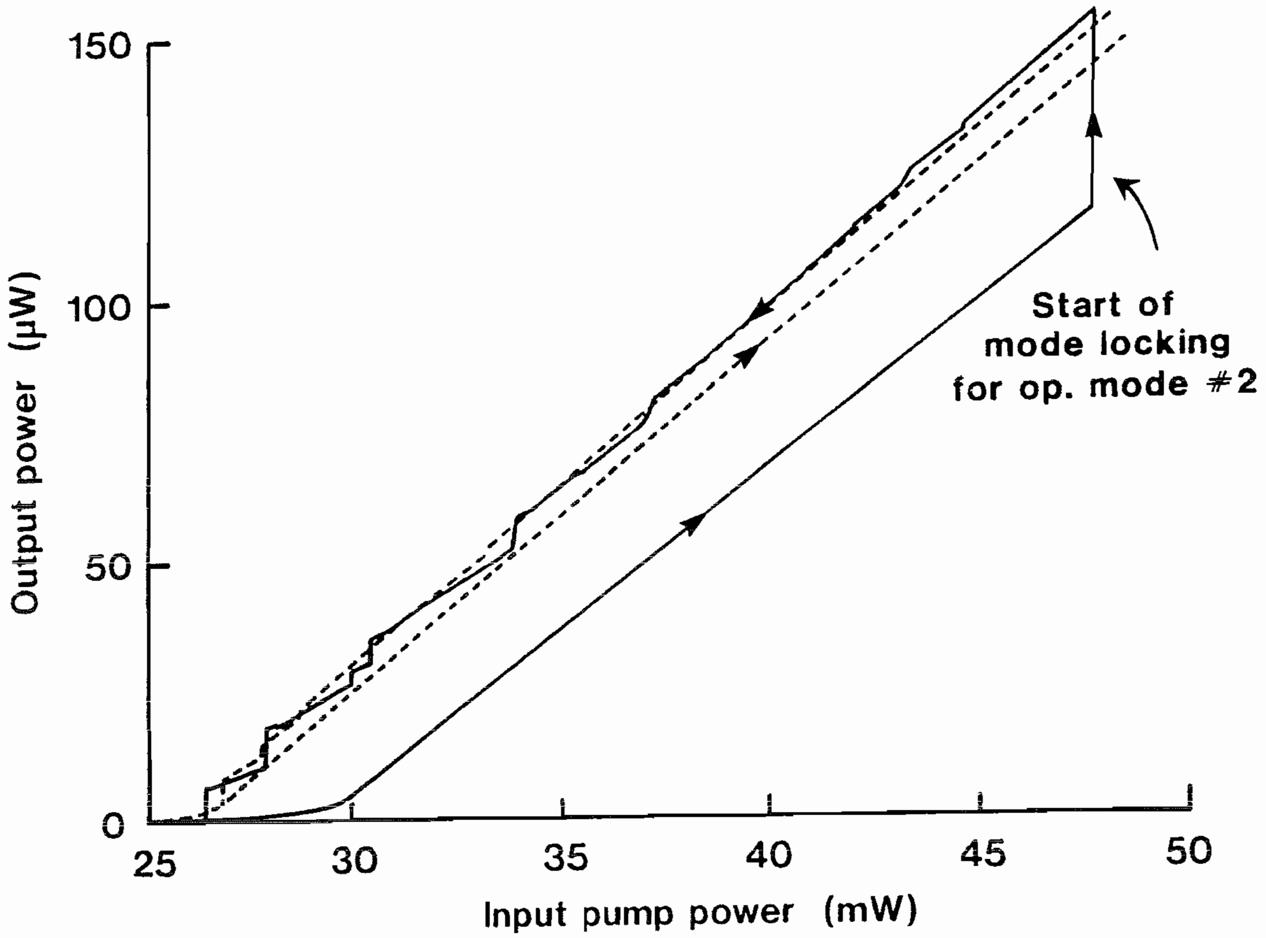

Fig.4.18 Power hysterisis curves for operating modes #1 (dashed) and #2 (bold).

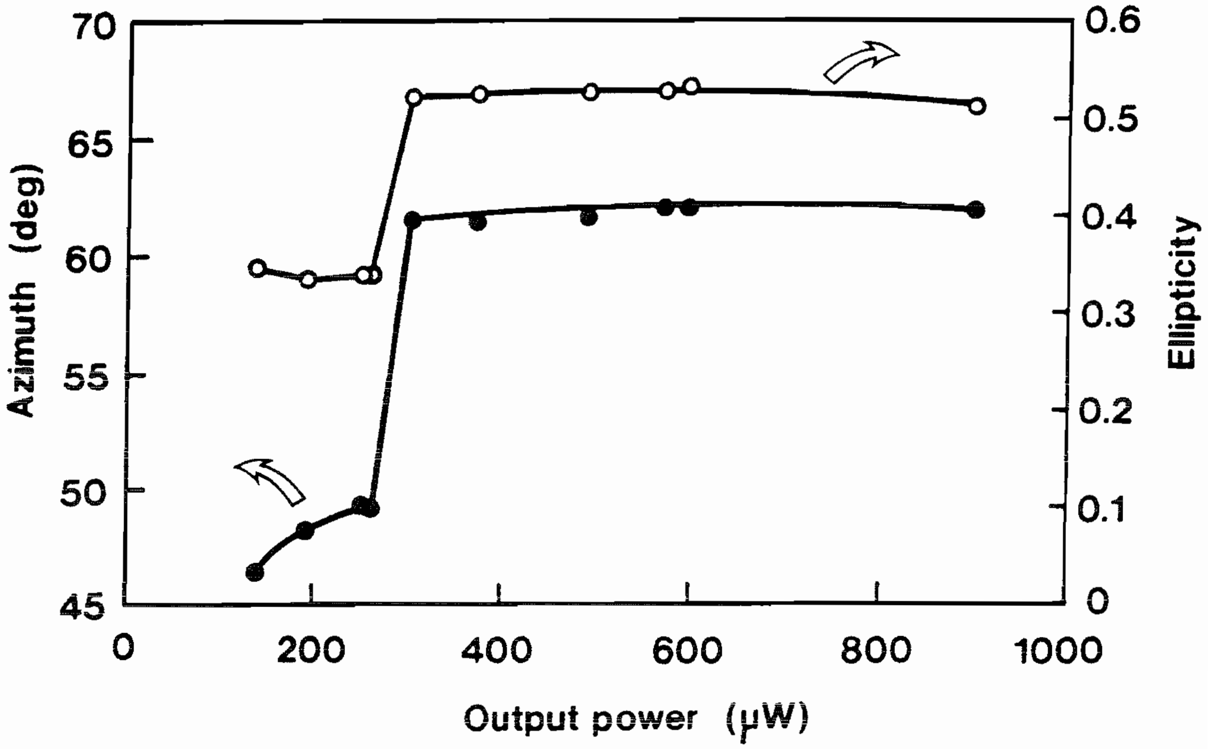

Fig.4.19 Ellipticity and azimuth of the light emerging from the output port located before the isolator as a function of pump power.

beyond this point. These observations provide strong evidence that NLPE provides the mode-locking mechanism within this laser and are similar to those published by other groups [20,21], where azimuth changes between 1^0 and 8^0 were reported.

The LoBi fibre section was then cut back to a length of 45m and subsequently to 3m in order to measure the minimum pulse width obtainable as a function of the total cavity length. The length of the residual fibre in the cavity i.e. EDFA, isolator pig-tails and coupler leads was ~15m. The shortest pulses obtained had a duration of 720 fs with the 3m Lo-Bi fibre section. Similar measurements were made with a section of standard telecommunications fibre. Lengths of fibre ranging from 200m down to 3m were tested. The shortest pulse observed with this fibre was 700fs. Fig.4.20(a) shows the autocorrelation trace of an incident in which the intracavity soliton pulses formed coupled pairs. This is also reflected in the optical spectrum (Fig.4.20(b)) which is modulated at 1.67nm (200GHz), corresponding to the observed 4.3ps pulse separation. The cavity length was 30m. Fig.4.21 summarises the pulsewidth dependence on the total cavity length for the two types of fibre used. It is seen that the pulsewidth follows an approximate $L^{1/2}$ dependency in both cases which is in agreement with the theory on the resonant loss mechanism presented in the previous chapter. It should be noted that, with a maximum pump power of 100 mW, no spontaneous mode-locking was observed without at least a 3m section of relatively low birefringence ($L_{b0}>2m$) fibre within the fibre laser cavity. When sections of medium to highly birefringent fibre ($L_{b0}<0.1m$) were incorporated within the cavity no mode-locking was observed, irrespective of the fibre length used. Finally, it must also be mentioned that in terms of ability to self-start, spectral quality and overall stability, the Lo-Bi fibre produced significantly better results than the ordinary telecommunications fibre.

4.4. NON-LINEAR POLARISATION EVOLUTION IN A FABRY-PEROT FIBRE LASER CONFIGURATION

The NLPE method of passive mode-locking can also be applied to a Fabry-Perot cavity configuration. However, the experimental results presented below demonstrate a dramatic increase in the self-starting threshold for mode-locking compared to the ring laser system described previously. Section 4.4.1 provides a description of the laser system and presents the experimental results.

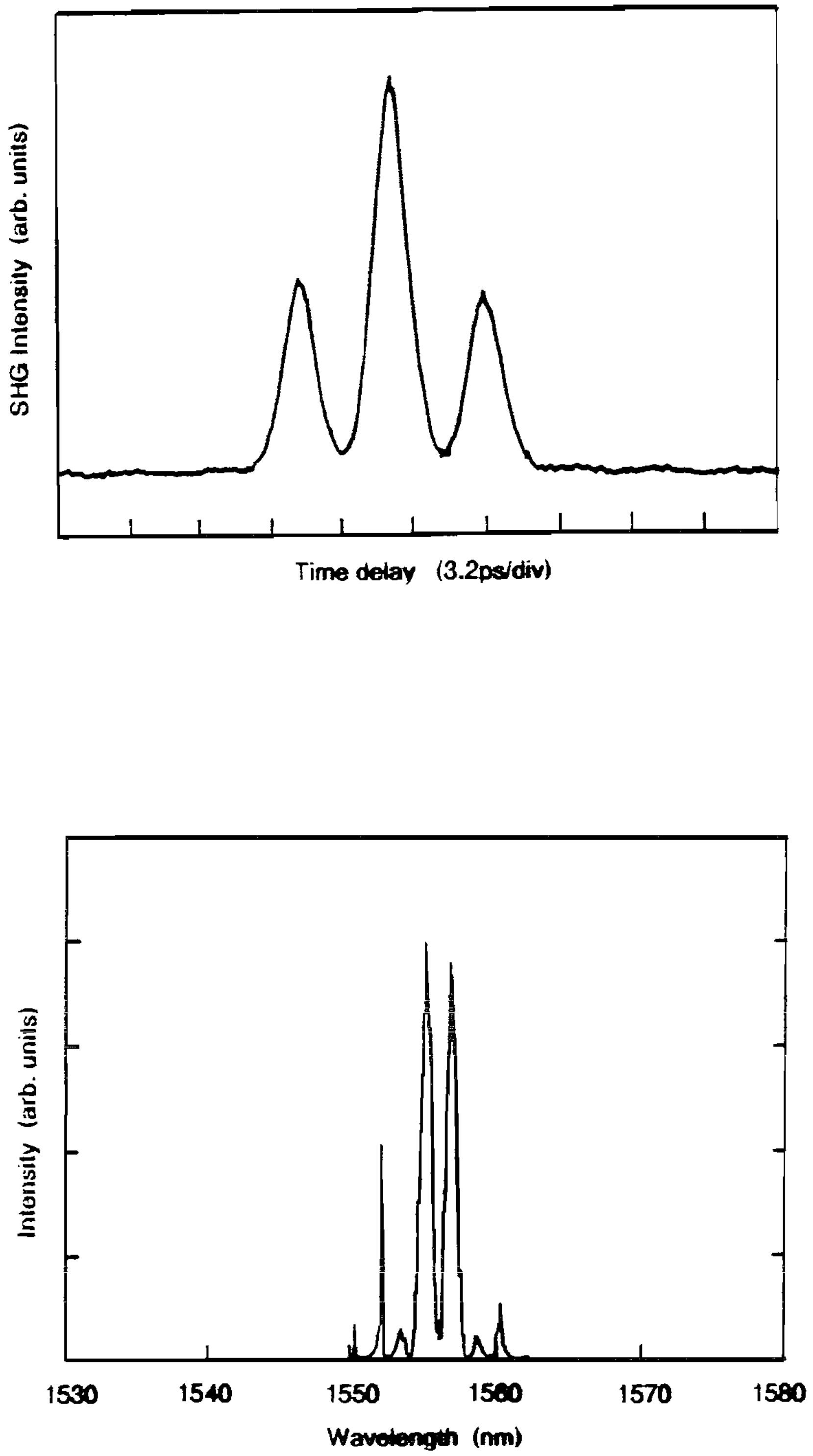

Fig.4.20 (a) Autocorrelation and (b) optical spectrum of two soliton pulses circulating in a 30m fibre ring laser and separated by 4.3ps.

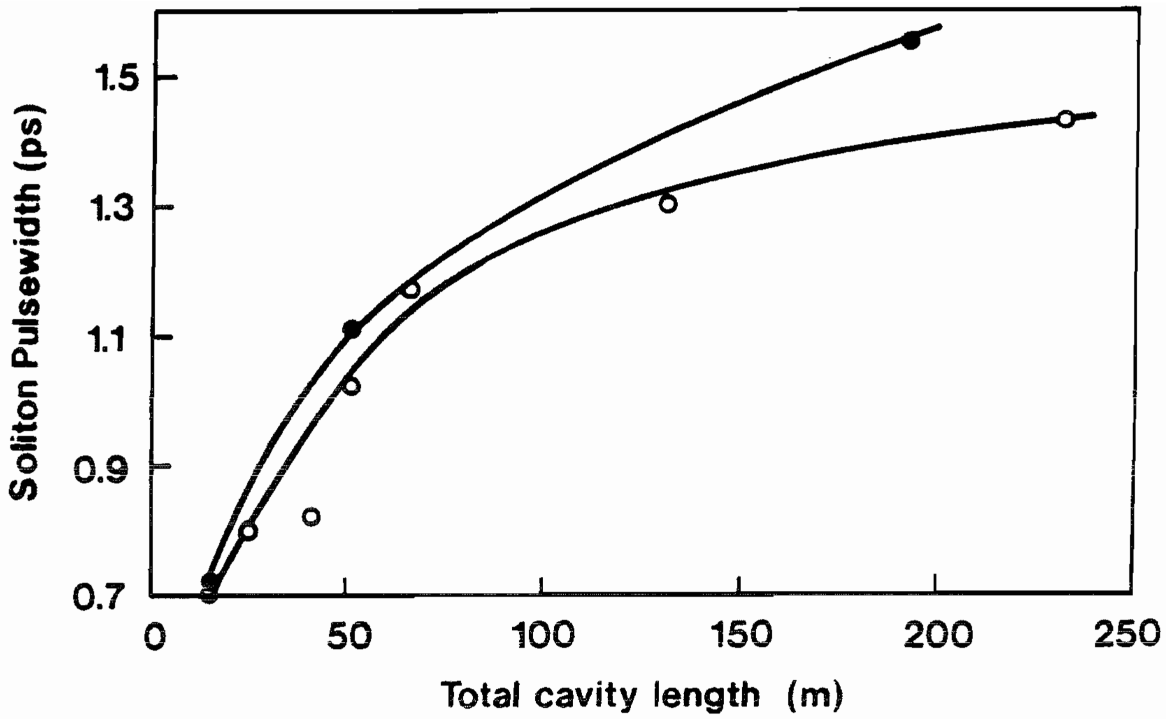

Fig.4.21 Minimum soliton pulsewidth vs total cavity length for the two types of fibre used.

4.4.1 Experimental Details and Results

Fig.4.22(a) depicts the laser cavity schematic and Fig.4.22(b) the actual experimental set-up. The system comprised 40m of Lo-Bi spun fibre (NA=0.12, λ_c=1250nm, D=17 ps/nm/km, A_{mode}=124μm^2 and beat length >10m), 3m of Er^{3+}-doped fibre (dopant concentration =800ppm, NA=0.15, λ_c=960nm), a fibre polariser (FP) and a polarisation controller (PC) situated just before the fibre polariser. Pumping was provided by a Ti:Sapphire laser operating at 980nm and the pump power was actively stabilised with a feedback circuit and a Bragg-cell intensity modulator placed in front of the launch optics. A 980/1550nm fibre WDM was used to couple the pump light into the Er-doped fibre and the laser cavity was formed by butting the end of port #2 of the WDM against a 1550nm 99% reflecting mirror (M1) and the fibre polariser end against an 85% reflecting output mirror (M2).

Using the Jones calculus approach as previously performed for the ring laser cavity, the linear cavity transmission for the system depicted in Fig.4.22(a) is given by

$$T=1-\frac{1}{2}\sin^2(2\theta)\left[1-\cos\left[2\pi\frac{L}{L_{b_0}}\right]\right] \tag{4.14}$$

where L is the length of the birefringent fibre and the polariser is assumed to be located at one end of the cavity. The angle θ between the polariser axis and the x-axis of the fibre birefringence in the experiment is specified by the orientation of the PC.

With the PC adjusted so as to minimise the intracavity loss, the laser had a CW threshold of 25mW launched pump power. The onset of mode-locked operation was marked by an abrupt change in the optical spectrum and output power at a particular value of the launched pump power (450mW). Once initiated, mode-locked operation could be sustained to powers within a few mW of the CW threshold (25mW). The self-start pump power threshold is considerably higher than that required for self-starting mode-locked operation in the Fig-8 and ring configurations presented earlier (typically 50-80 mW). In general, the modes within a laser cavity are unevenly spaced due to the effects of

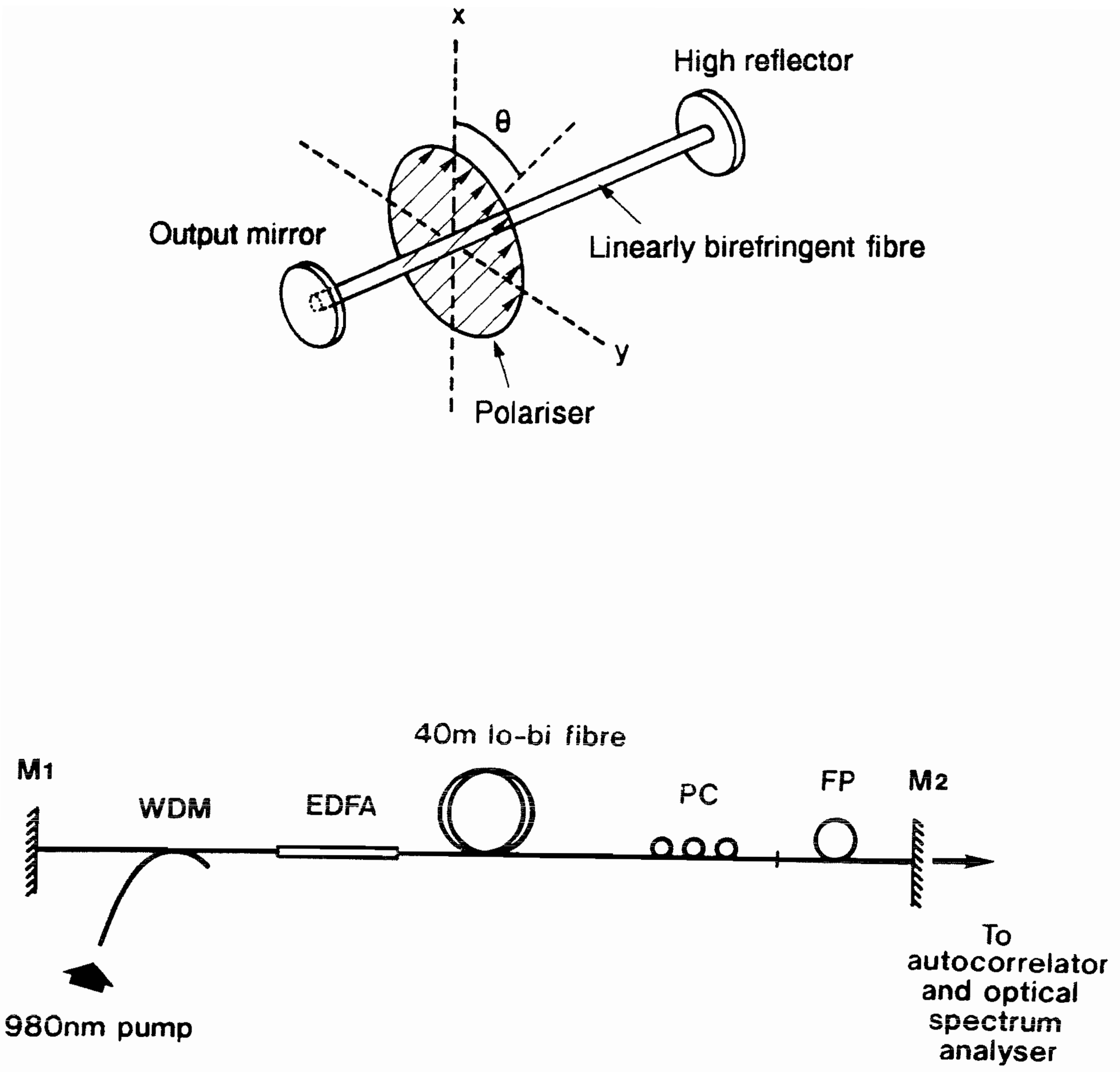

Fig.4.22 (a) Fabry-Perot fibre laser cavity schematic and (b) actual experimental arrangement.

spurious reflections [10] and, in the case of a Fabry-Perot laser, due to the formation of complex refractive index grating in the gain medium set up by the two counter-propagating waves [11]. This uneven mode-spacing leads to beat-note line broadening and hence limits the lifetime of the mode-beating fluctuations. Fig-8 and ring fibre lasers are inherently travelling-wave lasers and therefore have a significant advantage over their Fabry-Perot counterpart in which the effect of spatial hole burning sets up the refractive index grating, thus leading to substantial beat-note line broadening. Subsequently the intensity of the fluctuations and hence the pump power required to initiate self-starting mode-locking is significantly higher in Fabry Perot cavities, in general agreement with the work of Zehetner and Krausz [12,11]. It should also be noted that the effects of spurious reflections are significantly less in a unidirectional cavity due to the presence of the isolator which will also contribute to the low self-start threshold.

Two distinct regimes of mode-locked operation were observed depending on both pump power and the setting of the PC: in the "square pulse" regime, long duration ($>$500ps) square pulses at the cavity round-trip frequency (2MHz) were observed, as was also discussed in the previous experiments on the Figure-8 laser and the NLPE ring laser. These pulses were characterised by broad bandwidths of 10-15nm. In the soliton regime and at high pump powers (around the self-start threshold $\approx$450 mW) tightly-packed bunches of solitons exhibiting chaotic behaviour were observed. As the pump power was gradually decreased, these bunches would break up to produce stable bunches of randomly-spaced fundamental solitons, the bunches repeating at the cavity round trip period. At pump powers close to the cw laser threshold, as few as two pulses were obtained within the cavity. Autocorrelation measurements (see Fig.4.23(a)) showed a full width at half maximum of 2.5ps, corresponding to a pulse duration of 1.6ps. The spectral width was 1.5nm (see Fig.4.23(b)), yielding a time-bandwidth product of 0.32, as expected for transform limited sech^2 pulses.

When the 15% output coupling mirror was replaced by a 50% output coupler, thus reducing the intracavity power, it was not possible to obtain stable soliton operation at low pump powers. At best, only a mixed operating regime of square and soliton pulses could be obtained. With the output coupler increased further to 85%, no pulses could be

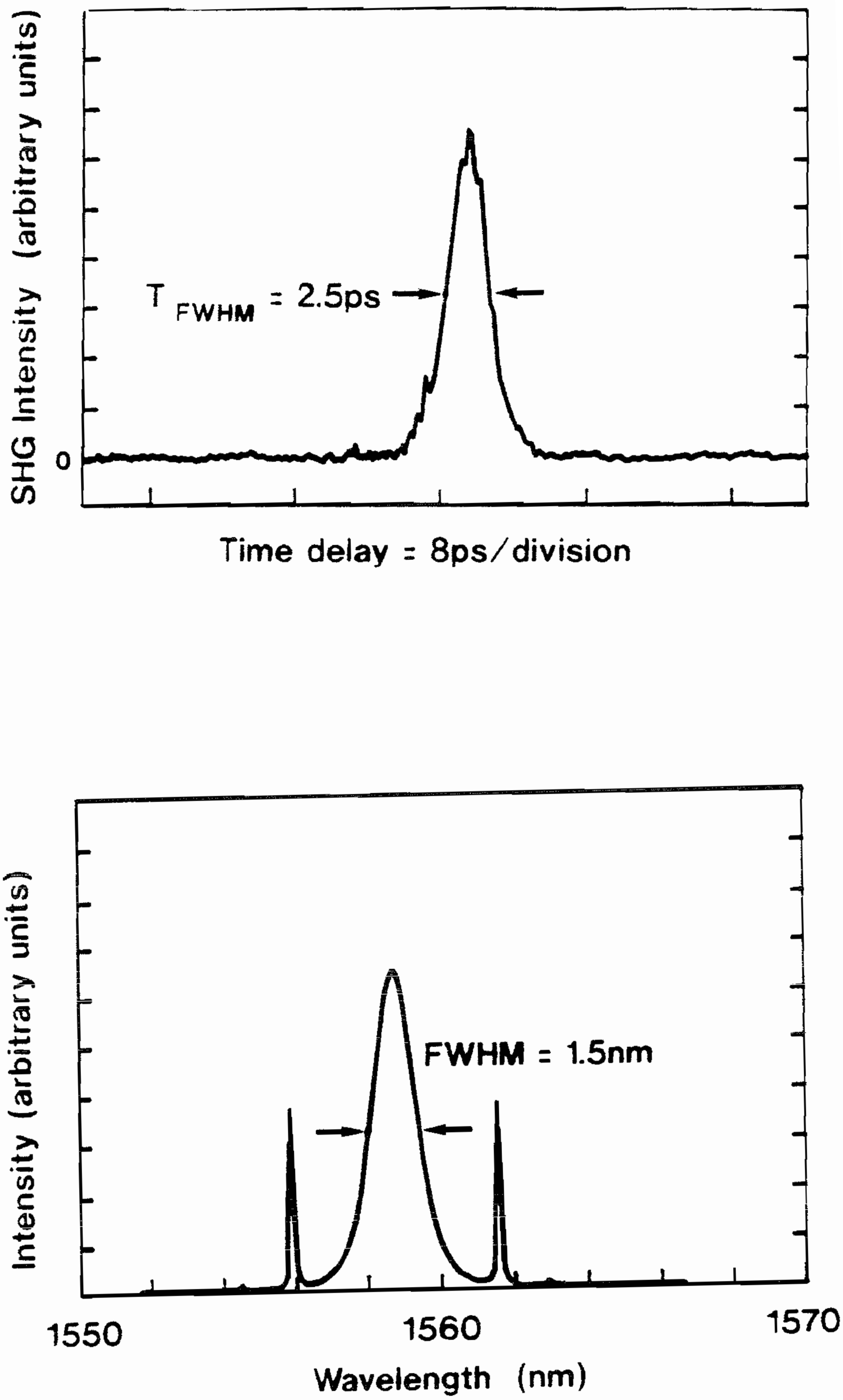

Fig.4.23 (a) Autocorrelation trace and (b) optical spectrum of the soliton pulses produced in the Fabry-Perot cavity configuration.

obtained at all, possibly because the mode-locking threshold is then higher than the maximum available pump power (700mW launched). No simultaneous dual-wavelength modelocked operation as previously seen with the ring laser configuration was ever observed in the course of these experiments.

The two dielectric mirrors were then replaced by two highly reflective fibre gratings of 1nm bandwidth in order to form an all-fibre laser cavity. The results were, however, disappointing: When both gratings were used, no mode-locking was observed and at best, square-pulsed operation was observed when only one reflection grating was used and a dielectric mirror on the other side of the cavity. The absence of soliton formation is thought to be due to the narrow bandwidth and the high dispersion that these fibre gratings possess [13]. Fig.4.24 displays the gratings' wavelength transmission characteristics and Fig.4.25 shows a picture of the square pulse and its optical spectrum as transmitted from the grating side of the cavity. Since the grating bandwidth is only 1nm, the optical spectrum shows the band of frequencies generated by self-phase modulation in one cavity round trip.

4.5 SOLITONS AND NON-LINEAR BIREFRINGENCE

When considering propagation in a non-linear birefringent medium, the NLSE that governs soliton wave propagation in a one-dimensional non-linear medium (eqn.(3.21)) is split into two coupled NLSEs [14]:

$$i\left[\frac{\partial u}{\partial z}+\delta\frac{\partial u}{\partial t}\right]+\frac{1}{2}\frac{\partial^2 u}{\partial t^2}+\left[|u|^2+\frac{2}{3}|v|^2\right]u+\frac{1}{3}v^2u^*e^{-i\frac{8z_0}{L_{b_0}}z}=0 \qquad (4.15a)$$

$$i\left[\frac{\partial v}{\partial z}-\delta\frac{\partial v}{\partial t}\right]+\frac{1}{2}\frac{\partial^2 v}{\partial t^2}+\left[|v|^2+\frac{2}{3}|u|^2\right]v+\frac{1}{3}u^2v^*e^{i\frac{8z_0}{L_{b_0}}z}=0 \qquad (4.15b)$$

where u,v are the normalised amplitudes for the two orthogonal polarisations and δ is a normalised birefringence parameter defined as follows:

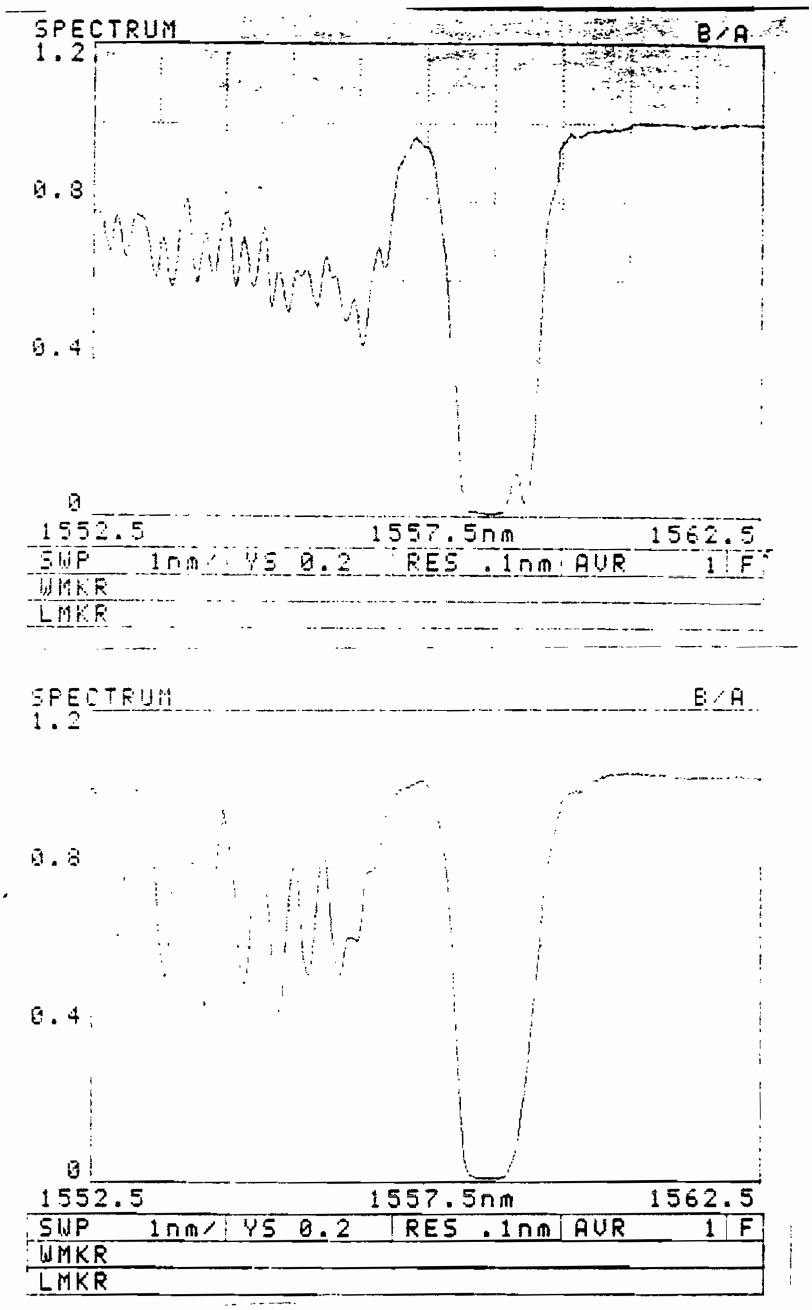

Fig.4.24 Wavelength transmission characteristics of the two fibre gratings used to replace the dielectric mirrors.

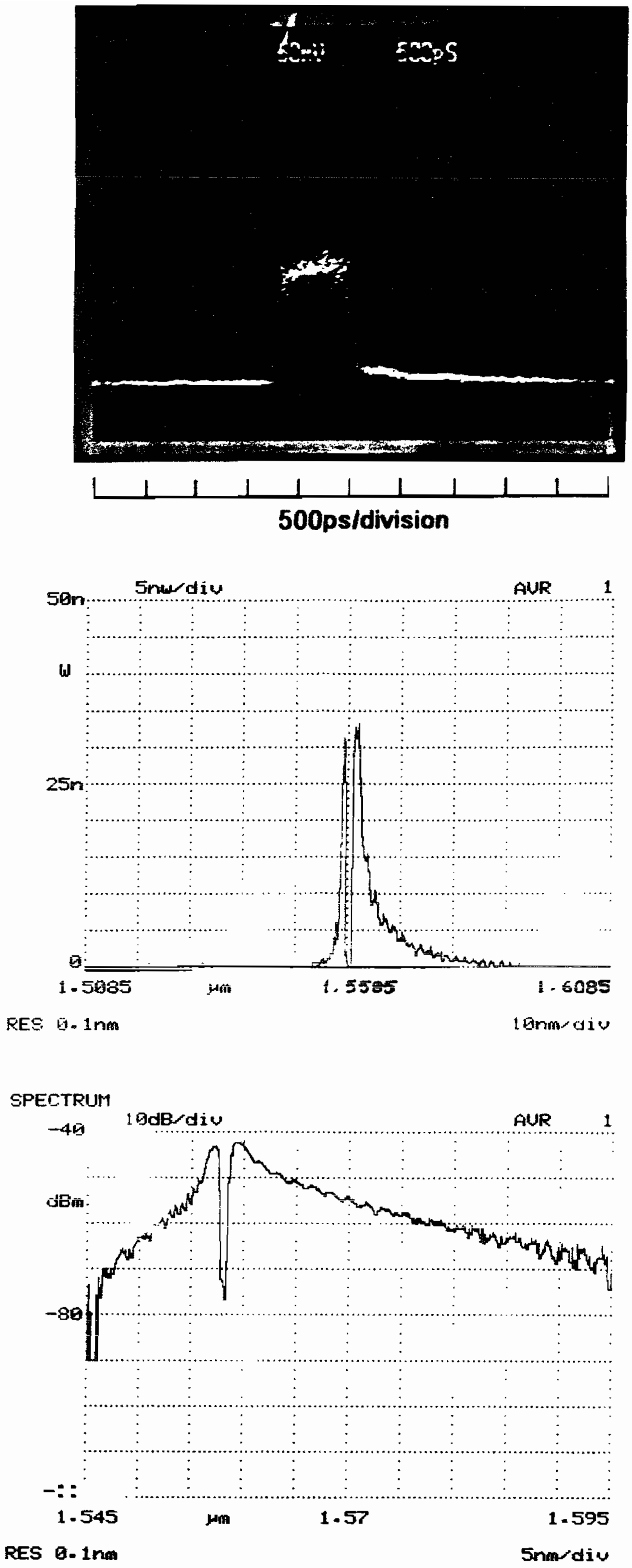

Fig.4.25 (a) Oscilloscope trace and (b) optical spectrum of the square pulses produced in the Fabry-Perot cavity with the output mirror replaced by a fibre grating.

$$\delta \equiv \frac{\pi}{2\cosh^{-1}\left(\sqrt{2}\right)}\frac{\tau_{FWHM}}{\lambda|D|L_{b_0}} \qquad (4.16)$$

As an example, if $\tau_{FWHM}=1$ ps, D=-17 ps/nm/km, $\lambda=1.56$ μm and $L_{b0}=1$ m, $\delta=0.067$ and $8z_0/L_{b0}\approx 184$. If $8z_0/L_{b0} >> 1$, ie the soliton phase period is much greater then the fibre beat length, then the exponentially varying terms in eqs.(4.15) can be neglected.

The solution of the system of eqn.(4.15) under specified conditions has been studied by many authors [15-19], although, to the author's knowledge and at the time of writing of this thesis, a complete study of the system has yet to appear. The basic conclusions of these studies that are of interest here can be summarised as follows:

(a) For moderate values of δ (0.1-0.8) and assuming that $8z_0/L_{b0} >> 1$ so that the exponentially varying terms can be neglected, it has been found that for a linearly polarised input soliton pulse of the form Asech(t) launched at an angle with respect to the birefringence axes there is a critical threshold for the value of A above which, the nonlinearity is sufficient to constrain both the spreading that is due to dispersion and the splitting that is due to birefringence, thus keeping the two partial pulses bound together. More specifically, above threshold, if the input pulse is launched *unevenly* with respect to the fibre birefringence axes, then the largest amplitude pulse is found to "capture" part of the pulse travelling along the other axis, the two ultimately travelling together without any further energy exchange. If, on the other hand, the input pulse exites both othogonal modes *equally*, the two partial pulses are seen to move with respect to each other in an oscillatory fashion without energy exchange.

(b) For lower values of δ such that the exponentially varying terms of eqns.(4.15) can no longer be neglected, it has been found that if the input pulse is launched along the fast axis its energy is eventually transferred permanently to the slow axis, which, as in the CW wave case (ie with no dispersion effects included) is the stable axis. Thus, although in the CW case the energy cannot relax to the stable mode and is forced to oscillate between the two modes, the extra dimension introduced by the dispersion allows the energy to relax to the stable mode by shedding radiation from the central pulse.

The important thing to note from these analyses is that in a birefringence-polariser transmission situation, solitons are equally, if not more, flexible compared to square pulses: That is, if a birefringent fibre laser includes an intracavity polariser, a soliton pulsewidth can always be found, within the allowed limits set by effects such as the resonant loss or the soliton self-frequency shift, which permits stable and lossless propagation, the same way that a certain "switching" power exists for square pulses in order to pass through the polariser without loss. This is because both parameters of the coupled system of eqn.(4.15) which determine the soliton evolution, ie δ and $8z_0/L_{b0}$, depend on τ, the soliton pulsewidth. This observation agrees with the experimental results which demonstrated that the pulsewidth may be varied from 5 to 1.5 ps by changing the position of the polarisation controllers. Although this variation may initially seem insignificant, note that the ratio $8z_0/L_{b0}$ is changed appreciably due to the quadratic dependence of z_0 on τ. Another point to note is that the normalised birefringence parameter δ is inversely proportional to β_2, the group velocity dispersion. Hence, decreasing β_2 should result in shorter soliton pulsewidths in order to keep an acceptable value for $\delta < 0.9$ to ensure stable soliton propagation. As was discussed in Chapter 3, however, the ultimate pulsewidth is still determined by the resonant loss mechanism.

4.6 CONCLUSIONS

Non-linear polarisation evolution provides an simple and effective way for passive mode-locking of fibre lasers. As with the Figure-8 laser, it can produce soliton pulses of picosecond and subpicosecond duration and it also has the additional advantage of avoiding the soliton splitting and the subsequent interferometric recombination that is required in Figure-8 lasers, thus keeping the soliton more or less intact at each round trip. The passively mode-locked fibre lasers produced by the NLPE technique were characterised in terms of their modes of operation, hysterisis curves, cavity length and fibre birefringence. It was demonstrated experimentally that standing-wave configurations, such as a Fabry-Perot, have a substantially higher mode-locking threshold over travelling-wave arrangements such as ring or Figure-8 lasers and is in confirmation with recent theoretical investigations [11]. The existence of NLPE as the mechanism behind the passively mode-locked operation was verified by state of polarisation measurements.

REFERENCES:

1. L. Dahlstrom: "Passive mode-locking and Q-switching of high power lasers by means of the optical Kerr effect" *Opt. Commun.* **5** p.157 (1972).

2. K. Sala, M. C. Richardson and N. R. Isenor: "Passive mode-locking of lasers with the optical Kerr effect modulator" *IEEE J. Quant. Electron.* **QE-13** p.915 (1977).

3. M. Hofer, M. E. Fermann, F. Haberl, M. H. Ober and A. J. Schmidt: "Mode-locking with cross-phase and self-phase modulation" *Opt. Lett.* **16** p.502-504 (1991).

4. P. D. Maker, R. W. Tehrune and C. M. Savage: "Intensity-dependent changes in the refractive index of liquids" *Phys. Rev. Lett.* **12** p.507 (1964).

5. H. Winful: "Self-induced polarisation changes in birefringent optical fibres" *Appl.Phys.Lett.* **87** p.213 (1985).

6. H. Winful: "Polarisation instabilities in birefringent nonlinear media: application to fibre-optic devices" *Opt. Lett.* **11** p.33 (1986).

7. R. H. Stolen, J. Botineau and A. Ashkin: "Intensity discrimination of optical pulses with birefringent fibres" *Opt. Lett.* **7** p.512 (1982).

8. K. Kitayama, Y. Kimura and S. Seikai: "Fibre-optic logic gate" *Appl. Phys. Lett.* **46** p.317 (1985).

9. S. J. Garth and C. Pask: "Polarisation behaviour in lossy non-linear birefringent optical fibres" *Opt. and Quant. Electron.* **22** p.37 (1990).

10. H. Haus and E. P. Ippen: "Self-starting of passively mode-locked lasers" *Opt. Lett.* **16** p.1331 (1991).

11. F. Krausz and T. Brabec: "Passive mode-locking in standing-wave laser resonators" *opt. Lett.* **18** p.888 (1993).

12. J. Zehetner, Ch. Spielmann and F. Krausz: "Passive mode-locking of homogeneously and inhomogeneously broadened lasers" *Opt. Lett.* **17** p.871-873 (1992).

13. D. Taverner: Personal communication.

14. C. R. Menyuk: "Stability of solitons in birefringent optical fibres. II. Arbitrary amplitudes" *J. Opt. Soc. Am. B* **5** p.392 (1988).

15. K. J. Blow, N. J. Doran and D. Wood: "Polarisation instabilities for solitons in birefringent fibres" *Opt. Lett.* **12** p.202 (1987).

16. D. N. Christodoulides and R. I. Joseph: "Vector solitons in birefringent nonlinear

dispersive media" *Opt. Lett.* **13** p.53 (1988).

17. M. V. Trantik and J. E. Sipe: "Bound solitary waves in a birefringent fibre" *Phy. Rev. A* **38** p.2011 (1988).

18. S. Trillo, S. Wabnitz, E. M. Wright and G. I. Stegeman: "Polarised soliton instability and branching in birefringent fibres" *Opt. Commun.* **70** p.166 (1989).

19. E. M. Wright, G. I. Stegeman and S. Wabnitz: "Solitary-wave decay and symmetry-breaking instabilities in two-mode fibres" *Phys. Rev. A* **40** p.4455 (1989).

20. M. Hofer, M. H. Ober, F. Haberl and M. E. Fermann: "Characterisation of ultrashort pulse formation in passively mode-locked fibre lasers" *IEEE J. Quantum Electron.* **QE-28** p.720 (1992).

21. R. P. Davey, N. Langford and A. I. Ferguson: "Role of polarisation rotation in the mode-locking of an erbium fibre laser" *Electron. Lett.* **29** p.758 (1993).

CHAPTER 5

LONG MODE-LOCKED FIBER LASERS FOR SENSING APPLICATIONS

5.1 INTRODUCTION

This chapter investigates the potential of using long mode-locked fibre lasers for distributed temperature sensing (DTS). In a conventional DTS system a high-power short pulse is launched into an optical fibre and the temperature-dependent Raman backscattered signal, produced by the pulse travelling along the fibre, is detected using a fast detector and time-averaging techniques. In principle, a fundamentally mode-locked long fibre laser should be capable of generating a measurable Raman signal, with the fibre laser cavity forming the sensing element.

The first section of this chapter examines the relative merits of such a fibre laser DTS system with respect to that of a commercially available system which uses a source external to the sensing fibre. Three experimental mode-locked system configurations that could potentially form part of a DTS system are presented, followed by an analysis of the experimental results. In this analysis the theory of active mode-locking as developed by Kuizenga and Siegman (K-S) [1], is extended to include the effects of intracavity dispersion which become significant at long fibre laser resonator lengths.

5.2 THEORETICAL CONSIDERATIONS

As mentioned in the introduction, a long mode-locked fibre laser may be used as a distributed temperature sensor. Assuming that there is only one pulse circulating inside the cavity, the backward-scattered ratio of the Stokes and the anti-Stokes Raman light allows the determination of the absolute temperature at each point according to the formula [2]

$$R(T)=\left[\frac{\nu_a}{\nu_s}\right]^4 \exp\left[-\frac{h\Delta\nu}{kT}\right] \tag{5.1}$$

where $\Delta\nu = |\nu_{a \text{ or } s} - \nu_i|$ is a chosen value of the Stokes/anti-Stokes frequency shift from the laser light ν_i at which the ratio is measured, T is the absolute temperature, and k, h are Boltzmann's and Planck's constants respectively. The $(\nu_\alpha/\nu_s)^4$ factor is a consequence of Rayleigh scattering.

This method of detection has been used with success in the past [2] and is given the acronym DART (Distributed Anti-Stokes-Raman Thermometry). In the state-of-the-art, commercially available system at present, high (~250nJ) energy pulses from a Q-switched laser are injected into a passive multimode fiber at a repetition rate of ~4kHz and the backscattered ratio at a convenient wavelength is subsequently measured and averaged. The backward scattered anti-Stokes signal for a launched energy of 1 J is given by [3]

$$P_{A-S}(z)=S\alpha(z)\eta_{A-S}(z,T)v_g e^{\left(-\int_0^z(\alpha(z')+\alpha_{bA-S}(z'))dz'\right)} \tag{5.2}$$

where α and α_{bA-S} are the fiber attenuation at the launched and backscattered wavelengths respectively, $\eta_{A-S}(z,T)$ is the effective quantum efficiency of the anti-Stokes process (defined as the ratio of Raman anti-Stokes signal generated to the power lost from the forward-traveling pulse in a scattering region at temperature T and distance z), v_g is the group velocity of the optical guide and S is the backscatter capture ratio, which for a homogeneous step index fiber is given by [4]

$$S_{SM}=\frac{3}{8\pi^2}\left[\frac{\lambda}{n_{co}w}\right]^2 \tag{5.3}$$

λ being the optical wavelength of the backscattered light, n_{co} the refractive index of the fiber core and w the fibre $1/e^2$ intensity spotsize at the backscattered wavelength. For multimode step-index fibres S is given by [4]

$$S_{MM}=\eta\left[\frac{NA}{n_{co}}\right]^2 \tag{5.4}$$

where η is a function of the power distribution of the backscattered power. For a uniform power distribution $\eta=3/8$. Fig.5.1 plots the ratio S_{MM}/S_{SM} against the single-mode fibre V-value for the case of equal single-mode and multimode fibre NA's. If the NA's are unequal, the value of S_{MM}/S_{SM} from the graph at a particular V-value should be multiplied by the square of the ratio NA_{MM}/NA_{SM}. Setting the following values into eqn.(5.2) $\eta_{A\text{-}S}=0.001$, $\alpha=\alpha_{bA\text{-}S}=10^{-6}$ cm^{-1} (~0.4dB/km), $S=0.001$, $v_g=2\times10^{10}$ cm/s, L=500m, we obtain $P_{A\text{-}S}(L)=18$ pW for a 1 nJ pulse. At room temperature, the Stokes signal is 4 times stronger.

A 1-10km long low-loss mode-locked fiber laser configuration which produces 1-10ns, 10W pulses at repetition rates of 10-100kHz could then be developed to offer an attractive alternative to the current Q-switch source/passive fibre DTS approach. In fact, by using a low loss fibre laser cavity, intracavity pulse energies in excess of 200nJ should be possible at modest (<150mW) pump powers. This offers a significant advantage in terms of power efficiency over the existing system which uses each probing pulse only once. By using wavelength selective couplers, the Raman Stokes and anti-Stokes signals could be routed out of the cavity and detected whilst the lasing wavelength is maintained inside. Consequently, and in combination with the relatively high repetition rates, the averaging time needed to obtain sufficient data would be significantly reduced. However, the onset of stimulated Raman scattering, typically a few Watts for a 1 km silica core single-mode fiber cavity at 1.55μm [5], will impose a maximum limit to the pulse power that can be used, although owing to the pulse walk-off effect the Raman threshold for nanosecond pulses is expected to be greater, typically 10-15W.

5.3 EXPERIMENTAL RESULTS ON ACTIVELY MODE-LOCKED SYSTEMS

This section presents experimental results on two types of fibre laser cavity

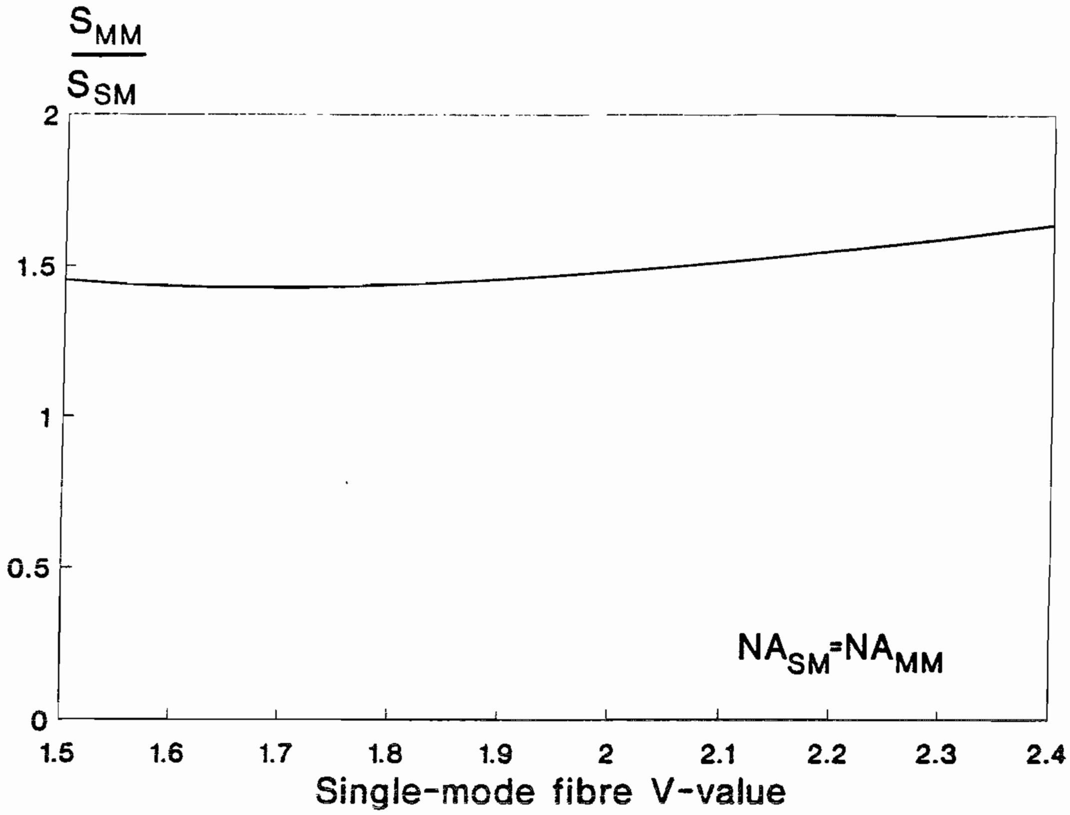

Fig.5.1 Ratio of S_{MM}/S_{SM} against single-mode fibre V-value.

configurations, namely Fabry-Perot and antiresonant ring (Sagnac) lasers. Active mode-locking techniques were pursued using amplitude and phase modulators with an aim to find the most suitable arrangement for a DTS system.

5.3.1 Fabry-Perot AM Mode-Locking Using an Acousto-Optic Modulator

The experimental arrangement is shown in Fig.5.2a. 5m of Nd^{3+}-doped fiber (dopant concentration=190ppm, NA=0.2, cut-off wavelength=790nm) were spliced onto 500m of low-loss (<1.5 dB/km) undoped fiber, (NA=0.16, cut-off wavelength 960nm). The Bragg cell modulator (IntraAction Corp. Model AOM-40R) had an acoustic carrier frequency of 40 MHz with a modulation bandwidth of 2.9-4.5 MHz (depending on the input beam diameter) and was anti-reflection coated at the lasing wavelength of 1.08μm. The diffraction efficiency was measured to be 80% at the modulating frequency of 200 kHz. The intracavity lens (Newport KPX010) was an anti-reflection coated planoconvex lens positioned with its flat surface facing the fiber so as to minimise spherical aberration. The end of the passive fiber was also polished at an angle to prevent etalon formation.

The laser had a pump threshold of 80mW and a slope efficiency of ~5%. The carrier frequency was modulated using square and sinusoidal signals, with the former producing 20ns mode-locked pulses and the latter producing 35ns pulses. Since these pulses were far from being bandwidth-limited, the grating arrangement shown in Fig.5.2b was subsequently used. Although this arrangement caused a reduction of the lasing linewidth to 0.15nm, no pulse shortening was observed.

5.3.2 Sagnac Loop AM Mode-Locking Using a Piezoelectric Cylinder

Another method to produce AM mode-locking using an FM modulator is to use the arrangement of Fig.5.3. The phase difference of the two counter-propagating fields in the Sagnac loop previously provided by birefringence and/or non-linear effects, as discussed in Chapter 3, is instead now produced using a phase modulator positioned on one arm of the loop. This phase modulation actually mode-locks the Sagnac laser by means of amplitude modulation.

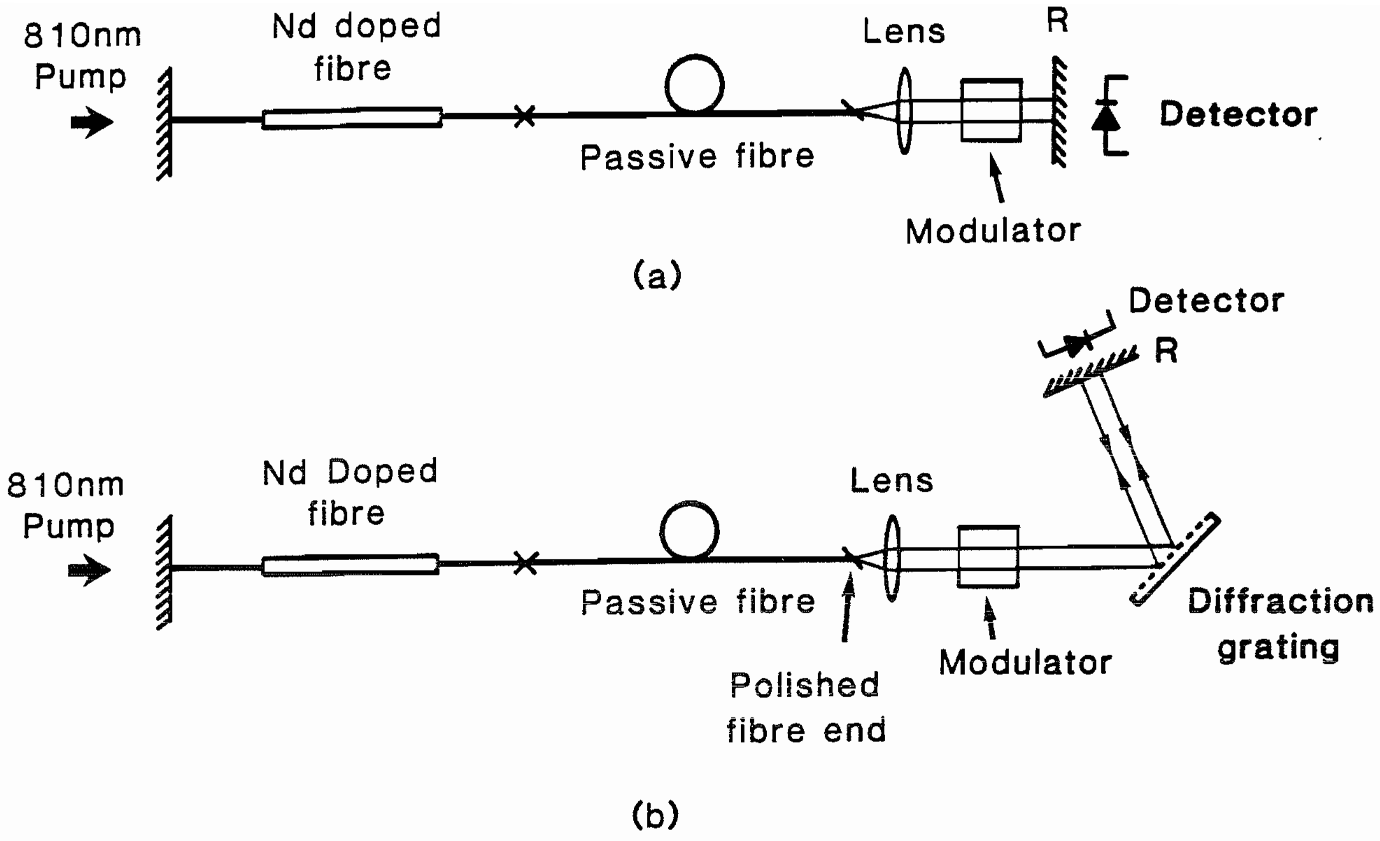

Fig.5.2 The experimental arrangements for AM mode-locking using an acousto-optic modulator (Sec.5.3.1).

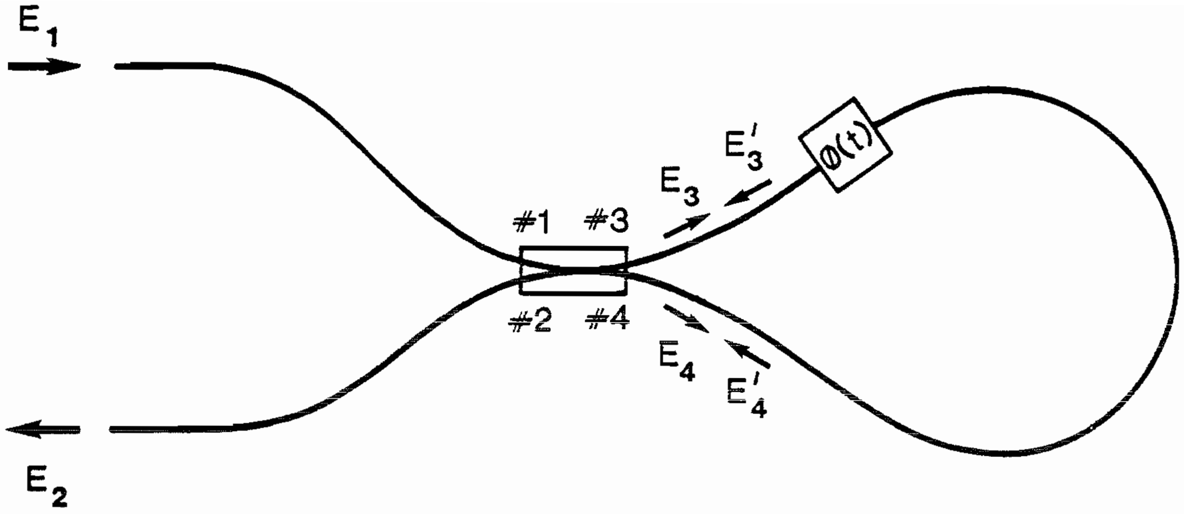

Fig.5.3 Action of phase modulator in the Sagnac loop.

We can write for the fields E'$_3$ and E'$_4$:

$$E_4'(t)=\alpha^{1/2}E_1(t-T)e^{j[\beta L+\phi(t-T)]}$$
$$E_3'(t)=j(1-\alpha)^{1/2}E_1(t-T)e^{j[\beta L+\phi(t)]} \tag{5.5}$$

where

$$\phi(t)=\delta\cos(\omega_m t) \tag{5.6}$$

The transmission function becomes

$$\mathrm{T}_{AM}(t)=1-4\alpha(1-\alpha)\cos^2\left[\frac{\phi(t)-\phi(t-T)}{2}\right] \tag{5.7}$$

For low modulation indices $\cos^2(x)\approx 1-x^2$ and the transmission function can be written as

$$T_{AM}(t)\approx\delta^2\sin^2\left[\omega_m\left(t-\frac{T}{2}\right)\right]\ \sin^2\left(\frac{\omega_m T}{2}\right)\qquad (for\ \alpha=0.5) \tag{5.8}$$

Because of the $\sin^2(\omega_m T/2)$ factor in the transmission function, the length of the whole cavity should be made as close as possible to the loop length. Note also that the amplitude modulation frequency is twice the phase modulation frequency that produces it.

Fig.5.4 shows the experimental set-up. The modulator used was a piezoelectric cylinder (Vernitron PZT 5H 32-16125) with an outer diameter of 25.4mm, a wall thickness of 3.18mm and length 50.8mm. The modulation efficiency of the device at 1.1 MHz was measured by setting up a Mach-Zender interferometer and was found to be 0.1 radians per volt per meter at a wavelength of 632.8nm. A length of ~80m was used to form the Sagnac loop for fundamental mode-locking. This was composed of ~35m of a low doped erbium doped fiber spliced with 45m of undoped fiber, both single mode at the lasing wavelength of 1.55μ. Almost all of the 35m of the doped section was wound on the cylinder.

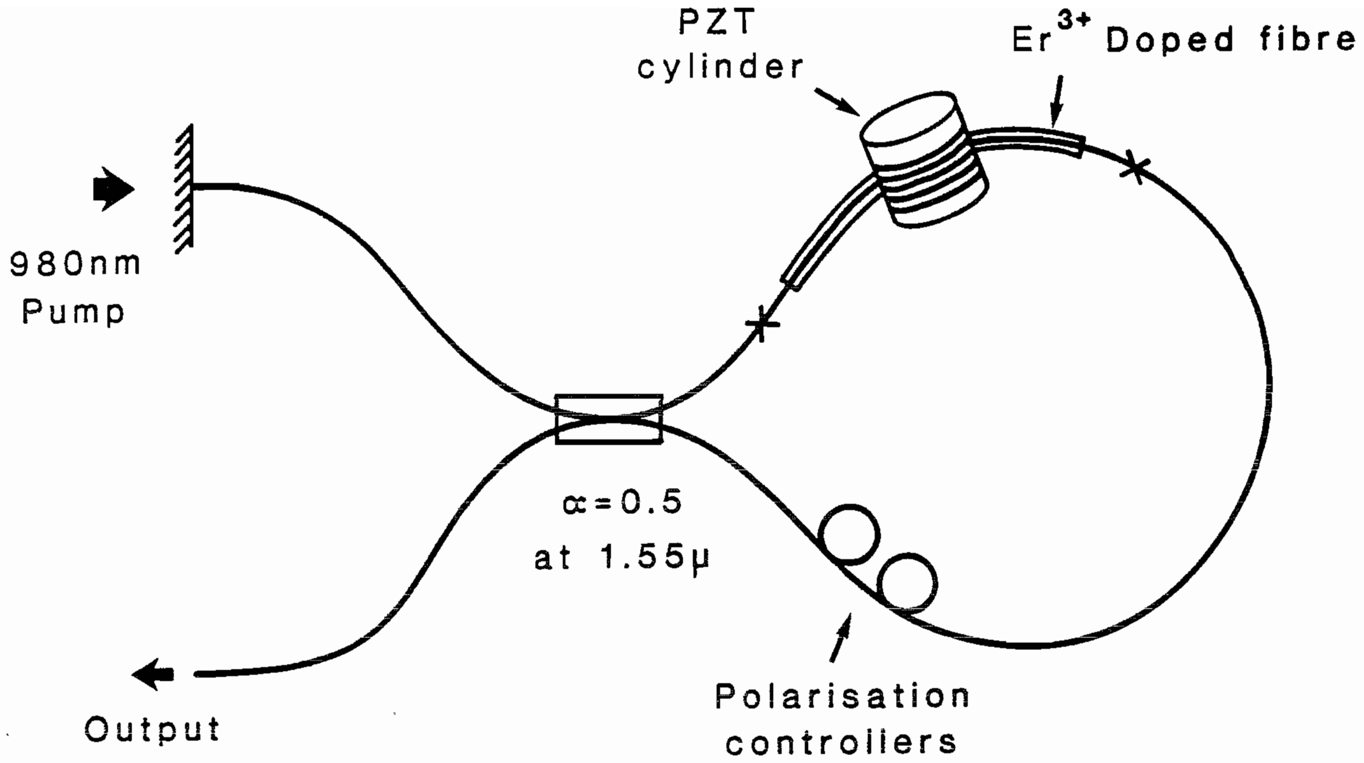

Fig.5.4 Experimental arrangement for AM mode-locking using a piezoelectric cylinder.

When the modulator was switched on, mode-locking of the laser was achieved. The pulses observed had a 5ns envelope with a 300ps substructure (see Fig.5.5) which was probably caused by an excessive modulation index.

5.3.3 Fabry-Perot FM Mode-Locking Using a Piezoelectric Cylinder

In this experiment the same piezoelectric cylinder as described in the previous experiment was used to provide phase modulation of a Fabry-Perot cavity. The experimental arrangement is shown in Fig.5.6. 30m of a low-doped Er-doped fiber was spliced onto 70m of passive fiber. As the phase modulation efficiency of the cylinder was small, even when used at its thickness resonance frequency, almost all of the Er-doped fiber was wound onto it. When a sinusoidal voltage of 40Vp-p at the round trip frequency (1.1 MHz) was applied to the piezo, mode-locking produced a pulsewidth of 7ns. In Fig.5.7 the cw and mode-locked linewidths are shown. It was also observed that the noisy cw spectrum became quieter when the phase modulator was on, irrespectively of the applied frequency (see Fig.5.8). This effect has recently been used for noise suppression in a harmonically mode-locked fibre ring laser [6], with successfull results. Similar experiments using a Nd-doped fibre in a 1km cavity produced pulsewidths ~85ns.

5.4 KUIZENGA-SIEGMAN THEORY

These preliminary attempts at actively mode-locking long fibre lasers failed to achieve the desired pulse durations of ~1-10ns required for a spatial resolution of ~0.1-1m, assuming a cavity length of ~1km. In order to assess the effect of the various parameters on the mode-locking performance of the fibre laser configurations that were presented in the previous section, it is neccessary to use an extended version of the Kuizenga-Siegman (K-S) theory of active mode-locking. Kuizenga and Siegman developed a model in order to predict the pulsewidth and bandwidth of a Gaussian pulse formed in a mode-locked laser with a homogeneously broadened linewidth using either an amplitude (AM) or a phase (FM) modulator. The solution is based on finding a Gaussian pulse, the real and imaginary parts of which transform self-consistently after one round trip inside the laser cavity:

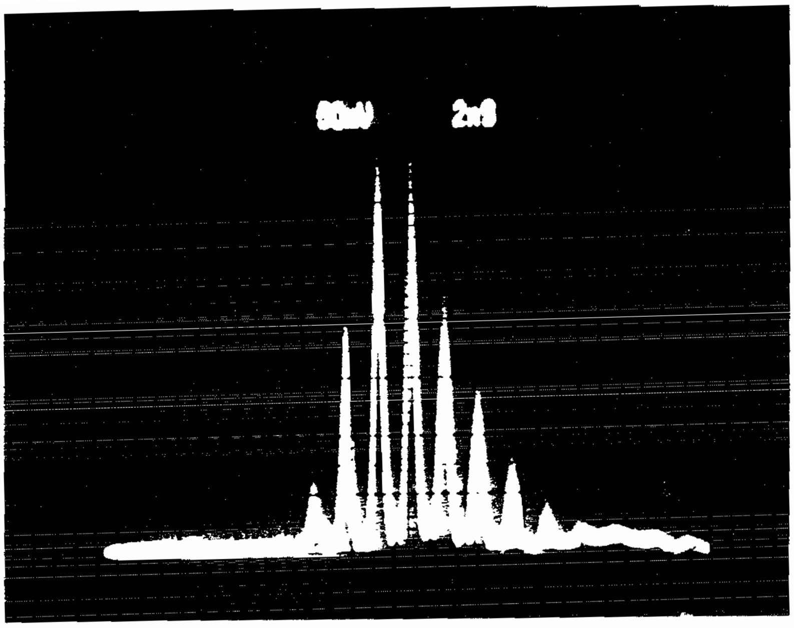

Fig.5.5 Mode-locked pulse obtained with the arrangement of Fig.5.4

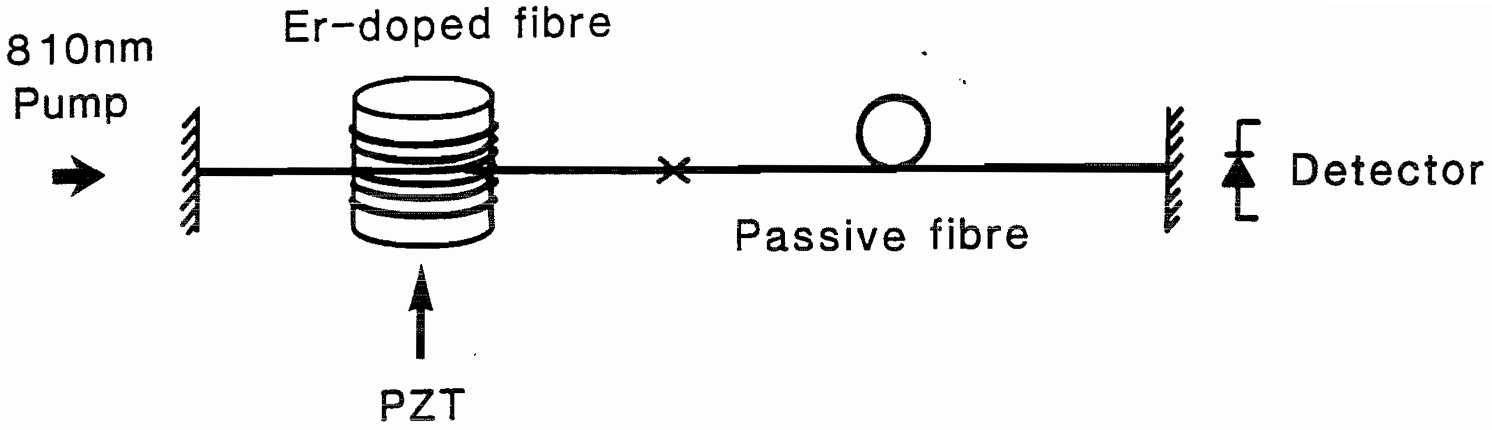

Fig.5.6 Experimental arrangement for FM mode-locking using a piezoelectric cylinder (Sec.5.3.3).

Fig.5.7 Pulsewidth and optical spectrum produced with the arrangement of Fig.5.6.

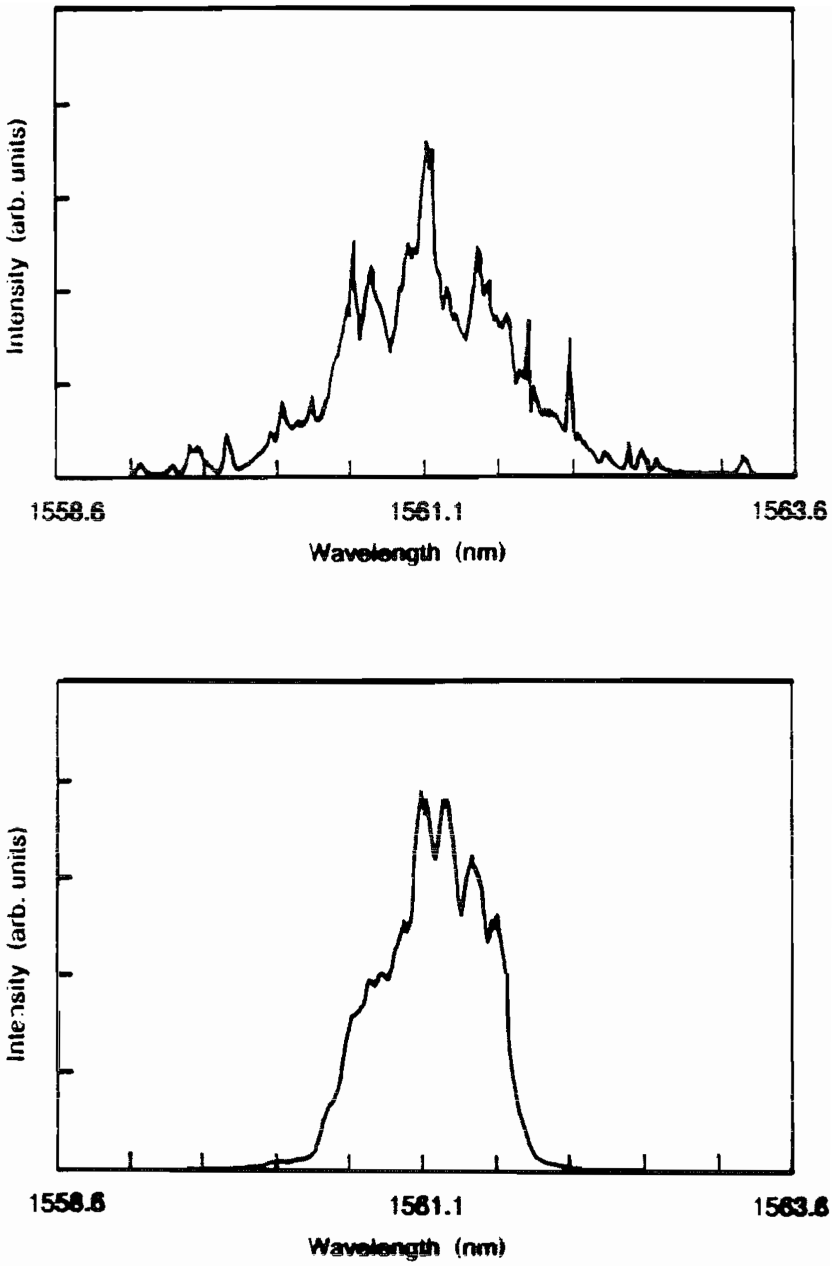

Fig.5.8 Lasing linewidths of the laser in Fig.5.6 (a) free-running and (b) free-running but with applied phase modulation much lower than the round trip frequency.

$$E(t) \xrightarrow{gainmedium} E(t+t_1) \xrightarrow{modulator} E(t+t_2) \xrightarrow{otherelements} \ldots \dashrightarrow E(t+t_n)=E(t) \qquad (5.9)$$

where

$E(t)=E_0 \exp\{-\Gamma t^2\} \exp\{i\omega_p t\}$;

$\Gamma=\alpha-i\beta$

ω_p=carrier frequency of the pulse and

$t_n=T_{rt}$=cavity round-trip time.

The pulsewidth and bandwidth of the Gaussian pulse in terms of α and β are given by

$$\tau=\left[\frac{2\ln 2}{\alpha}\right]^{\frac{1}{2}} \qquad (5.10)$$

$$\Delta f=\frac{(2\ln 2)^{\frac{1}{2}}}{\pi}\left[\frac{\alpha^2+\beta^2}{\alpha}\right]^{\frac{1}{2}} \qquad (5.11)$$

Eqn.(5.9) may be expressed mathematically as

$$E_4(t)=E_1(t-T_{rt})e^{-i\phi} \qquad (5.12)$$

with

$E_4(t)=rE_3(t-2L_c/c)$

$E_3(t)=E_2(t)\ T(t-t_g)$

$E_2(\omega)=G(\omega)\ E(\omega)$

where r is the field amplitude reflectivity of the output mirror, $G(\omega)$ is the double pass amplitude gain transfer function of the amplifying medium, T(t) is the modulator transmission function (amplitude or phase) and t_g, $2L_c/c$ allow for delays of the pulse envelope from the passage through the gain medium and the passive optical cavity length L_c respectively.

The theory assumes that the Gaussian pulse remains Gaussian after one round trip, and eqn.(5.12) is reduced to an equation for Γ:

$$\Gamma_{round\,trip}=\Gamma_{initial} \tag{5.13}$$

Refering to Fig.5.9, this corresponds to

$$\Gamma_{AM or FM\ modulator}=\Gamma_{initial} \tag{5.14}$$

where

$$\begin{aligned}\Gamma_{AM\,modulator}&=\Gamma_{gain\,medium}+\frac{\delta_t\omega_m^2}{2}\\ \Gamma_{FM\,modulator}&=\Gamma_{gain\,medium}+\frac{j\delta_c\omega_m^2}{2}\end{aligned} \tag{5.15}$$

and

$$\Gamma_{gain\,medium}=\Gamma_{initial}-\frac{8\ln G_0}{\Delta\omega^2}\Gamma_{initial}^2 \tag{5.16}$$

where G_0 is the double pass intensity gain through the active medium, δ_t is defined by the transmission function of the amplitude modulator $m(t)=\exp\{-\delta_t(1-\cos\omega_m t)\}$ and $2\delta_c$ is the peak-to-peak phase deviation through the phase modulator. By substituting eqns.(5.15) and (5.16) into eqn.(5.14), a quadratic equation for Γ is obtained which can be solved easily to give us the steady-state values of α and β.

The next two sections will investigate the effect of the intracavity fibre dispersion on the standard formulas for the mode-locked pulsewidth in both the AM and FM mode-locking cases.

5.4.1 AM Mode-Locking

When using an amplitude modulator, the α and β parameters predicted by the theory are

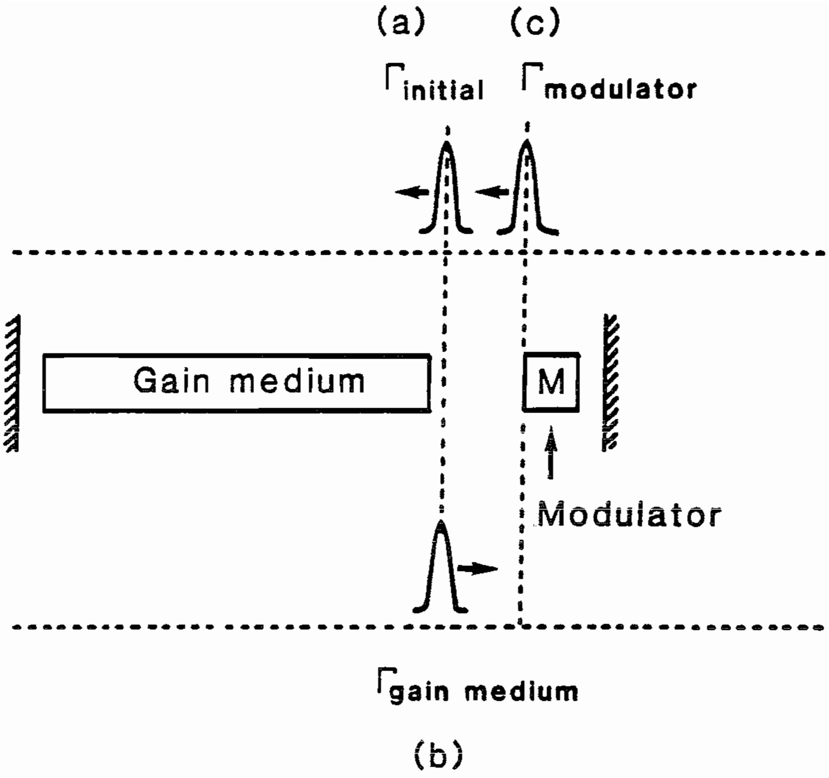

Fig.5.9 The transformation of Γ for one cavity round trip: (a) pulse entering the gain medium section of the cavity, (b) pulse entering the modulator section and (c) pulse has completed one round trip.

$$\alpha_0^{AM}=\left[\frac{\omega_m\Delta\omega}{4}\right]\sqrt{\frac{\delta_t}{2g}} \qquad \beta_0^{AM}=0 \tag{5.17}$$

which correspond to a pulsewidth of

$$\tau_0(AM)=\frac{\sqrt{2\sqrt{2}\ln 2}}{\pi}\left[\frac{g}{\delta_t}\right]^{1/4}\left[\frac{1}{f_m\Delta f}\right]^{1/2} \tag{5.18}$$

with bandwidth

$$\Delta f_0^{AM}=\frac{2\ln 2}{\pi\tau_0^{AM}} \tag{5.19}$$

where g is the double pass saturated amplitude gain coefficient, f_m is the modulation frequency and $\Delta\omega=2\pi\Delta f$ is the gain bandwidth.

The pulsewidth-bandwidth product is thus 0.44 (the pulse is bandwidth-limited). Fig.5.10(a) shows how this pulse transforms in the complex plane for one round trip. The gain and the amplitude modulator actions have been exaggerated for clarity.

The model can be easily modified to include dispersion effects which become significant in long fiber laser cavities. Following the same method that lead to the derivation of eqns.(5.18) and (5.19) [1], but using a Taylor expansion up to second order terms for the propagation constant of the material comprising the gain medium, it can be shown (see Appendix to Ch.5) that the predicted pulsewidth, τ_D(AM) with the inclusion of GVD in a laser cavity of length L is given by

$$\tau_D(AM)=\tau_0(AM)\frac{\left(1+\Delta^2\right)^{1/8}}{\sqrt{\cos\frac{\theta}{2}}} \tag{5.20}$$

where

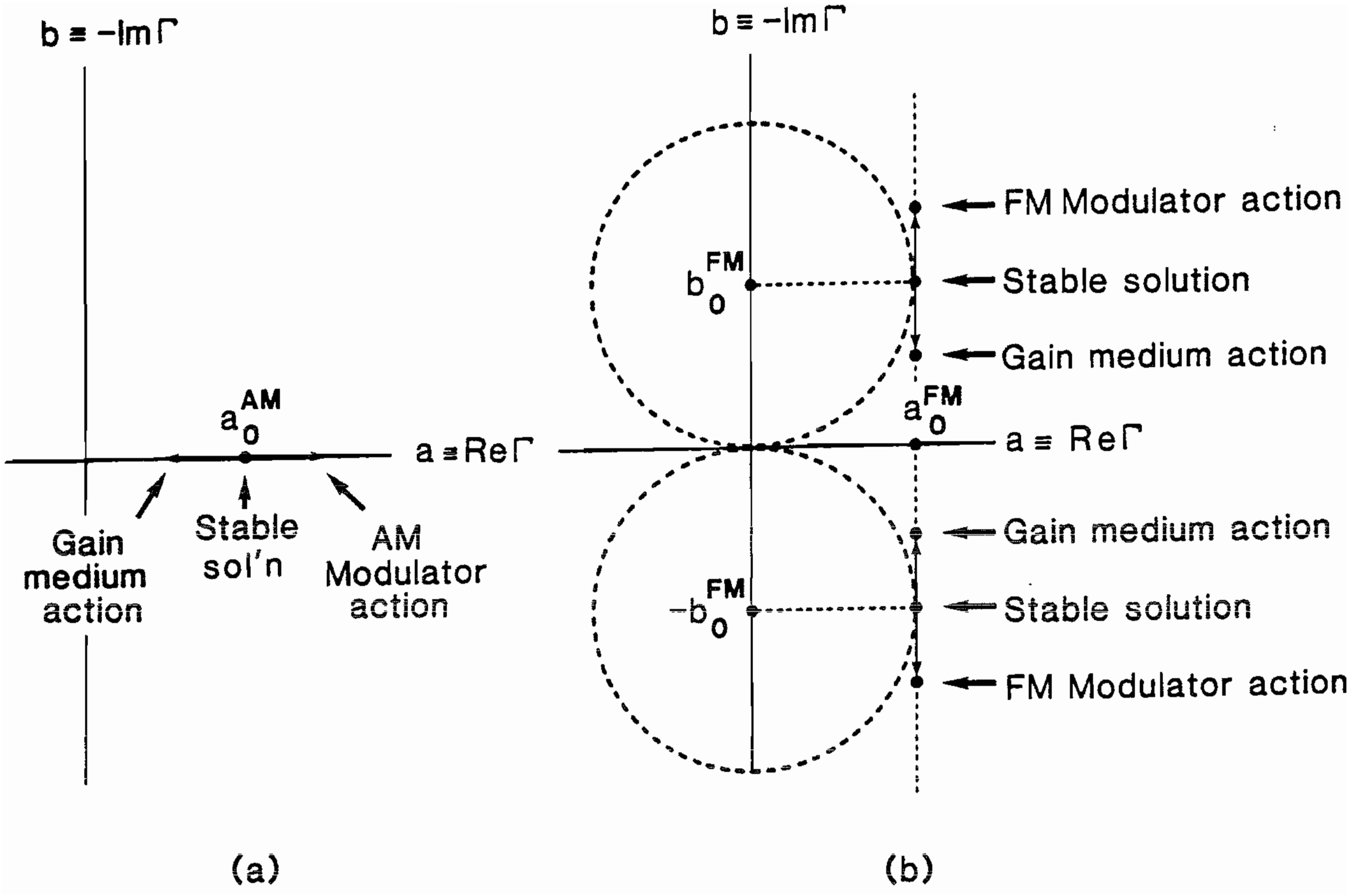

Fig.5.10 The transformation of Γ for one cavity round trip in the complex plane: (a) refers to AM mode-locking and (b) to FM mode-locking. The stable solution in the AM case is a Gaussian pulse with no imaginary part (bandwidth limited) whereas in the FM case the pulse has equal real and imaginary parts.

$$\Delta = \frac{\beta_2 L \Delta\omega^2}{4g} \qquad (5.21)$$

$$\beta_2 = \frac{\lambda^3}{2\pi c^2}\left[\frac{\partial^2 n}{\partial\lambda^2}\right] \qquad (5.22)$$

$$\theta = \tan^{-1}(-\Delta) \qquad (5.23)$$

and the bandwidth by

$$\Delta f_D^{AM} = \Delta f_0^{AM}\frac{\left(1+\Delta^2\right)^{-1/8}}{\sqrt{\cos\frac{\theta}{2}}} \qquad (5.24)$$

These give a pulsewidth-bandwidth product of $\frac{0.44}{\cos(\theta/2)}$.

The important thing to note is that for values of $\Delta > 1$ the pulsewidth becomes essentially independent of $\Delta\omega$; the $(\Delta\omega)^{-1/2}$ initial dependance of τ_0^{AM} is cancelled by the strong Δ term in eqn.(5.20). Fig.5.11(a,b) shows how τ/τ_0^{AM} and $\Delta f_D^{AM}/\Delta f_0^{AM}$ vary with Δ and Fig.5.12 shows a z plot of the pulse's real and imaginary parts (normalised to α_0^{AM}) as a function of Δ.

5.4.2 FM Mode-Locking

For a phase modulator, the real and imaginary parts of the steady-state Gaussian pulse are

$$\alpha_0^{FM} = \beta_0^{FM} = \left[\frac{\omega_m \Delta\omega}{8}\right]\sqrt{\frac{\delta_c}{g}} \qquad (5.25)$$

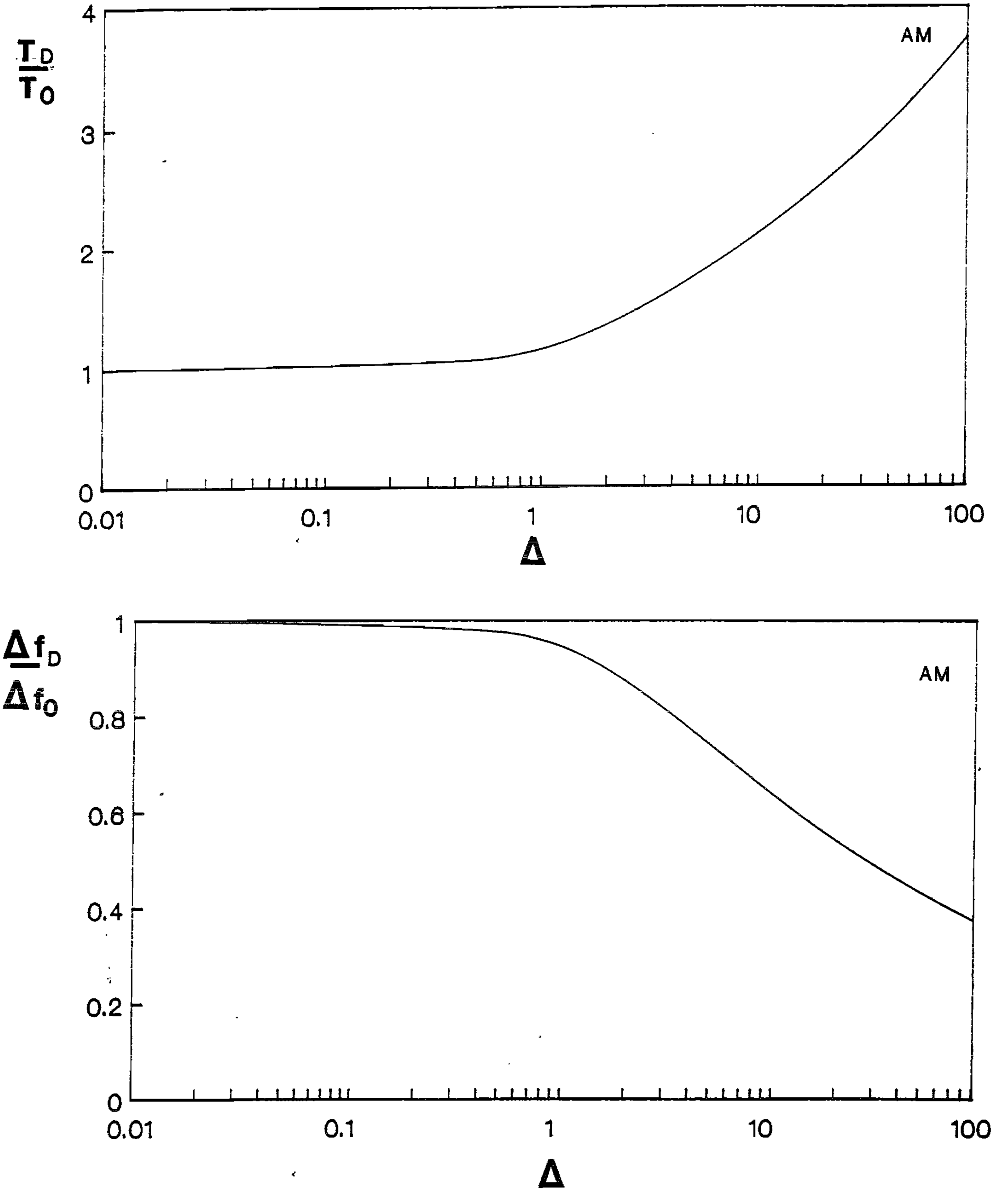

Fig.5.11 The variation of the ratio of the pulsewidth (a) and bandwidth (b) of the AM mode-locked pulses in a dispersive medium with respect to their zero dispersion values as a function of the dispersion parameter Δ.

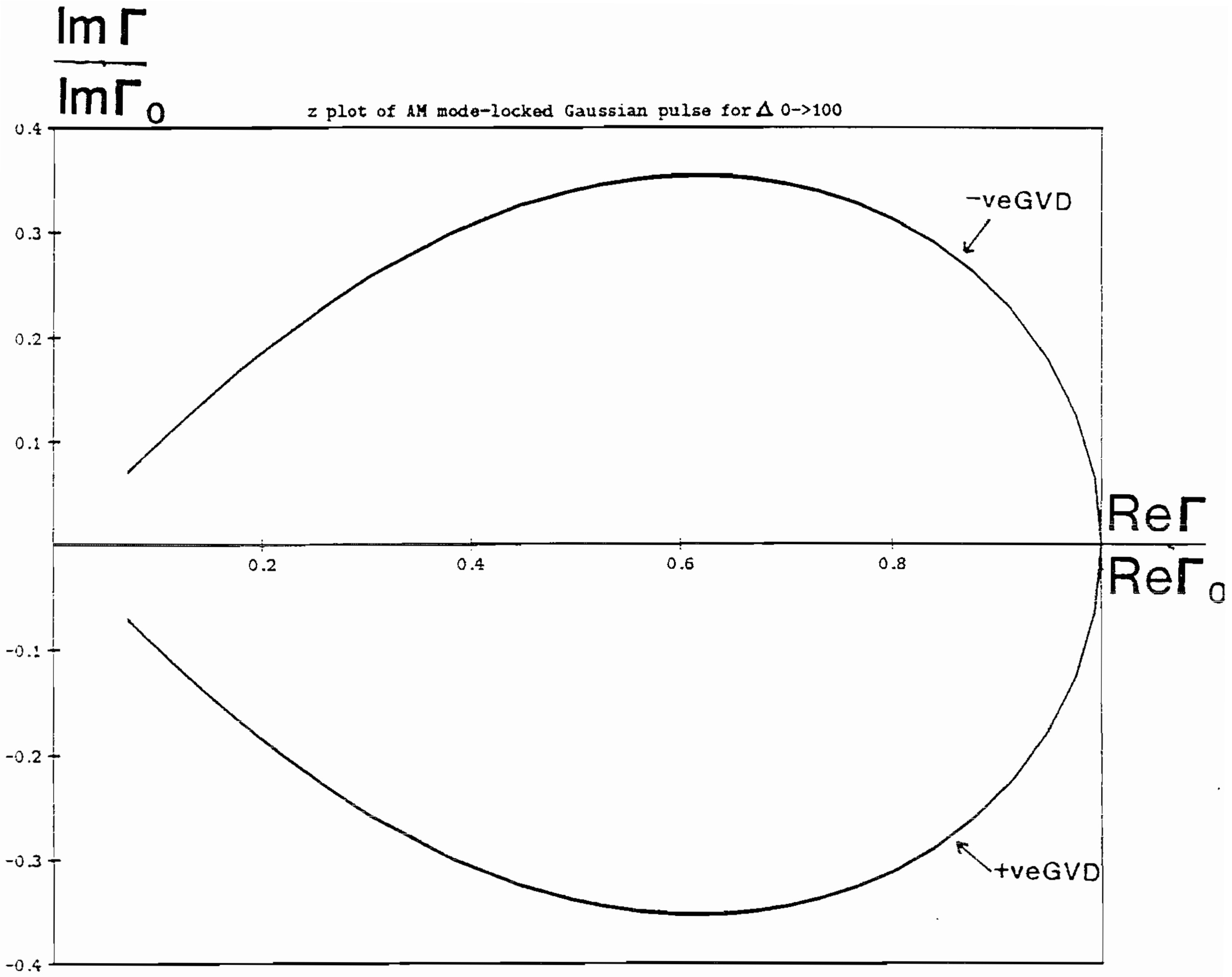

Fig.5.12 The variation shown in Fig.5.11 as viewed in the complex plane.

but now β can be either positive, corresponding to a pulse having a positive chirp and passing through the phase modulator at the maximum of the phase variation, or negative, corresponding to a pulse having a negative chirp and passing through the phase modulator at the minimum phase variation point. Hence there are two stable mode-locked pulses inside the cavity of equal pulsewidths but different phase chirps. Fig.5.13 illustrates the action of the phase modulator on the positively chirped pulse. The tangents on the left and on the right of the peak phase variation point have been drawn quite far apart from it for the sake of clarity. It can be seen that the front, low frequency part of the pulse (in space) gets downshifted, the rear, higher frequency part gets upshifted, while the centre of the pulse experiences no Doppler shift at all. The overall result is an increase in the pulse's bandwidth. The same increase happens with the negatively chirped pulse.

The predicted pulsewidth and bandwidth are

$$\tau_0(FM) = \frac{2\sqrt{\ln 2}}{\pi}\left[\frac{g}{\delta_c}\right]^{1/4}\left[\frac{1}{f_m \Delta f}\right]^{1/2} \tag{5.26}$$

$$\Delta f_0^{FM} = \frac{2\sqrt{2}\,\ln 2}{\pi \tau_0^{FM}} \tag{5.27}$$

Fig.5.10(b) shows the pulses' tranformations for one round trip on the complex plane. The action of the modulator and the gain medium have, as in the AM case, been exaggerated for clarity. It can be seen that the action of the gain medium is to decrease the bandwidth of the pulse by an amount equal and opposite to the increase due to the action of the FM modulator. Therefore, no pulsewidth shaping occurs at steady-state FM mode locking, since α remains constant. In contrast, the action of the gain medium in the AM case is to cause pulse broadening without any change in its bandwidth. This counter-balances the action of the amplitude loss modulator which sharpens the pulse by "cutting" its edges. The gain medium therefore acts differently in each case. In fact, these are two special cases; in general a gain medium acts to alter both of the α and β parameters of the pulse.

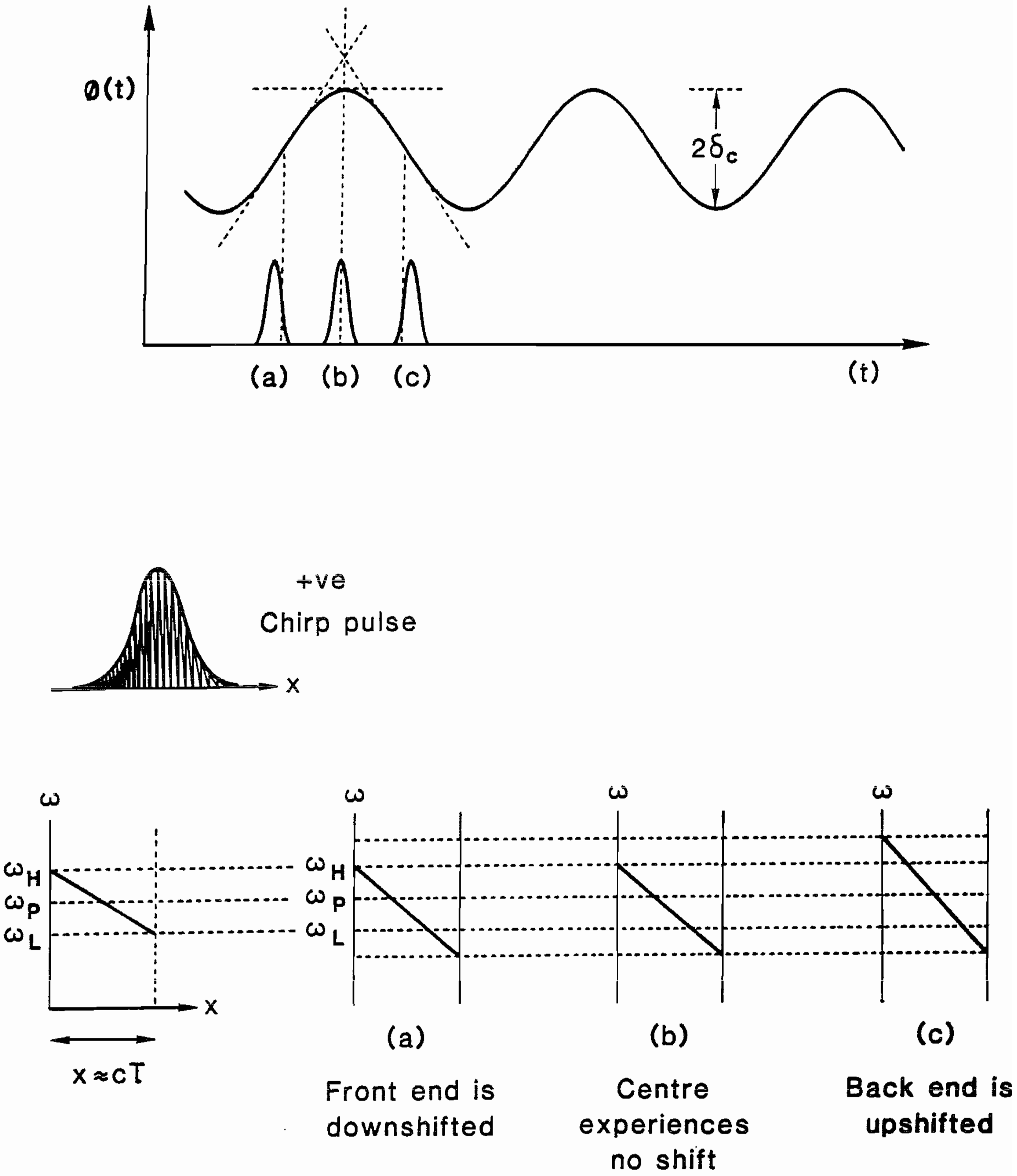

Fig.5.13 The action of a phase modulator on a positively chirped pulse. x refers to the length of a pulse with duration τ and ω_H, ω_L to the high and low frequency parts of its spectrum. The action of the modulator is seen to increase the pulse's bandwidth.

If dispersion effects are taken into account it is found that the degeneracy between the two pulses is lifted (see Appendix to Ch.5). Dispersion discriminates between the two pulses and the predicted pulsewidths are

$$\tau_D^-(FM)=\tau_0(FM)\frac{\left(1+\Delta^2\right)^{1/8}}{\sqrt{\sqrt{2}\cos\frac{\theta'}{2}}} \tag{5.28}$$

$$\tau_D^+(FM)=\tau_0(FM)\frac{\left(1+\Delta^2\right)^{1/8}}{\sqrt{\sqrt{2}\sin\frac{\theta'}{2}}} \tag{5.29}$$

where

$$\theta'=\tan^{-1}\left[\frac{1}{\Delta}\right] \tag{5.30}$$

The - and + superscripts indicate the sign of the chirp that the pulses had originally and correspond to $\delta_g=+j\delta_c$ and $-j\delta_c$ respectively (see Appendix to Ch.5). Fig.5.14(a) shows how $\tau^{(-,+)}/\tau_0$ vary with Δ: the pulse with the negative chirp is shortened slightly before it starts broadening whereas the pulse with the positive chirp broadens immediately and much more rapidly. The reverse happens when β_2 is negative. Fig.5.14(b) shows how the bandwidth ratios $\Delta f^{(-,+)}/\Delta f_0$ change with respect to the dispersion parameter Δ and Figs.5.15(a-d) show the location of these pulses on the complex plane with respect to their zero dispersion values as a function of this parameter. The formulas for the new bandwidths are

$$\Delta f_{D-}^{FM}=\Delta f_0^{FM}\sqrt{\frac{\sqrt{2}}{2}}\,\frac{\left(1+\Delta^2\right)^{-1/8}}{\sqrt{\cos\frac{\theta'}{2}}} \tag{5.31}$$

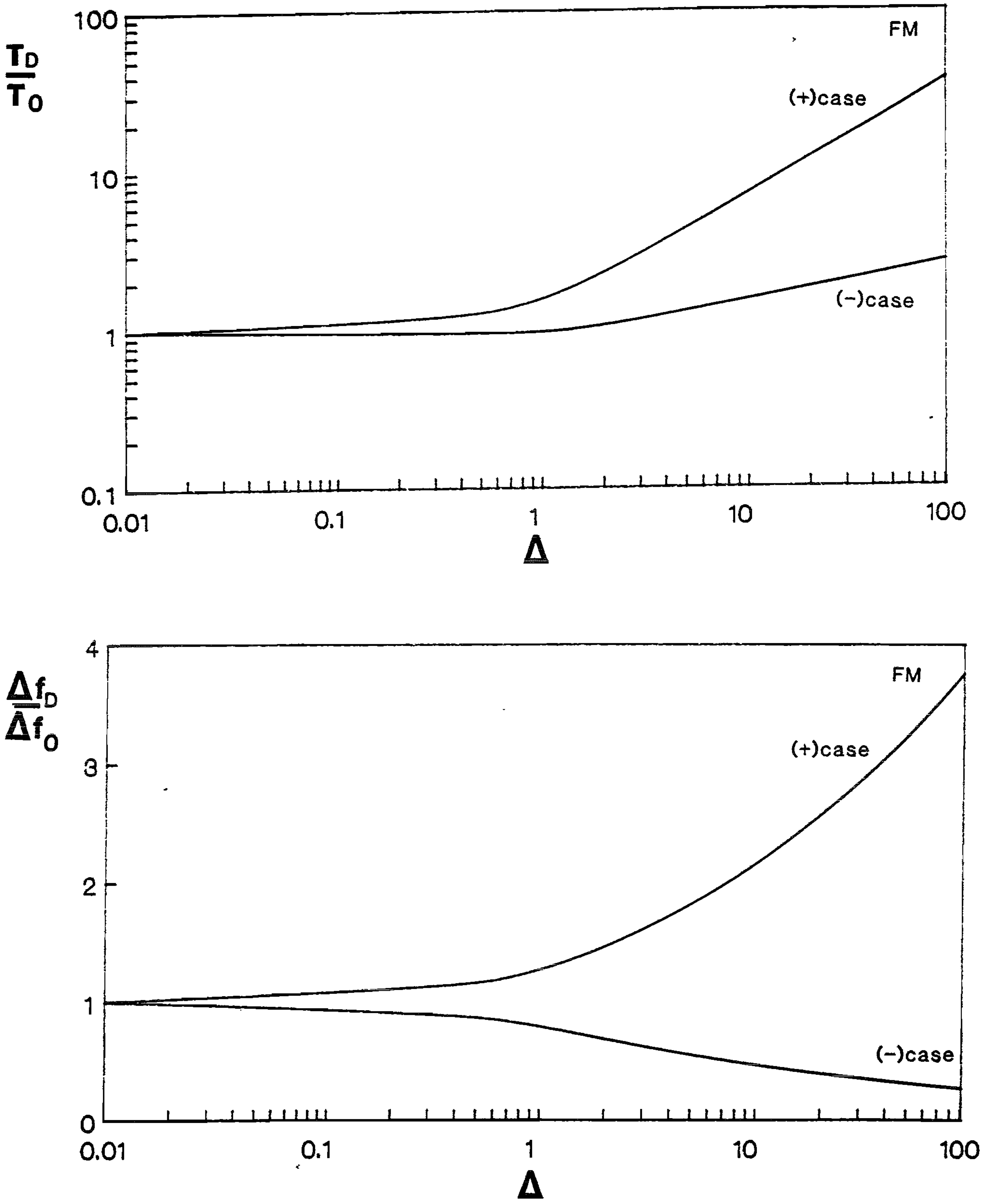

Fig.5.14 The variation of the ratio of the pulsewidth (a) and bandwidth (b) of the two FM mode-locked pulses in a dispersive medium with respect to their zero dispersion values as a function of the dispersion parameter Δ.

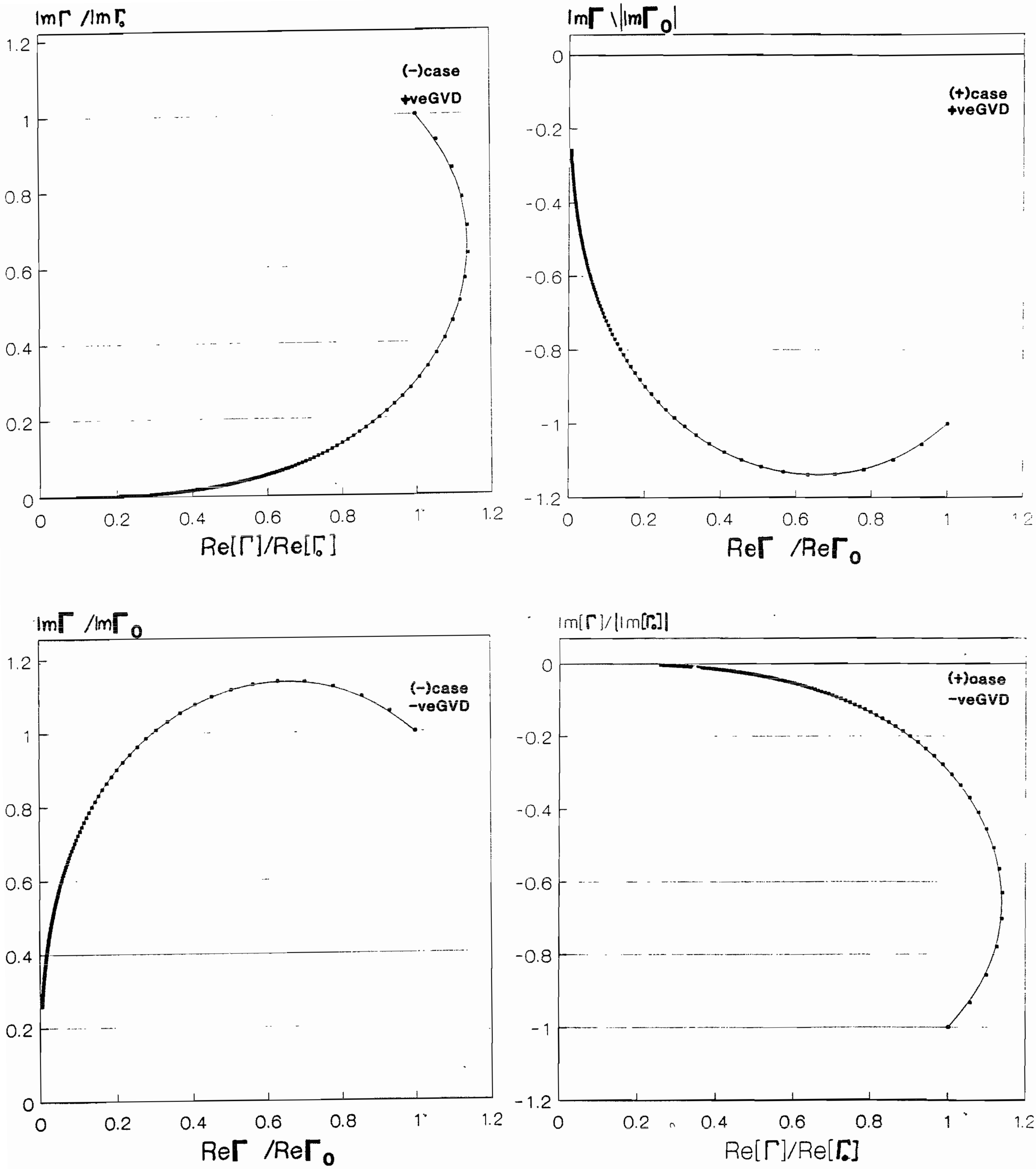

Fig.5.15 The variation shown in Fig.5.14 as viewed in the complex plane.

$$\Delta f_{D+}^{FM} = \Delta f_0^{FM} \sqrt{\frac{\sqrt{2}}{2} \frac{\left(1+\Delta^2\right)^{-1/8}}{\sqrt{\sin\frac{\theta'}{2}}}} \tag{5.32}$$

and the pulsewidth-bandwidth products are $\dfrac{0.624}{\sqrt{2}\cos\frac{\theta'}{2}}$ and $\dfrac{0.624}{\sqrt{2}\sin\frac{\theta'}{2}}$ respectively.

5.4.3 Result Interpretation

Using the formulas presented in the previous section, with the values $\beta_2=1.73\ 10^{-26}\ s^2/m$ (D=-27 ps/(nm km)) for the Nd^{3+} system and $\beta_2=-1.91\ 10^{-26}\ s^2/m$ (D=15 ps/(nm km)) for the Er^{3+} system and, accordingly, L(Nd)=500 m, L(Er)=100 m, g(Nd,Er)=0.34 for $R_{eff}=0.5$, $\Delta f(Nd)=10$ THz, $\Delta f(Er)=7.5$ THz, $f_m(Nd)=200$ kHz, $f_m(Er)=1$ MHz, $\delta_t(Nd)=0.4$, $\delta_c(Er)=1$ the expected values for the pulse durations are $\tau(Nd)=3.2$ns, $\tau(Er)=745$ps with corresponding bandwidths $\Delta f(Nd)=200$ MHz and $\Delta f(Er)=600$ MHz.

The experimental results therefore differ by a factor of ~10 from the theoretical predictions for both experiments. However, one must bear in mind that the Kuizenga-Siegman theory assumes a homogeneously broadened linewidth which ensures near-bandwidth-limited operation. In order to be able to make comparisons between the theory and the experiment, the oscillating linewidth should be reduced to that required for bandwidth-limited operation, otherwise the excessive osillating linewidth may result in imperfect mode-locking. In an imperfectly mode-locked laser, the lasing linewidth consists of several groups or "domains" having perfect internal phasing but random phases relative to other domains [7]. As was shown in the previous section, the pulsewidth becomes essentially independent of the gain bandwidth for values of $\Delta > 1$, having assumed that perfect mode-locking takes place. However, when the mode locking is imperfect due to excessive gain bandwidth and with the modes locked in "domains", reducing the osillating linewidth should result in the reduction of these domains and hence be a possible means for reducing the pulsewidth. Experimentally it was found that reducing the linewidth from 7nm to 0.15nm produced no pulsewidth shortening, however it may be argued than a linewidth of 0.15 nm (38 GHz) is still two orders of magnitude greater than the bandwidth-limited value of 200 MHz.

A plausible explanation for the discrepancy between the experimental results and the predictions of K-S theory, even with the linewidth reduced to the bandwith-limited value, is found by looking at the estimate of the time constant T_{ss}, which indicates the time needed for the pulsewidth to be within ~20% of its final, steady state value. For an AM mode-locked system T_{ss} is given by [8]:

$$T_{ss}=\left(\frac{1}{8g\delta_t}\right)^{\frac{1}{2}}\frac{\Delta\nu}{f_m^2} \tag{5.33}$$

which, for the Nd-doped system described previously, has a value of ~4 min! This is much larger than the mutual mode-coherence time of the laser and so the pulsewidth will never reach its steady state value.

5.5 EXPERIMENTAL RESULTS ON A PASSIVELY MODE-LOCKED SYSTEM

Since it proved difficult to produce short (~1-10ns) pulses by active mode-locking for cavity lengths close to ~1km, the passive mode-locking method based on NLPE (see previous Chapter) was tried next. The experimental set-up is depicted in Fig.5.16. The pump source was an argon-ion pumped Ti:sapphire laser providing up to 3W of cw light at 980nm to pump the erbium doped fibre (Er concentration 800ppm, NA=0.15 and cut-off wavelength λ_c=960nm) through a 980/1550 wavelength division multiplexing (WDM) coupler. A small amount of 980nm light from the remaining output port of the WDM was fed back to an active stabilisation circuit, which by means of a Bragg cell compensates for any variations in the pump power. The cavity comprised of 4 m of the erbium-doped fibre, two reels of standard telecom fibre (NA=0.11, λ_c=1200nm) of lengths 1km and 3km each, a fibre optical polarising isolator (BT&D Technology), two sets of polarisation

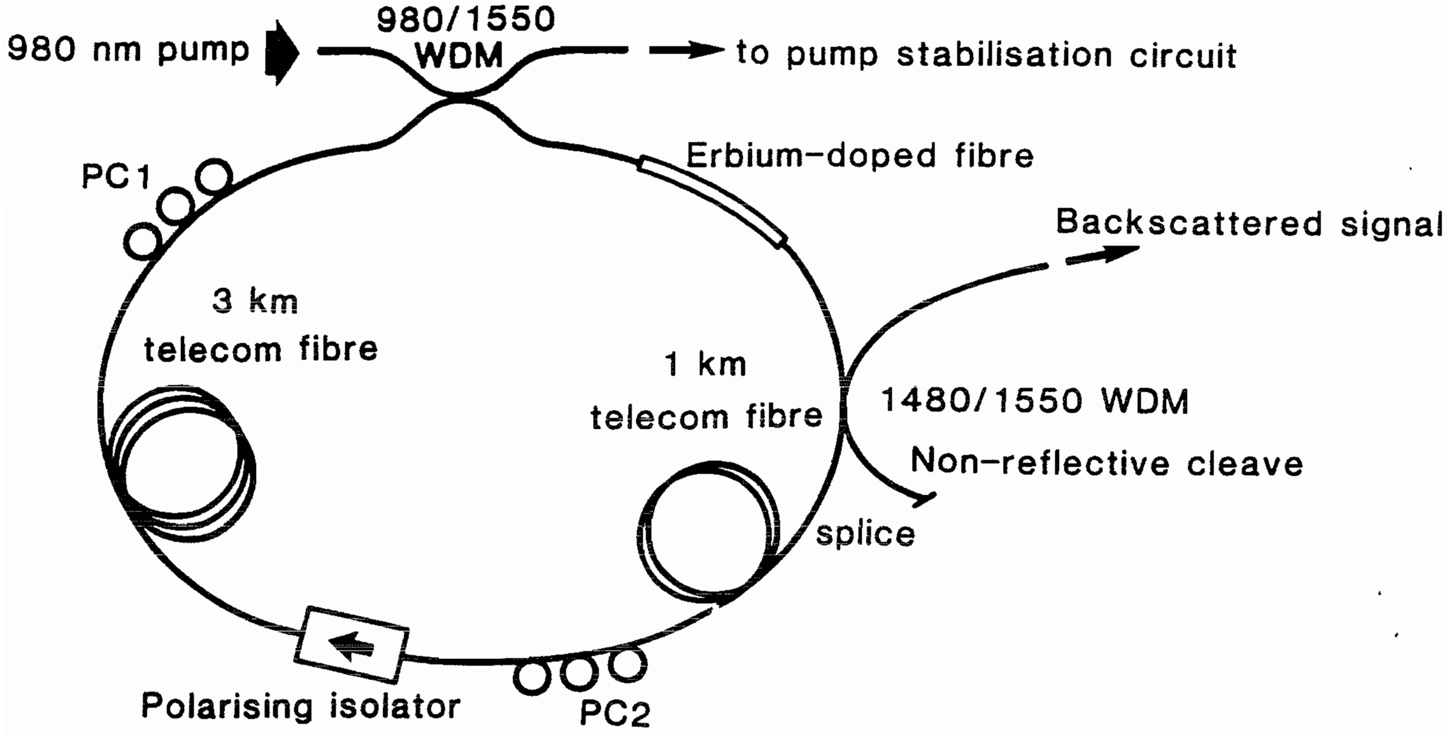

Fig.5.16 The 4-km passively mode-locked ring laser configuration.

controllers and a 1480/1550 WDM coupler situated between the erbium-doped fibre and the 1 km reel as shown. One free port of this coupler was used to monitor the backscattered light as shown in Fig.5.16, whereas the other free port was tightly bent so as to eliminate any reflection. The output coupling of the 1480/1550 WDM at the lasing wavelength was 16%. A 1480/1550 WDM was used as an output coupler for the backscattered light in order to enhance the intensity of the spontaneous backscattered Raman Stokes and Anti-Stokes wavelengths, located 100 nm away on either side from the main Rayleigh backscattered wavelength (1560nm). An InGaAs detector (Analog Devices Model No 713K-7-B) with 200MHz bandwidth and transimpedance gain of 16V/mW was used to detect the backscattered light. The signal was recorded using a digitizing scope with time averaging capabilities (Hewlett-Packard Model No HP 54111D).

The mode-locked operation of this laser was similar to the ring laser configurations described in detail in Chapter 4. In short, the laser produces "square" pulses of 40-50ns duration which, by appropriate adjustment of the PC's, can be split into smaller tight pulse bunches, each pulse inside the bunch being typically 1-2ns long. By gradually decreasing the pump power, only one of these pulses of 1-2ns duration can be left to circulate inside the cavity.

Fig.5.17 shows a typical backscatter trace obtained when a 43ns square pulse was circulating in the laser cavity. The power of the circulating pulse just before the 1480/1550 WDM was estimated to be 15.3 W and the average backscattered output power was 325nW. The trace is an average of 64 samples. Points (a) and (b) on the trace are shown on separate inserts for greater clarity. Point (a) represents the start of the Rayleigh backscatter signal with the small hump identifying the splice between the 1480/1500 WDM and the 1 km reel. The second, much bigger spike at point (b) originates from the optical isolator back-reflection. This was estimated from our measurements to be 58dB, in close agreement with the manufacturer's data which is 60dB. After the pulse has gone through the isolator, no backscattered signal is detected until the pulse passes the 1480/1550 WDM. The method may be applied to any mode-locked fibre laser to determine the loss parameters of each of the intracavity elements (isolators, modulators, polarisers, splices etc).

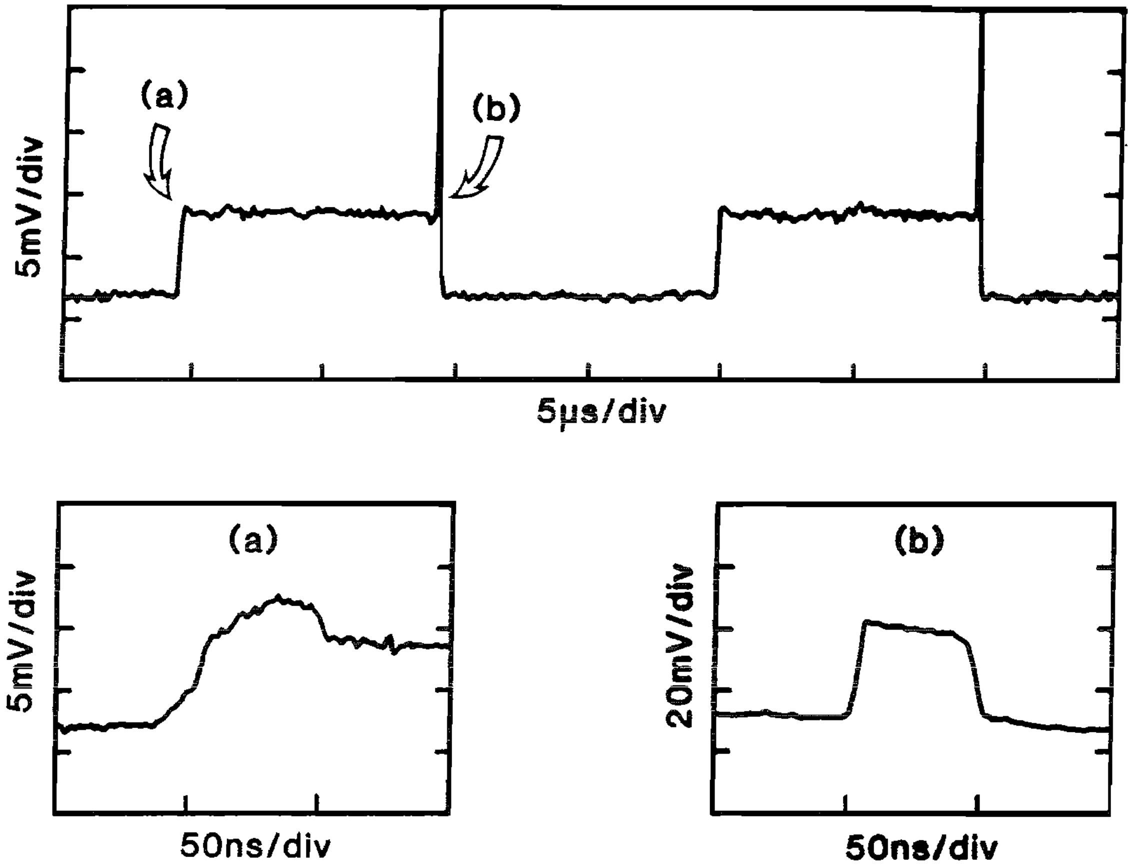

Fig.5.17 Rayleigh backscatter trace obtained from a 35ns pulse circulating in the 4 km ring laser.

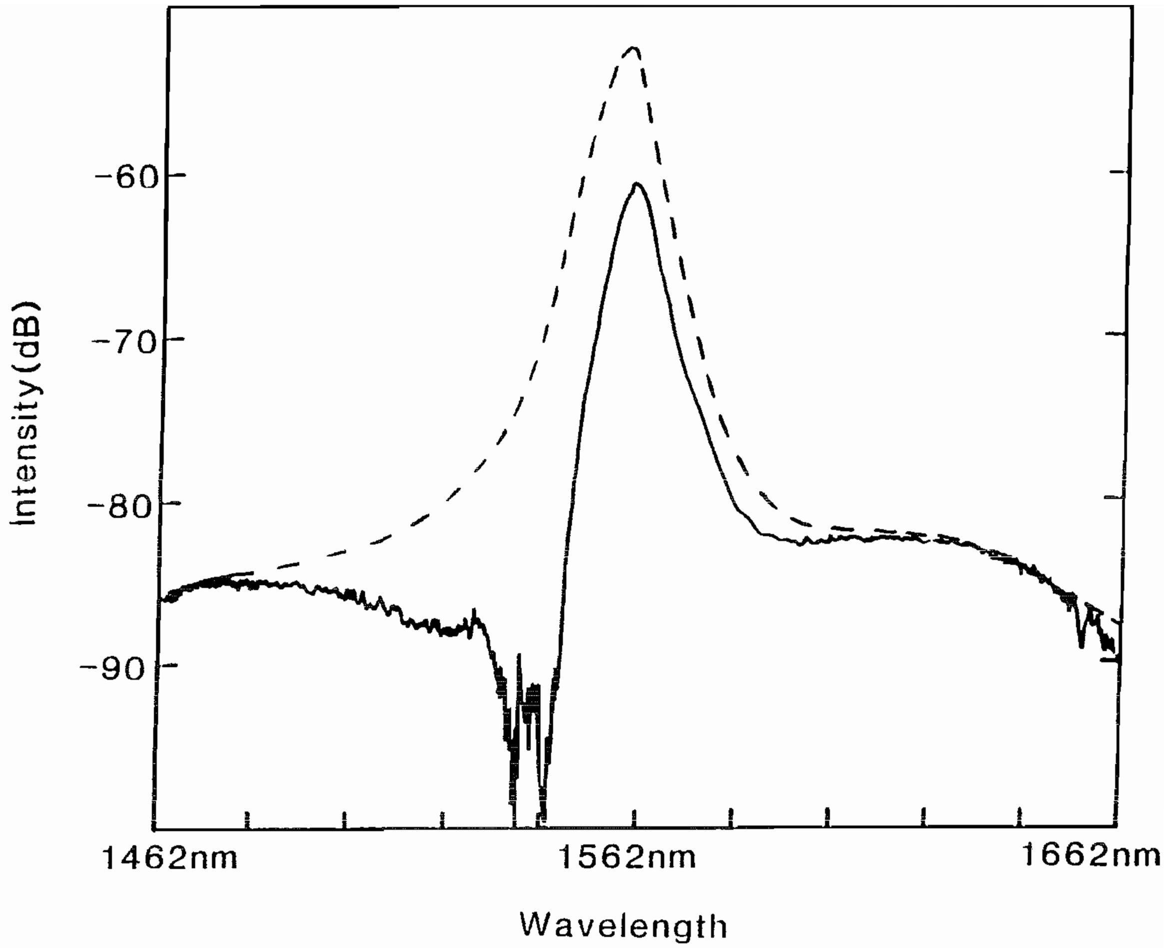

Fig.5.18 The optical spectrum of the backscattered signal shown in Fig.5.17 (solid line) and with coupler correction (broken line).

The optical spectrum of the backscattered signal is shown in Fig.5.18. The solid line shows the optical spectrum of the detected signal while the broken line shows the true optical backscattered spectrum after correcting for the 1480/1550 WDM's transmission characteristics. Fig.5.18 indicates that there is strong evidence of backscattered spontaneous Raman Stokes and anti-Stokes light; measurements of the backscattered spontaneous emission of erbium at wavelengths 1460 and 1660nm corresponding to the peaks of the Raman gain spectrum are more than 15dB below our recorded values. This demonstrates that the system is not only able to measure attenuation by conventional Optical Time-Domain Reflectometry [9] but also has the potential to become a distributed temperature sensing device, based on the measurement principles outlined previously.

5.6 CONCLUSIONS

This chapter investigated the potential of distributed temperature sensing by means of measuring the backscattered light produced by an optical pulse circulating in a long mode-locked fibre laser. In an extension of the Kuizenga-Siegman's model for homogeneously broadened actively mode-locked lasers which allowed for the inclusion of the effects caused by dispersion in the host medium, theoretical predictions for the pulsewidth and bandwidth of the mode-locked pulses for the cases of amplitude (AM) modulation and phase (FM) modulation have been derived and compared with experimental results based on long, actively mode-locked fiber laser systems. The pulsewidths achieved in these systems were an order of magnitude higher than those predicted by the theory but an estimate for the pulse transient build-up time indicated that the theory breaks down at very long cavity round-trip times. The passively mode-locked system based on the non-linear polarisation evolution technique presented at Chapter 4 was subsequently used, providing square pulses of 1-35ns duration with ~15W of peak power (intracavity). Time-domain reflectometry measurements performed on this 4km-system provided an estimate for the transmission/back-reflection of the various intracavity elements while the backscattered specrtum showed the existence of the Raman Stokes/anti-Stokes spectra.

REFERENCES

1. D.Kuizenga, A.Siegman: "FM and AM mode locking of the homogeneous laser: Part I: Theory" *IEEE J.Quantum Electron.* **QE-6** p.694 (1970).

2. J. P. Dakin, D. J. Pratt, G. W. Bibby and J. N. Ross: "Distributed optical fibre Raman temperature sensor using a semiconductor light source and detector" *Electr. Lett.* **21** p.569-570 (1985).

3. J. Dakin and B. Culshaw ed.: "*Optical Fiber Sensors, Vol.II*" Artech House Publishing ISBN 0-89006-376-1.

4. D. Philen, I. White, J. Kuhl, S. Mettler: "Single-mode fiber OTDR: Experiment and theory" *IEEE J.Quantum Elect.* **QE-18** p.1499 (1982).

5. G. Agrawal: *Nonlinear fibre optics* Academic Press (1989).

6. X. Shan and D. M. Spirit:"Novel method to suppress noise in harmonically mode-locked erbium fibre lasers" *Electron. Lett.* **29** p.979 (1993).

7. R. Picard and P. Schweitzer: "Theory of intensity-correlation measurements on imperfectly mode-locked lasers" *Phys.Rev.* **A1** p.1803 (1970).

8. A. Siegman: *Lasers* Oxford University Press (1985).

9. P. Healey: "Instrumentation principles for optical time domain reflectometry" *J. Phys. E: Sci. Instrum.* **19** p.334-341 (1986).

APPENDIX TO CHAPTER 5

The quadratic equation for Γ in the presence of second-order dispersion is

$$\Gamma^2-\Gamma\delta_g\omega_m^2-\frac{\delta_g\omega_m^2\Delta\omega^2}{16g+4j\beta_2L\Delta\omega^2}=0 \tag{A5.1}$$

where $\delta_g=\delta_t$ or $\pm j\delta_c$, depending on whether an AM or an FM modulator is used. For AM mode-locking, the solution of eqn.(A5.1) is

$$\Gamma=\frac{\delta_t\omega_m^2}{2}\pm\frac{\delta_t\omega_m^2}{2}\left[1+\frac{R}{1+j\Delta}\right]^{\frac{1}{2}} \tag{A5.2}$$

where

$$R\equiv\frac{\Delta\omega^2}{4g\,|\,\delta_g\,|\,\omega_m^2} \tag{A5.3}$$

and Δ is given by eqn.(5.21).

The complex expression on the RHS of eqn.(A5.2) is equal to

$$\begin{aligned}\left[1+\frac{R}{1+j\Delta}\right]^{\frac{1}{2}}&=R^{\frac{1}{2}}\left[\left[\frac{1}{R}+\frac{1}{1+\Delta^2}\right]^2+\left[\frac{\Delta}{1+\Delta^2}\right]^2\right]^{\frac{1}{4}}e^{j\frac{\theta}{2}}\\&\approx R^{\frac{1}{2}}\left(1+\Delta^2\right)^{-\frac{1}{4}}e^{j\frac{\theta}{2}}\end{aligned} \tag{A5.4}$$

where

$$\theta=\tan^{-1}\left[-\frac{R\Delta}{1+\Delta^2+R}\right]\approx\tan^{-1}(-\Delta) \tag{A5.5}$$

and we have used the fact that for any case of practical interest $R>>1+\Delta^2$.

The real and imaginary parts of Γ, α and β, are thus

$$\alpha=\frac{\delta_t\omega_m^2}{2}\left[1+R^{\frac{1}{2}}\left(1+\Delta^2\right)^{-\frac{1}{4}}\cos\frac{\theta}{2}\right] \approx \frac{\delta_t\omega_m^2}{2}R^{\frac{1}{2}}\left(1+\Delta^2\right)^{-\frac{1}{4}}\cos\frac{\theta}{2} \tag{A5.6}$$

$$\beta=\frac{\delta_t\omega_m^2}{2}R^{\frac{1}{2}}\left(1+\Delta^2\right)^{-\frac{1}{4}}\sin\frac{\theta}{2} \tag{A5.7}$$

from which, using eqn.(5.10), τ_D(AM) is determined.

For FM mode-locking, $\delta_g = \pm j\delta_c$ and the solution to eqn.(A5.1) is

$$\begin{aligned}\Gamma^+&=\frac{j\delta_c\omega_m^2}{2}\pm\frac{\delta_c\omega_m^2}{2}\left[-1+\frac{jR}{1+j\Delta}\right]^{\frac{1}{2}}\\ \Gamma^-&=\frac{-j\delta_c\omega_m^2}{2}\pm\frac{\delta_c\omega_m^2}{2}\left[-1-\frac{jR}{1+j\Delta}\right]^{\frac{1}{2}}\end{aligned} \tag{A5.8}$$

The complex expressions on the RHS of eqn.(A5.8) are equal to

$$\left[-1+\frac{jR}{1+j\Delta}\right]^{\frac{1}{2}}=\left[\frac{\left(R\Delta-\left(1+\Delta^2\right)\right)^2+R^2}{\left(1+\Delta^2\right)^2}\right]^{\frac{1}{4}}e^{j\frac{\theta'}{2}} \approx R^{\frac{1}{2}}\left(1+\Delta^2\right)^{-\frac{1}{4}}e^{j\frac{\theta'}{2}} \tag{A5.9}$$

$$\left[-1-\frac{jR}{1+j\Delta}\right]^{\frac{1}{2}}=\left[\frac{\left(R\Delta+\left(1+\Delta^2\right)\right)^2+R^2}{\left(1+\Delta^2\right)^2}\right]^{\frac{1}{4}}e^{j\frac{\theta'+\pi}{2}} \approx jR^{\frac{1}{2}}\left(1+\Delta^2\right)^{-\frac{1}{4}}e^{j\frac{\theta'}{2}} \tag{A5.10}$$

where

$$\theta' \approx \tan^{-1}\left[\frac{1}{\Delta}\right] \tag{A5.11}$$

and we used the fact that in all cases of practical interest $R\Delta >> 1+\Delta^2$. The real and imaginary parts of Γ are thus

$$\begin{aligned} \alpha^+ &= \frac{\delta_c\omega_m^2}{2}R^{\frac{1}{2}}\left(1+\Delta^2\right)^{-\frac{1}{4}}\cos\frac{\theta'}{2} \\ \beta^+ &= \frac{\delta_c\omega_m^2}{2}\left[1+R^{\frac{1}{2}}\left(1+\Delta^2\right)^{-\frac{1}{4}}\sin\frac{\theta'}{2}\right] \approx \frac{\delta_c\omega_m^2}{2}R^{\frac{1}{2}}\left(1+\Delta^2\right)^{-\frac{1}{4}}\sin\frac{\theta'}{2} \end{aligned} \tag{A5.12}$$

$$\begin{aligned} \alpha^- &= \frac{\delta_c\omega_m^2}{2}R^{\frac{1}{2}}\left(1+\Delta^2\right)^{-\frac{1}{4}}\sin\frac{\theta'}{2} \\ \beta^- &= \frac{\delta_c\omega_m^2}{2}\left[-1+R^{\frac{1}{2}}\left(1+\Delta^2\right)^{-\frac{1}{4}}\cos\frac{\theta'}{2}\right] \approx \frac{\delta_c\omega_m^2}{2}R^{\frac{1}{2}}\left(1+\Delta^2\right)^{-\frac{1}{4}}\cos\frac{\theta'}{2} \end{aligned} \tag{A5.13}$$

CHAPTER 6

SUMMARY OF THE THESIS AND GENERAL CONCLUSIONS

This thesis presented a theoretical and experimental examination of a number of single-mode fibre laser devices which are aimed for short-pulse generation via passive or active mode-locking. The passively mode-locked configurations that were examined were the Birefringence-Bias (B-B), the Figure-of-Eight (F-8) and the Non-Linear Polarisation Evolution (NLPE) laser. The actively mode-locked fibre laser configurations were part of an investigation of their potential use as distributed sensors and were hundreds of meters long. The structure of the thesis was as follows:

Chapter 2 provided a brief description to continuous wave characteristics of fibre lasers. The analysis assumed ideal 3 or 4-level systems and included possible signal and pump background losses and the effect of a power-dependent overlap. It was shown that the power-dependent overlap leads to the introduction of a power-dependent effective area and a power-dependent optimum cut-off wavelength. The optimum cut-off wavelengths of two fibre laser systems namely Er^{3+} and Pr^{3+} were calculated and the results were compared with numerical models developed by other groups. An analytical approach was pursued wherever possible, although in some cases this led to cumbersome expressions. An analysis to determine the lasing wavelength of Er^{3+}-doped lasers as a function of the cavity losses and length of Er^{3+}-doped fibre used, confirmed experimental observations on the F-8 and NLPE Er^{3+} lasers which demonstrated the existence of three lasing "windows" at 1.61, 1.56 and 1.53μm. Chapter 2 concluded with guidelines for achieving minimum threshold or maximum output power. Further work on CW laser modelling should be concerned with optimising the performance of more complicated systems, such as the Er^{3+}/Yr^{3+} system, which has a great potential for single-mode and high power applications.

Chapter 3 described the mode-locked performance of the B-B and the F-8 lasers. The linear and non-linear characteristics of the Sagnac loop mirror, upon which the operation of the B-B and F-8 laser relies, were analysed in detail. Experimental results on a Nd^{3+}-doped B-B laser demonstrated the production of 1-10ns square pulses whereas an Er^{3+}-doped F-8 system produced either square or soliton pulses, depending on the pump power. Both systems were self-starting, but the soliton operation of the F-8 laser was only observed at pump powers close to the lasing threshold. Depending on the cavity length, the F-8 produced soliton pulses between 1ps and 300fs. An analysis based on the average soliton model revealed a pulsewidth limitation mechanism showing that limiting pulsewidth depends on the square-root of the dispersion-length product of the laser cavity. Thus, in order to achieve shorter soliton pulswidths, the cavity dispersion-length product should be minimised. The analysis also revealed that the magnitude of the intracavity losses play an important role in the final pulsewidth determination. Experimental results showed excellent agreement with these predictions.

Chapter 4 introduced and applied the technique of NLPE to produce self-starting, passive mode-locking in ring and Fabry-Perot fibre laser cavities. The laser systems were characterised with respect to their modes of mode-locked operation, cavity length and type of optical fibre used. The mode-locked operation was in general similar to that observed with the F-8 laser, with the soliton pulses being produced at low pump powers and square pulses appearing at higher pump power levels. Two important effects that were observed in the soliton regime and were not observed with F-8 laser were the existence of a wavelength-unstable mode, in which the operating wavelength was observed to change abruptly with varying pump power, and a multiple wavelength operation mode, in which identical soliton spectra were observed to lase simultaneously at different wavelengths. The appearence of these effects is believed to stem from the wavelength-dependent loss of the cavity, but further research on soliton propagation in birefringent fibres should be conducted in order to fully understand these phenomena. The soliton pulsewidths ranged from 5ps down to 700fs with the shortest cavity length used. The low-birefringence fibre, that was used in most of the experiments, provided the most stable mode-locked operation. The Fabry-Perot fibre laser was found to have a much higher self-starting threshold for passive mode-locking than the fibre ring cavity. In accordance with the theoretical results of Krausz and Brabec, this effect was attributed to the existence of a complex refractive index grating which is formed by the standing wave pattern of the Fabry-Perot cavity. However, further work is needed in order to establish a definite quantitative agreement between Krausz's theory and our experiments. This would involve measuring the width of the first intermode-beat spacing in different types of fibre laser as well as the number of lasing modes as a function of pump power for each laser.

Compared to F-8 soliton lasers, the NLPE fibre ring laser can produce slightly better quality solitons since it does not involve the pulse splitting and the subsequent interferometric recombination that solitons undergo inside a F-8 laser. Both schemes have been identified as potential sources of picosecond soliton pulses which are thought to be the future carriers of digital information. Advantages such as high pulse quality, compactness and compatibility with single-mode optical fibre technology as well as low cost have placed them in a truly competitive position with respect to mode-locked semiconductor laser diodes. However, there are still some very important problems that should be addressed if these fibre lasers are to be used as soliton sources for future transmission systems, namely repetition-rate stability, environmental sensitivity and the dispersive wave generation problem. A possible solution to the environmental stability issue would be to use polarisation maintaining (PM) fibres. In this case F-8 fibre lasers, which can be wholly constructed from PM fibres and couplers, have a significant advantage over NLPE fibre ring lasers which would require the inclusion of an environmentally shielded, ordinary fibre section where NLPE can take place. The repetition rate stabilisation problem requires the development of an active, low-loss, intracavity fibre modulator, which in conjunction with the passive mode-locking mechanism would produce a well-defined, repetitively stable pulse train. In addition, single-mode fibre gratings could be used for bandwidth limitation and/or dispersion compensation purposes.

Chapter 5 investigated the potential use of a long ($\sim$1-4 km) mode-locked fibre laser as a distributed temperature sensor (DTS). A theoretical analysis showed that in order to compete with the existing state-of-the-art DTS systems, such a laser should produce 10-15W of pulses of $< \sim$5ns duration. A variety of cavity arrangements and mode-locking schemes were therefore examined and the experimental results were compared with the Kuizenga-Siegman (K-S) theory, extended to account for the effects of intracavity dispersion. This comparison showed a significant discrepancy between theory and experiment, which was attributed to the break-down of the K-S theory at very long resonator lengths and low modulation frequencies. The most successfull system of all those that were examined was a 4 km passively mode-locked ring laser configuration, similar to that presented in Chapter 4. This scheme produced 1-35ns pulses, depending on pump power, with peak intracavity powers of ~15W. Rayleigh backscatter measurements on this system provided an estimate of the various intracavity losses and the optical backscattered spectrum revealed the presence of Raman Stokes and anti-Stokes wavelengths. Future work should aim to temporally resolve these signals and hence extract the temperature profile along the fibre laser cavity.

In order to construct a practical distributed temperature sensing system based on the shuttle-pulse approach, the mode-locking performance of the fibre laser must be completely immune to any environmental influences. The fact that the operation of the passively mode-locked system discussed above depends heavily on the value of the fibre birefringence poses a serious obstacle towards environmental stability. In addition, the problem of repetition rate instability should also be dealt with. Hence, in a similar fashion with soliton pulse production, future work aimed at solving these problems should consider the use of a fast, low-loss fibre modulator and PM fibres to ensure repetition rate and environmental stability.

LIST OF PUBLICATIONS

1. D. J. Richardson, R. I. Laming, D. N. Payne, V. J. Matsas and M. W. Phillips: "Self-starting, passively mode-locked erbium fibre ring laser based on the amplifying Sagnac switch" *Electron.Lett.* **27** p.542 (1991).

2. D. J. Richardson, R. I. Laming, D. N. Payne, V. J. Matsas and M. W. Phillips: "320fs soliton generation with passively mode-locked erbium fibre laser" *Electron.Lett.* **27** p.730 (1991).

3. D. J. Richardson, R. I. Laming, D. N. Payne, V. J. Matsas and M. W. Phillips: "Pulse repetition rates in passive, self-starting femtosecond soliton fibre laser" *Electron.Lett.* **27** p.1451 (1991).

4. V. J. Matsas, T. P. Newson, D. J. Dichardson and D. N. Payne: "Self-starting passively mode-locked fibre ring soliton laser exploiting nonlinear polarisation rotation" *Electron.Lett.* **28** p.1391 (1992).

5. V. J. Matsas, T. P. Newson and M. N. Zervas: "Self-starting, passively mode-locked fibre ring laser exploiting non-linear polarisation switching" *Opt.Commun.* **92** p.61-66 (1992).

6. V. J. Matsas, D. J. Richardson, T. P. Newson and D. N. Payne: "Operating modes of a self- starting, passively mode-locked fibre ring laser exploiting non-linear polarisation rotation" ECOC' 92, Berlin, Germany, Sept.1992.

7. V. J. Matsas, D. J. Richardson, T. P. Newson and D. N. Payne: "Characterisation of a self- starting, passively mode-locked fibre ring laser exploiting non-linear polarisation rotation" *Opt.Lett.* **18** p.358 (1993).

8. V. J. Matsas, W. H. Loh and D. J. Richardson: "Self-starting, passively mode-locked Fabry-Perot fibre soliton laser using nonlinear polarisation evolution" CLEO'93, Baltimore, USA, May 1993, Paper JWB1.

9. V. J. Matsas, W. H. Loh and D. J. Richardson: "Self-starting, passively mode-locked Fabry-Perot fibre soliton laser using non-linear polarisation evolution" *IEEE J. Photon. Lett.* **5** p.492 (1993).

10. V. J. Matsas, T. P. Newson and D. N. Payne: "Optical time-domain reflectometry measurements in a 4km fibre ring laser" *Electron. Lett.* **29** p.1602 (1993).